Università di Pisa

Facoltà di Scienze Matematiche, Fisiche e Naturali

Corso di Laurea Specialistica in Scienze Fisiche
Anno accademico 2010/2011

Tesi di Laurea Specialistica

Chaos Characterization of Pulse-Coupled Neural Networks in Balanced State

Candidato	**Relatore Esterno**	**Relatore Interno**
Dylan Festa	Prof. Fred Wolf	Prof. Leone Fronzoni

Alla mia famiglia;
grazie a Voi, so che si dà
per il piacere di Essere.

Contents

Introduction

From the first theories of matter as constituted by elementary particles [*Democritus* (ca. 460 BC – ca. 370 BC)] up to the twentieth century, the dominating trend in physical, and, more generally, in scientific research has been *reductionism*: the principle that any complex system can be decomposed in elementary parts, which are then studied singularly, so that the full knowledge of the global phenomenon is expressed in terms of the elementary interactions between its simple entities.

Such approach has provided, and still provides, marvellous insights, crucial for the realization of most of the science and the technology we see around us. Nevertheless, it proves not sufficient when it comes to dealing with the study of the *emergent phenomena*.

Emergence can be defined, in natural and social science, as *the arising of novel and coherent structures, patterns and properties in complex systems.* In apparent contradiction to the third principle of thermodynamics, we are surrounded by emergent, highly ordered structures, life itself being the most astonishing example of all of them. Unfortunately, a reductionist approach does not prove to be sufficient, or even apt, for the study of such phenomena. The new challenge for science and research is to find models and rules for emergent phenomena, and apply them to reality. Complex networks are typical models showing the arise of complex bahviour and collective phenomena from an aggregation of relatively simple constituents.

Complex Networks

Although networks can reveal a rich variety of behaviours, and emergent phenomena, their definition is quite simple: a network is a set of items, usually called *nodes*, with connections between them, referred to as *edges* [1]. The topological study of networks started with Euler, and his solution to the *Könisberg Bridge Problem*, which laid down the foundations of the mathematical *Graph Theory*. Since then, extensive studies on a high variety of networks and on the dynamics taking place on them have been conducted, and now many scientific models rely on network structures; just to name a few: food webs, genetic networks, power grids, models for the spreading of computer viruses or human diseases, etc. [2]. A surprising number of examples on the importance of networks in science, technology, society and every-day life can be found in a popular book written by Barabási [3].

Neural Networks

Neural network constitute a class of complex network inspired by the structure of the nervous system. The nodes are identified with *neurons*, the edges represent the links between them (*axon* and *synapses*) and the exchanged signals are the electrical peaks, or spikes, (*action potentials*) triggered when the internal potential of the neuron reaches a certain threshold. They were introduced mainly to solve artificial intelligence problem, such as automated learning, visual pattern recognition, adaptivity, fault tolerance, etc. or as models for networks of real nervous cells [4].

In the present work, we consider the latter category of neural networks, aiming at a better understanding and modelling of real biological structures. The first example of such approach dates back in 1975, when Peskin modelled the peacemaker cells of the heart as a fully connected network of identical leaky integrate-and-fire neurons (LIF), and verified that they spontaneously synchronise their signals, as real peacemaker cells do [5]. The LIF model is the simplest one dimensional model for the electrical activity of a neuron. The use of more complex and refined models would add more biophysical value to the investigation, but the required computations would increase dramatically with the network size; moreover phenomena emerging from the collective dynamics of the system should not depend too much on the precise and realistic reconstruction of its single components.

The specific system we are interested in is not the hearth, but the pyramidal neurons of the neocortex in their stationary state. Many experiments on living cells, both *in vitro* and *in vitro*, showed that, although very dense, and densely connected ($\sim 10^6$ neurons on a mm^3, with $\sim 10^4$ connections each), they exhibit very low average firing rates ($\sim$ 1Hz), with a spike pattern very variable in time, and very weakly correlated, even when sampled from neurons close each other; at the same time, the response in time seems surprisingly fast when compared to reaction times for isolated, individual neurons. The system is therefore doubly efficient: the low spiking rate reduces the energy consumption, but, at the same time, it is able to react even faster than any of its isolated components would. Admittedly, brains still detain the record of most efficient and complex parallel calculators in the known universe.

Going back to the the neocortex, the model used to explain the observed activity is the *balanced state model*. Namely each neuron, for most of the time, is kept close to its firing threshold by a balance between excitatory and inhibitory inputs from other neurons, so that even very small deviations result in a quick response by the interested neuron. Different experiments and measures confirmed this theory (see section 2.3). Our aim is now to construct a neural network which replicates, at least qualitatively, this kind of behaviour, and study it.

The creation of a neural network in stationary balanced state requires just the mixing of the right ingredients, namely:

a) a proper model for single neuron dynamics, as simple as possible;

b) a very large number of neurons, and number of connections between them still very large but small when compared to the size of the system, so to resemble the connectivity of real neurons;

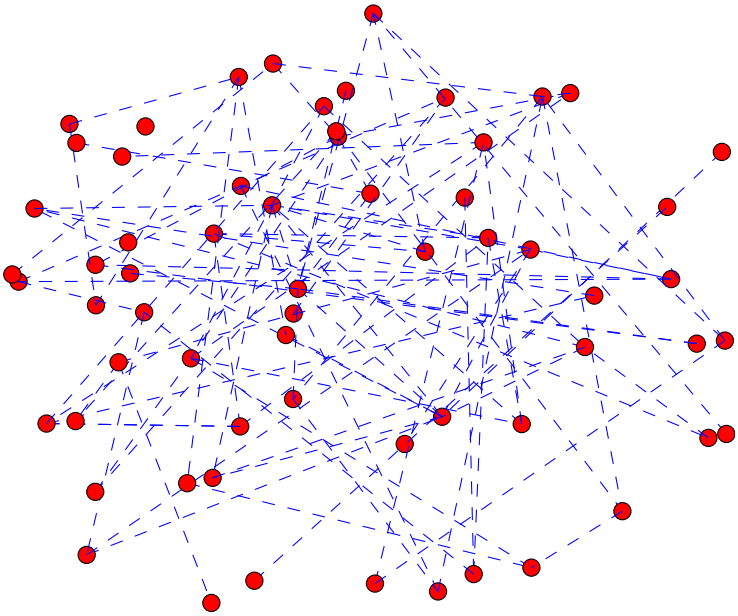

Figure 1: Simplified representation of a sparsely connected Erdős-Rény random graph. The image shows ~ 60 neurons with an average of 1.5 connections each. The simulated networks range from 200 to 1000 neurons with $20 - 50$ average connections. The orientation of the connections is not shown.

c) both excitation and inhibition acting on neurons.

The first choice for point **a)** would be the LIF neuron, however they have been excluded for an intrinsic flaw in their dynamics: when the membrane potential of a real neuron crosses a certain threshold, a positive-feedback process furtherly increases it, producing a peaked signal; LIF neurons, on the other end, are artificially reset in the instant they touch their threshold. With this qualitative difference, LIF neural networks have the tendency to synchronize. In networks made of inhibitory neurons subjected to positive external currents this phenomenon has been proved analytically [6]. For that reason the chosen model is the simples *canonical* 1D neuron model: the quadratic integrate and fire described in chapter 2.

Condition **b)** is obtained by connecting a large number of neurons with an Erdős-Rény random graph structure, as represented in figure 1. If N is the total number of neurons and K the average connections *per neuron*, our ideal conditions would be $N \gg K \gg 1$. In the actual model N ranges from 200 to 1000, while K from 20 to 100. Finally all connections are assumed to be one-directional, as for real neurons. For graphical reasons the figure does not show connection orientations, and the parameters are reduced to $N \approx 60$, $K \approx 1.5$.

As regards the point **c)**, it has been found that a network of only inhibitory neurons, subjected to a constant, excitatory external current, suffices to fulfil it. This simplifies the model and the calculations, so that we can concentrate on more essential parameters.

The system defined with those requisites shows *deterministic chaos*. For a further characterization of the system and its properties, and for a better un-

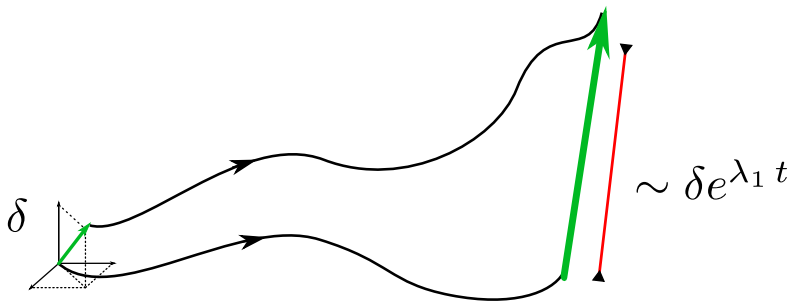

Figure 2: Intuitive definition of the first Lyapunov exponent ad the logarithm of the expansion rate for to points initially very close in the phase space. The direction of expansion is coded by the first Lyapunov vector.

derstanding, we rely on the mathematical framework typically used for large, complex, dynamical systems: the *Ergodic Theory*.

Ergodic theory

Since chapter 1 contains most of the formalism, the correct definitions and the mathematical rigour necessary to define and describe the ergodic properties and quantities we are interested in, in this section we give a more intuitive (and less formally correct) description of what ergodicity is about.

Given a finite-dimensional, deterministic dynamical system, its phase space is defined as the n-dimensional manifold in which every single point fully represents the exact state of the system at a given time. As the system evolves, it draws a trajectory the phase space which cannot intersect itself, or trajectories associated to other time evolutions.

The basic idea of ergodic theory is that, for sufficient extents of time, averaging over time any quantity associated to the dynamical system is completely equivalent to performing an average on the whole phase space, as long as such manifold is weighted with an *ergodic measure*. Intuitively, such a measure should neglect the areas of phase space never (or almost never) touched in the evolution of our system, and give more importance to those in which the system lingers much more in time (the *attracting manifold*).

With this approach we can find quantities that are global and invariant for the system just following a single time evolution starting at a random point: the information gained from such trajectory would be equivalent to studying the system as a whole, or to what we would find using any other trajectory starting from different points; as long as, of course, the system in question is ergodic. One of the most crucial quantities for the characterisation of a dynamical system is the *first covariant Lyapunov exponent*, as it is strictly bound with the definition of deterministic chaos.

The idea of a dynamical system both deterministic and chaotic, - i.e. with a time evolution completely and uniquely determined by its variables on one hand, but complex and not predictable in the long term on the other hand - is only an apparent paradox, easily resolved stating that deterministic chaos is the property of systems where two points, arbitrarily close in phase space

$d(t_0) = \delta \ll 1$, evolve in time on paths diverging with an *exponential* rate $d(t) \simeq \delta e^{\lambda_1 t}$, $\lambda_1 > 0$ (see figure 2) . The result is that, since we can know the state of a system only with *finite* precision, any long term forecast would eventually be outgrown by the exponentially increasing error associated to our initial uncertainty. This is basically what Lorentz originally intended as "the butterfly effect".

The first Lyapunov exponent is, roughly speaking, the $\delta \to 0$ limit of the exponent associated to that divergence, averaged for time $t \to \infty$. If positive, the system is clearly chaotic. If negative, we can say that separate trajectories would eventually converge, although for a particular class of dynamical systems the time needed grows so fast with the system dimensionality that the dynamics appear practically chaotic. Such property is called *stable chaos* [7].

Going back to figure 2, we notice that the maximum divergence defines, in time, also a direction. We call the direction associated to the maximum expansion the *first Lyapunov vector* $v^{(1)}(t)$. It is local, since it depends on the point in phase space we are considering.

Apart from points, we can consider n-dimensional phase space volumes. This introduces the idea of different orders of Lyapunov exponents, as well as different associated directions: a k dimensional hypercube would increase (or shrink) its size as $V(t) \simeq V(t_0) \exp\left(t\left(\lambda_1 + \ldots + \lambda_k\right)\right)$, and the deformation of its shape would follow, in time, the directions of the associated Lyapunov vectors. Figure 3 represents an example of this: the first direction is expanding, the second corresponds to a 0 exponent, finally the third is contracting. The volume expands as the sum of the three exponents, and its shape changes: we expect that the direction associated to the 0 exponent keeps being parallel to the motion, but nothing can be said, in general, about the expanding and contracting directions, and the angle between them. The systems we are interested in are *dissipative*: the sum of all Lyapunov exponents is negative, so that a volume in phase space shrinks during the dynamical evolution, progressively falling on a subset of the total phase space manifold called *attractor*.

The attractor has, in general, a very complex shape, possibly fractal. A useful property of the exponents is that they can give an esteem of the attractor dimension. If the first exponent is positive, but the total sum is negative, for a certain integer k we have $\lambda_1 + \ldots + \lambda_k \simeq 0$ (if the sum is not exactly zero, we can add a small non-integer correction to k). Then, for what stated above, a volume of dimension k will neither expand nor contract in time, thus giving an *upper bound* to the attractor dimension.

Another esteem derived from the exponents is the *entropy* production rate. Assuming we know the initial state of the system with finite precision, the exponential spreading of trajectories from points initially indistinguishable adds information regarding their initial state, thus chaotic dynamical systems can be seen as producers of information, and the production rate can be estimated as the sum of the positive Lyapunov exponents.

The calculations of entropy and attractor dimension are actually esteems that, in general, cannot be taken as exact equalities. There is, however, a class of dynamical systems, called *axiom-A*, for with the entropy calculation is *proved* to be correct, while the attractor dimension esteem is *conjectured* to be. Estimating if a complex, chaotic dynamical system is axiom-A or not is mathematically a very hard task, and a general approach has yet to be found. What we did in

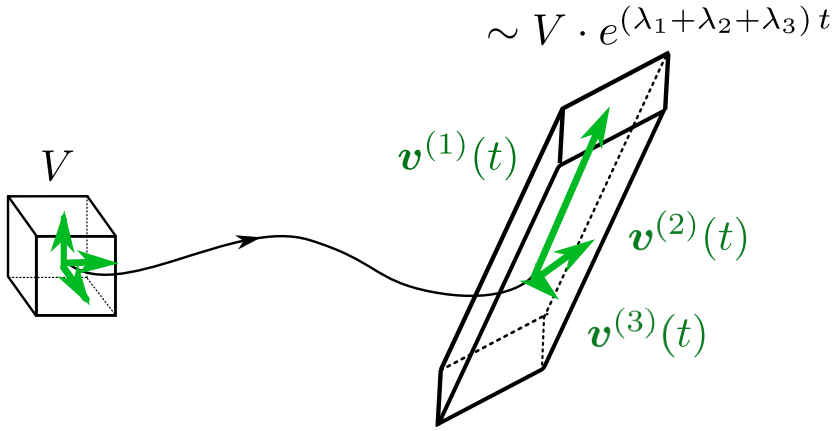

Figure 3: The series of Lyapunov exponents decodes the expansion/contraction rate for volumes. In this example a volume grows in one direction, maintains its size in another, and shrinks in the third: $\lambda^{(1)} > 0$, $\lambda^{(2)} = 0$, $\lambda^{(3)} < 0$. The directions are given by the Lyapunov vectors associated to the exponents.

the present work is investigate if the system we are interested in satisfies one of the key requisites for axiom-A: *hyperbolicity*.

Basically, in hyperbolical systems expanding and contracting directions do no mix up (see the end of chapter 1 for further details. In the present work we check if this requisite is respected by studying the angles between contracting and expanding directions, given by the Lyapunov vectors associated to, respectively, positive or negative global exponents.

Thesis Structure

The aim of the present work is to simulate and, using the ergodic formalism, fully characterise a large-scale neural network of inhibitory quadratic integrate-and-fire neurons.

Chapter 1 introduces and explains the ergodic theory more formally. Quantities such as attractor dimension, Lyapunov exponents, entropy production rate and Lyapunov vectors are defined, explaining also how they can be numerically computed.

The following chapter deals with the construction of the neural network. First we model the one-neuron dynamics, taking the general Hodgkin-Huxley equations as a starting point. Trough different levels of approximation we reach the simplest canonical 1D description for a neuron: the quadratic integrate-and-fire or theta neuron. Afterwards, starting from the results of in-vivo measures on large populations of pyramidal neurons, we define the balanced state, and build a model for the computation of a large-scale network with similar qualitative behaviour.

Chapter 3 deals with the computation and the findings. It starts with a step-by-step description of the computer simulation we used. Then we assess to which extent the neuron pulses are comparable to a real balanced state.

Afterwards, we calculate numerically the Lyapunov exponents, deriving from them the entropy production rate and the attractor dimension. The findings, so far, are substantially a confirmation of what has already been presented in recent works on the subject [8, 9]. We consequently focus on the Lyapunov vectors: to confirm their invariance and the robustness of the algorithm used for their calculation, different convergence tests are performed. The minimal angles between vectors, corresponding to expanding and contracting directions are used to estimate the hyperbolicity of the dynamical system. The result is that, as the system becomes larger, the angle distribution is more peaked for a nonzero value, showing more transversality between contracting and expanding directions.

Finally, for each vector, we measure the *average participation ratio*, that counts the effective number of neurons contributing to the vector dynamics, and the *chaos index* (defined as the time average of the square vector components), that reveals *which* neurons have a predominant role for a single vector. From the interplay between these two parameters (and some others derived from them) we can characterize the network dynamics both globally and from the perspective of the single neurons. In particular, we find that the contribution to the expanding directions comes from a group with an average size that scales with K, and the single neurons that take part to it change in time, covering uniformly most of the network; on the other hand, strongly contracting directions tend to be localized on few neurons, fixed in time.

The final part summarises the novel results, namely the use of Lyapunov vectors to assess the hiperbolicity of the neural network and to characterise the role of individual neurons in the collective dynamics. A list of possible extensions and future prospects concludes the chapter.

Chapter 1

Mathematical Framework

We stated that a set of interconnected neurons can be modeled as a network and studied as a n-dimensional dynamical system. In this chapter we will describe the general mathematical framework used to study systems of known dynamics, characterized by chaotic behavior and high-dimensionality.

We start with an introduction about the statistical study of differentiable chaotic dynamical systems, through the definition of a *natural* or *physical* probabilistic measure on phase-space and the application of Birkhoff's *Ergodic theorem*.

Afterwards we focus on the characterization of chaos, defining both intuitively and in a more rigorous way the *Lyapunov exponents*. We show how the *Oseledec Ergodic theorem* implies that such exponents exist and are finite, and how the presence of a *Oseledec splitting* of phase-space emerges from that.

Using the given definitions, we illustrate the classical algorithm used to calculate the complete set of Lyapunov exponents, when the equations regulating the dynamics are fully known; then we introduce a very recent method for the calculation of a vector base corresponding to the expanding direction of the dynamics, i.e. the *local Lyapunov vectors*. The meaning of such vectors and their connection with the *local Lyapunov exponents* is briefly explained.

In the last part we describe two conjectures of Ergodic theory which investigate the connection between the Lyapunov spectrum the attractor dimension and entropy.

All quantities described in this chapter will be explicitly calculated and analyzed in the specific dynamical model described in the next chapter.

1.1 Differentiable Dynamical Systems and Ergodicity

A differentiable dynamical system is a time evolution on a compact, differentiable manifold $M \subseteq \mathbb{R}^m$ (the *phase space*), defined by a differentiable mapping or flow [10]

$$f^t : M \to M \ , \qquad \text{with } t \in \mathbb{R} \text{ for flows, } t \in \mathbb{N} \text{ for mappings;}$$

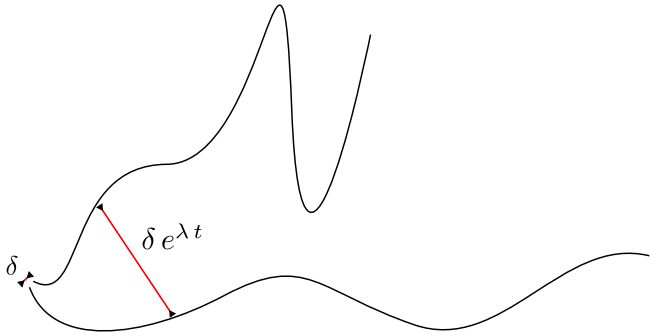

Figure 1.1: Exponentially diverging trajectories in phase space

with the properties:

$$f^0 = \text{identity} \qquad \text{and} \qquad f^s f^t = f^{s+t}\,. \tag{1.1}$$

If the system is *dissipative*, a given portion of phase space is usually contracted by the time evolution on a smaller volume. The portion of phase space where the motion is "concentrated", possibly after an initial transient, is called *attractor*. We can define the attractor as a set A with the following properties [11, 12]:

1. **is invariant** in the dynamical evolution: $\forall t$, $f^t A = A$;
2. **attracts an open set**: $\exists$ open set $U \supset A$ such that $\forall \boldsymbol{x} \in U$ the distance between A and $f^t \boldsymbol{x}$ reduces to zero in the limit $t \to \infty$.
3. **is minimal**: there is no subset of A which satisfies properties 1 and 2.

The largest U satisfying property 2 is called *basin of attraction of* A, if $U = M$ the attractor is called *universal*.

A dynamical system is said to be *chaotic* when it presents high sensitivity to initial conditions, i.e. when the trajectories of two distinct phase space points, arbitrarily near at $t = 0$, diverge exponentially during time evolution, as illustrated in figure 1.1. In the next section we elaborate the concept in greater detail and quantitatively; for now we can notice that, for a given starting point, trajectories calculated on machines with slightly different precisions or different round-off methods would completely diverge after a relatively short time. Unless we use numbers of infinite precision, there will always be some intrinsic random noise that compromises any long-term forecast of such systems. Nevertheless global statistical properties, such as the presence or the structure of the attractor, stay unchanged, regardless the starting point and the level of noise (assuming, of course, that the latter is reasonably small). In chaotic systems the attractor is therefore characterized by the additional property:

4. **is stable under small random perturbations**.

Such a property is essential to guarantee that, in experiments and numerical simulations, the motion falls asymptotically on the attractor despite the fact that the trajectory itself has poor predictive value.

The attractors of chaotic dynamical system are called *strange*. The name comes from the fact that they often present a very complex, fractal structure, i.e. with non-integer Hausdorff dimension. The definition of fractals and their properties is beyond the scope of the present work (see for example chap 11 in [12] or chapter 3 in [13]) here we just mention that similar attractors are quite hard to model and to study directly. This, along with the impossibility of calculating the "true" evolution of a point in phase space, suggests that the only possible approach to tackle those problems is *statistical* and *probabilistic*.

The tool we use for our analysis is the *Ergodic theory*. It basically says that averages on a single trajectory in time equal averages over the whole phase-space, where the phase-space is weighted by an appropriate measure μ, with the fundamental requisites of being *invariant under time evolution* and *ergodic*. Abstract ergodic theory deals a lot with the study and definition of measures that can satisfy those requisites. As physicists, hopefully interested in real differentiable dynamical system, we can luckily "bypass" this problem by operationally define a unique *natural* or *physical* measure in the way described below.

We start by taking into consideration the probability density functions (PDF) on M, defined so that, for $\boldsymbol{x} \in M$, $\rho(\boldsymbol{x})\, d\boldsymbol{x}$ is the probability of finding the system in the small volume of phase space $d\boldsymbol{x}$ around the point $\boldsymbol{x}$. Imagine to have, for $t = 0$ a given ensemble of phase-space points, corresponding to a density $\rho_0(\boldsymbol{x})$, then evolve each point in time with f, and study the series of pdfs $\rho_1(\boldsymbol{x}), \rho_2(\boldsymbol{x}), \dots \rho_t(\boldsymbol{x})$. In the $t \to \infty$ limit, we may expect that they converge to a density which is invariant under the action of dynamics: $\rho_{\text{inv}}(\boldsymbol{x})$. This is not always true, but in the systems of our concern, i.e. chaotic and finite-dimensional, the application of Perron-Frobenius theorem ensures that such a PDF exists, is unique, and is approached exponentially fast in time [14]: $\rho_t(\boldsymbol{x}) = \rho_{\text{inv}}(\boldsymbol{x}) + \mathcal{O}(e^{-\alpha\, t})$

Intuitively, if we begin with a homogeneous distribution of points in phase space, and evolve them for some time, all points would fall over the attractor and stay confined on it. Under a practical point of view, unstable fixed points and cycles do not play any role, since points on them are driven away by the random noise intrinsic to numerical computation. To be mathematically more rigorous, we could follow the idea expressed by Eckmann and Ruelle [10] (said to have been first formulated by Kolmogorov), and define our density asymptotically, as the $\epsilon \to 0$ limit of densities $\rho_{\epsilon,\text{inv}}$ characterized by a dynamics perturbed by random noise of magnitude ϵ.

The *physical* measure μ can be defined as the probability of finding the motion in a given phase-space area:

$$\mu(B) = \int_B \rho_{\text{inv}}(\boldsymbol{x})\, d\boldsymbol{x} \ .$$

From the way $\rho_{\text{inv}}(\boldsymbol{x})$ has been constructed, this measure has the crucial property of being *invariant* under dynamical evolution:

$$\mu(B) = \mu(f^{-t}B) \ .$$

After finding a "natural" candidate for the invariant measure, we can define the property of **ergodicity**, studied by Birkhoff(1931) and Von Neumann (1932):

> The invariant measure μ is said to be *ergodic* if the phase space M is metrically indecomposable with respect to it; i.e. there cannot be two distinct and invariant subsets, A and B, both with positive μ measure. In other terms, if A is invariant ($f^t A = A$), then $\mu(A) = 1$ or 0.

We can imagine that in systems with distinct attractors, the dynamic evolution would "select" one of them, according to the specific starting point, and move eternally over it. As a consequence, the statistical properties derived from such trajectory would be neither global nor invariant of the starting condition, invalidating the notion of ergodicity.

If such a simple and intuitive requisite is already enough to state the presence of ergodicity, in practice the ergodic hypothesis is impossible to demonstrate for the great majority of systems. However we can make the "reasonable assumption" that the system we are considering has only one attractor, and go on illustrating Birkhoff's **Ergodic theorem**:

> For a integrable function $\phi : M \to \mathbb{R}$, the limit
>
> $$\lim_{T\to\infty} \frac{1}{T} \int_0^T dt\, \phi\left(f^t \boldsymbol{x}_0\right) =: \langle \phi(\boldsymbol{x}_0) \rangle$$
>
> exists. If μ is an ergodic measure, then $\langle \phi(\boldsymbol{x}_0) \rangle$ is almost everywhere constant (does not depend on the initial point $\boldsymbol{x}_0$) and equal to:
>
> $$\langle \phi(\boldsymbol{x}_0) \rangle = \int_M \phi(\boldsymbol{x})\ \mu(d\boldsymbol{x}) =: [\phi(\boldsymbol{x}_0)]\ .$$

For a proof see, for example, the original article by Birkhoff [15].

The powerful result obtained is that any observable of our system, corresponding to an integrable function ϕ has a definite global average value over phase space. This value can be computed by integrating the function on a random trajectory reasonably long in time, and the result does not depend on the initial point $\boldsymbol{x}_0$ of the specific trajectory. This fundamental principle gives meaning to basically all the analysis performed in the present work.

1.2 Chaotic Dynamics and Lyapunov Exponents

As mentioned before, a dynamical system is said to be chaotic when its time evolution is highly sensitive to the initial conditions. Namely, if we take two points at distance ϵ arbitrarily small, the divergence of the two trajectories in time will be $\sim \epsilon\, e^{\lambda t}$, $\lambda > 0$. For $\lambda < 0$ the difference would quickly decay, making the dynamics stable; if $\lambda = 0$ nothing can be said. If the motion is confined on an attractor, the distance cannot grow indefinitely. What happens is that the two trajectories, after the initial strong divergence, become completely independent one another.

If we apply this concept to a point in phase space $\boldsymbol{x}$, with a small error associated $\boldsymbol{\delta x}$, we reach the conclusion that even though a chaotic system is regulated by precise equations, the exponential grow of errors makes any calculated time

evolution *self-independent* of its long-term past history, i.e. non-deterministic in any practical sense [11].

The parameter λ, called *the Lyapunov exponent*, is of primary importance in studying quantitatively the chaotic behavior and estimating its long-term predictability in such systems. For a precise definition and calculation, we need a satisfying mathematical description of the entities in question.

Let M be a smooth, compact manifold and f a mapping or flow over M with the properties (1.1); let μ be a measure invariant under time evolution; $\boldsymbol{x}$ is our starting point on M. We can identify the small difference between $\boldsymbol{x}$ and an arbitrarily close point as a vector $\boldsymbol{u}$ belonging to the tangent vector space to M in point $\boldsymbol{x}$, $T_{\boldsymbol{x}}M$. Pairs expressed as $(\boldsymbol{x}, \boldsymbol{u})$, with $\boldsymbol{x} \in M$ and $\boldsymbol{u} \in T_{\boldsymbol{x}}M$ can be interpreted as elements of the *tangent bundle* of M, that we call TM.

We can define an iteration of a given amount of time t as a map of the form:

$$\begin{aligned} T^t : TM &\to TM \\ (\boldsymbol{x}, \boldsymbol{u}) &\to \left(f^t(\boldsymbol{x}), T^t_{\boldsymbol{x}}\boldsymbol{u}\right) \ . \end{aligned}$$

The linear operator $T^t_{\boldsymbol{x}}$ maps the vector $\boldsymbol{u} \in T_{\boldsymbol{x}}M$ in $\tilde{\boldsymbol{u}} \in T_{f^t(\boldsymbol{x})}$. This operation can be seen as the *push-forward* of $\boldsymbol{u}$ by f: this implies that the operator is simply the linearized version of $f^t(\boldsymbol{x})$, i.e. its total derivative, represented by the *Jacobian matrix*: $T^t_{\boldsymbol{x}} \coloneqq Df^t(\boldsymbol{x})$.

From the properties on f and the chain derivation rule we have that:

$$T^{t+s}_{\boldsymbol{x}} = T^s_{f^t(\boldsymbol{x})}\, T^t_{\boldsymbol{x}} \tag{1.2}$$

in other words, a long time iteration is equivalent to a product of short time iterations, consisting of elements defined following the trajectory of the starting point $\boldsymbol{x}$.

From now on we will consider f as a discrete map, with $t \in \mathbb{N}$. However it is possible to generalize all the following definitions and results for flows, with little change in the notation. If $||\cdot||_{\boldsymbol{x}}$ is the vector norm over the space $T_{\boldsymbol{x}}$, we can express the rate of change of the vector $\boldsymbol{u}$ for one step ($t = 1$) as:

$$r(\boldsymbol{x}, \boldsymbol{u}) = \frac{||T^1_{\boldsymbol{x}}\boldsymbol{u}||_{f^1(\boldsymbol{x})}}{||\boldsymbol{u}||_{\boldsymbol{x}}}$$

for the next timestep, using (1.2), we have:

$$r(f^1(\boldsymbol{x}), T^1_{\boldsymbol{x}}\boldsymbol{u}) = \frac{||T^1_{f^t(\boldsymbol{x})}\, T^1_{\boldsymbol{x}}\boldsymbol{u}||_{f^2(\boldsymbol{x})}}{||T^1_{\boldsymbol{x}}\boldsymbol{u}||_{f^1(\boldsymbol{x})}} = \frac{||T^2_{\boldsymbol{x}}\boldsymbol{u}||_{f^2(\boldsymbol{x})}}{||T^1_{\boldsymbol{x}}\boldsymbol{u}||_{f^1(\boldsymbol{x})}} \ .$$

Wen we compute the *geometric mean* of the change rate for the n elements of the time series $\boldsymbol{x}$, $f^1(\boldsymbol{x})$, $f^2(\boldsymbol{x})$ $\ldots$ $f^{(n-1)}(\boldsymbol{x})$, the result is:

$$\begin{aligned} &\left[r\left(f^{(n-1)}(\boldsymbol{x}), T^{(n-1)}_{\boldsymbol{x}}\boldsymbol{u}\right) \cdot r\left(f^{(n-2)}(\boldsymbol{x}), T^{(n-2)}_{\boldsymbol{x}}\boldsymbol{u}\right) \cdot \ldots \cdot\ r(\boldsymbol{x}, \boldsymbol{u})\right]^{\frac{1}{n}} = \\ &= \left[\frac{||T^n_{\boldsymbol{x}}\boldsymbol{u}||\ ||T^{(n-1)}_{\boldsymbol{x}}\boldsymbol{u}|| \ldots ||T^1_{\boldsymbol{x}}\boldsymbol{u}||}{||T^{(n-1)}_{\boldsymbol{x}}\boldsymbol{u}|| \ldots ||T^1_{\boldsymbol{x}}\boldsymbol{u}||\ ||\boldsymbol{u}||}\right]^{\frac{1}{n}} = \left[\frac{||T^n_{\boldsymbol{x}}\boldsymbol{u}||}{||\boldsymbol{u}||}\right]^{\frac{1}{n}} \ . \end{aligned}$$

The logarithm of this quantity in the large n limit is called the *Lyapunov Characteristic Exponent* (LCE) of $(\boldsymbol{x}, \boldsymbol{u})$

$$\lambda(\boldsymbol{x}, \boldsymbol{u}) \coloneqq \lim_{n\to\infty} \log\left(\frac{||T^n_{\boldsymbol{x}}\boldsymbol{u}||}{||\boldsymbol{u}||}\right)^{\frac{1}{n}} = \lim_{n\to\infty} \frac{1}{n}\log||T^n_{\boldsymbol{x}}\boldsymbol{u}|| - \lim_{n\to\infty}\frac{1}{n}\log||\boldsymbol{u}|| = \lim_{n\to\infty}\frac{1}{n}\log||T^n_{\boldsymbol{x}}\boldsymbol{u}|| \quad (1.3)$$

This definition satisfies the properties:

$$\begin{aligned} &\forall k \in \mathbb{R}\backslash\{0\} \quad \lambda(\boldsymbol{x}, k\,\boldsymbol{u}) = \lambda(\boldsymbol{x}, \boldsymbol{u})\ ; \\ &\forall \boldsymbol{u}, \boldsymbol{v} \in T_{\boldsymbol{x}}M \quad \lambda(\boldsymbol{x}, \boldsymbol{u}+\boldsymbol{v}) \leq \max\{\lambda(\boldsymbol{x}, \boldsymbol{u}),\ \lambda(\boldsymbol{x}, \boldsymbol{v})\}\ . \end{aligned} \quad (1.4)$$

The LCE depend only on the direction of the vector, and not on its magnitude (a direct consequence of the linearity of the operator $T^t_{\boldsymbol{x}}$).

The existence of such limits is granted by **Oseledec's multiplicative ergodic theorem** [16]. It can be expressed as follows:

> Given a compact, differentiable manifold M, a mapping $f : M \to M$ and a measure μ invariant over M; let T^1 be a map from M to the space all the $m \times m$ real matrices, with the notation $T^1(\boldsymbol{x}) = T^1_{\boldsymbol{x}}$, such that
>
> $$\int_M \mu(d\boldsymbol{x}) \log^+ ||T^1_{\boldsymbol{x}}|| < \infty\ ;$$
>
> where $\log^+(k) = \max\{0, \log(k)\}$ and $||\cdot||$ is a matrix norm; let $T^n_{\boldsymbol{x}}$ be defined as the product $T^n_{\boldsymbol{x}} = T^1_{f^{(n-1)}(\boldsymbol{x})} \cdots T^1_{f(\boldsymbol{x})}\, T^1_{\boldsymbol{x}}$. Then there is a f-invariant subspace $N \subseteq M$ such that $\mu(N) = 1$ and $\forall \boldsymbol{x} \in N$ (indicating with A^* the adjoint of A) the matrix
>
> $$\Lambda_{\boldsymbol{x}} \coloneqq \lim_{n\to\infty} ((T^n_{\boldsymbol{x}})^* T^n_{\boldsymbol{x}})^{\frac{1}{2n}} \quad \text{exists.}$$
>
> It has $s \leq m$ distinct, real eigenvalues, that can be ordered as $\exp\lambda^{(1)}_{\boldsymbol{x}} > \ldots > \exp\lambda^{(s)}_{\boldsymbol{x}}$, corresponding to the eigenspaces $U^{(r)}_{\boldsymbol{x}}$; $r = 1, \ldots, s$. The $\lambda^{(r)}_{\boldsymbol{x}}$ exponents assume real values or can be $-\infty$ if the corresponding eigenvalue is 0.
>
> If we define $L^{(r)}_{\boldsymbol{x}} = U^{(r)}_{\boldsymbol{x}} \oplus U^{(r+1)}_{\boldsymbol{x}} \oplus \ldots \oplus U^{(s)}_{\boldsymbol{x}}$, and $L^{(s+1)}_{\boldsymbol{x}} = \{0\}$, we have that for $\boldsymbol{u} \in L^{(r)}_{\boldsymbol{x}}\backslash \in L^{(r+1)}_{\boldsymbol{x}}$
>
> $$\lim_{n\to\infty}\frac{1}{n}\log||T^n_{\boldsymbol{x}}\boldsymbol{u}|| = \lambda^{(r)}_{\boldsymbol{x}}\ ,$$
>
> i.e. the logarithms of the eigenvalues of $\Lambda_{\boldsymbol{x}}$ are the set of all LCE we can find from $\boldsymbol{x}$. Finally, defining $d^{(r)}_{\boldsymbol{x}} \coloneqq \dim U^{(r)}_{\boldsymbol{x}}$, we have that the functions $\boldsymbol{x} \to \lambda^{(r)}_{\boldsymbol{x}}$ and $\boldsymbol{x} \to d^{(r)}_{\boldsymbol{x}}$ are f-invariant ($\lambda^{(r)}_{\boldsymbol{x}} = \lambda^{(r)}_{f^t(\boldsymbol{x})}$, etc.) and, if the system is ergodic, are almost everywhere constant (with the possible exception of a set of 0 measure).

The matrix $\Lambda_{\boldsymbol{x}}$ is called Oseledec Matrix. If we write the vector norm as a scalar product $||\boldsymbol{u}|| = \sqrt{\langle \boldsymbol{u}, \boldsymbol{u}\rangle}$; the expansion rate after a single iteration is:

$$\frac{||T^1_{\boldsymbol{x}}\boldsymbol{u}||}{||\boldsymbol{u}||} = \sqrt{\frac{\langle T^1_{\boldsymbol{x}}\boldsymbol{u},\, T^1_{\boldsymbol{x}}\boldsymbol{u}\rangle}{\langle \boldsymbol{u},\, \boldsymbol{u}\rangle}} = \sqrt{\frac{\langle (T^1_{\boldsymbol{x}})^* T^1_{\boldsymbol{x}}\boldsymbol{u},\, \boldsymbol{u}\rangle}{\langle \boldsymbol{u},\, \boldsymbol{u}\rangle}}\ ;$$

the last equality comes from the definition of adjoint matrix. Now, assuming $\boldsymbol{u}$ is an eigenvector of $(T^1_{\boldsymbol{x}})^* T^1_{\boldsymbol{x}}$ with eigenvalue k, the result is:

$$\sqrt{\frac{\langle (T^1_{\boldsymbol{x}})^* T^1_{\boldsymbol{x}} \boldsymbol{u},\, \boldsymbol{u}\rangle}{\langle \boldsymbol{u},\, \boldsymbol{u}\rangle}} = \sqrt{\frac{\langle \boldsymbol{u},\, \boldsymbol{u}\rangle\, k}{\langle \boldsymbol{u},\, \boldsymbol{u}\rangle}} = \sqrt{k}\,. \tag{1.5}$$

This explanation has the only purpose of describing the idea behind the construction of the Oseledec matrix. For a full description of the theorem and its relation with the Lyapunov exponents, see [11, 17, 18]. An exhaustive mathematical demonstration can be found in [19]. The Oseledec multiplicative ergodic theorem is not simply an alternative way to express the Lyapunov exponents, but more than that, it states the existence of such a limit as an invariant property of the dynamical system, independent from the initial point chosen for time evolution.

The folding vector spaces $L^{(1)}_{\boldsymbol{x}} \supseteq L^{(2)}_{\boldsymbol{x}} \ldots \supseteq L^{(s)}_{\boldsymbol{x}}$ induce a natural splitting on the tangent space, known as *Oseledec splitting*. The importance of such splitting can be illustrated as follows: if we take a random vector $\boldsymbol{u}$ belonging to $T_{\boldsymbol{x}}M$, its mean grow rate will be $\exp \lambda^{(1)}_{\boldsymbol{x}}$, i.e. the exponential of the highest Lyapunov exponent. This comes from the fact that $\boldsymbol{u} \in L^{(1)}_{\boldsymbol{x}}$: the subspaces $L^{(2)}_{\boldsymbol{x}}$, $L^{(3)}_{\boldsymbol{x}} \ldots$ have zero measure with respect to the total space, so the probability of a random vector to be limited to them in substantially zero. However, if we consider a random vector $\tilde{\boldsymbol{u}}$ from which we systematically remove the component in the direction(s) of highest expansion, i.e. its projection on $U^{(1)}_{\boldsymbol{x}}$, then $\tilde{\boldsymbol{u}} \in L^{(2)}_{\boldsymbol{x}}$ and its LCE will be the second highest exponent, $\lambda^{(2)}_{\boldsymbol{x}}$, and so on. The numerical calculation of the complete spectrum of LCE is essentially based on this mechanism. We can also notice that the ordering of the spectrum induces different orders of expansion (and stability, for negative LCEs) in different subspaces.

Moreover, the basis of each $U^{(r)}_{\boldsymbol{x}}$ subspace (i.e. the $\Lambda_{\boldsymbol{x}}$ normalized eigenvectors), represents the (average) direction associated to the expanding (or contracting) average rate $\exp \lambda^{(r)}_{\boldsymbol{x}}$. Such directions are called *Lyapunov vectors* and, as described in section 1.4, can be computed and studied *locally*, in order to gain useful information on the local dynamics and global dynamics.

1.3 Calculating Lyapunov Exponents

The classical algorithm for the calculation of the Lyapunov exponents dates back to 1980 [20]. It considers only dynamical systems whose governing equations are fully known and computable. If the dynamics is hidden, it is still possible to estimate some of the exponents by using an empirical time series of some observable of the system. In [21], for example, both cases are considered (see also [22]). However, for the scope of the present work, we will stick to the hypothesis of the classical algorithm.

Following the reasoning of the original article, we start with the procedure for the first, highest exponent, and then we generalize the result to the whole spectrum. First of all we remind that for a starting point in our manifold $\boldsymbol{x} \in M$ and a vector in its tangent space $\boldsymbol{u} \in T_{\boldsymbol{x}}M$, the linear operator involved in the push-forward $(\boldsymbol{x}, \boldsymbol{u}) \to (f^t(\boldsymbol{u}), T^t_{\boldsymbol{x}}\boldsymbol{u})$ is the Jacobian of f^t calculated in point

$\boldsymbol{x}$. This value is basically the complete derivative of f^t: in section 2.6 of next chapter we will show the calculation in our specific setting. For now we assume the $T^t_{\boldsymbol{x}}$ matrices as given for every $\boldsymbol{x}$ in M.

As said in previous section, for the first exponent is sufficient to follow the evolution of a random vector $\boldsymbol{u}_0$. To have an intuitive representation of the process, we can imagine to decompose $\boldsymbol{u}_0$ in the basis of the directions of expansion associated to each exponent (i.e. the Lyapunov vectors). Being random, our starting vector will have a nonzero component for each direction. Due to the linearity of the process each component will increase, on average, exponentially, according to the respective Lyapunov exponent. The exponential difference of the growing rates will cause the component associated to the highest exponent to dominate over all the others after a short amount of iterations, so that it is the only one selected in the large n limit.

The only difficulty is that an exponentially growing vector would soon go out of the boundaries of our computational capabilities (that's basically the reason why we cannon calculate $\Lambda_{\boldsymbol{x}}$ directly). It is solved as follows. Given an integer $k \gtrsim 1$ such that $T^k_{\boldsymbol{x}}$ lies safely in our numeric limits, we start with a random vector $\boldsymbol{u}_0 \in T_{\boldsymbol{x}}M$ and calculate iteratively the series:

$$\boldsymbol{u}_1 = T^k_{\boldsymbol{x}} \frac{\boldsymbol{u}_0}{||\boldsymbol{u}_0||} , \qquad \boldsymbol{u}_2 = T^k_{f^k(\boldsymbol{x})} \frac{\boldsymbol{u}_1}{||\boldsymbol{u}_1||} , \qquad \boldsymbol{u}_3 = T^k_{f^2k(\boldsymbol{x})} \frac{\boldsymbol{u}_2}{||\boldsymbol{u}_2||} , \ldots$$

$$\boldsymbol{u}_i = T^k_{f^{(i-1)k}(\boldsymbol{x})} \frac{\boldsymbol{u}_{i-1}}{||\boldsymbol{u}_{i-1}||} = \frac{T^k_{f^{(i-1)k}}(\boldsymbol{x})\, T^k_{f^{(i-2)k}}(\boldsymbol{x}) \ldots T^k_{f^k(\boldsymbol{x})} \boldsymbol{u}_0}{||\boldsymbol{u}_{i-1}||\, ||\boldsymbol{u}_{i-2}|| \ldots ||\boldsymbol{u}_0||} ;$$

$||T^{ik}_{\boldsymbol{x}} \boldsymbol{u}_0|| = ||\boldsymbol{u}_i||\, ||\boldsymbol{u}_{i-1}|| \ldots ||\boldsymbol{u}_0|| ;$ finally, from $\boldsymbol{u}_0 \in L^{(1)}_{\boldsymbol{x}}$ and (1.3), we have:

$$\lambda^{(1)}_{\boldsymbol{x}} = \lim_{n\to\infty} \frac{1}{n} \sum_{i=1}^{n} \log ||\boldsymbol{u}_i|| . \tag{1.6}$$

Both the fact that $T^k_{\boldsymbol{x}}$ is applied only to normalized vectors and that the logarithm is computed at every single step have the positive effect of containing the size of the numbers involved, making the computation possible.

To calculate the whole spectrum, we must think in terms of volume variations. We assume the $\Lambda_{\boldsymbol{x}}$ matrix to be m dimensional and, for simplicity, that all its eigenvalues have multiplicity one (i.e. we have m distinct LCE). Let $U \subset T_{\boldsymbol{x}}M$ be a open set of volume $\mathrm{Vol}(U)$; using the definition of LCE and the Oseledec theorem, we infer that its average growing rate in time is $\propto \exp \sum_{i=1}^{m} \lambda^{(i)}_{\boldsymbol{x}}$.

We start from U_0, defined for convenience as the m-dimensional hypercube enclosed in a random orthonormal basis of $T_{\boldsymbol{x}}M$: $\{\boldsymbol{u}^{(1)}_0, \boldsymbol{u}^{(2)}_0, \ldots \boldsymbol{u}^{(m)}_0\}$; Let A be the linear operator corresponding to a single time iteration of the set. Following the same reasoning as before, we define iteratively the sets U_i as:

$$U_i = \frac{A(U_{i-1})}{\mathrm{Vol}(U_{i-1})} ;$$

so that, from the linearity of A, it follows:

$$\mathrm{Vol}(U_i) \cdot \mathrm{Vol}(U_{i-1}) \cdot \ldots \cdot \mathrm{Vol}(U_0) = \mathrm{Vol}(AA \ldots AU_0) .$$

The quantity on the right is the volume of our initial hypercube after i timesteps, namely:

$$\mathrm{Vol}(AA\dots AU_0) = \mathrm{Vol}(T^{ik}_{\boldsymbol{x}}\boldsymbol{u}^{(1)}_0,\, T^{ik}_{\boldsymbol{x}}\boldsymbol{u}^{(2)}_0, \dots\, T^{ik}_{\boldsymbol{x}}\boldsymbol{u}^{(m)}_0)\ ;$$

this expression leads to the sum of all LCE:

$$\lim_{n\to\infty}\frac{1}{n}\log\frac{\mathrm{Vol}(A^nU_0)}{\mathrm{Vol}(U_0)} = \lim_{n\to\infty}\frac{1}{n}\log\left(\mathrm{Vol}(A^nU_0)\right) = \sum_{j=1}^{m}\lambda^{(j)}_{\boldsymbol{x}}\ .$$

The quantities on the left assume the form:

$$\mathrm{Vol}(U_i) = \frac{\mathrm{Vol}(A(U_{i-1}))}{\mathrm{Vol}(U_{i-1})} = \tag{1.7}$$
$$= \frac{\mathrm{Vol}(T^k_{f^{(i-1)k}(\boldsymbol{x})}\boldsymbol{u}^{(1)}_{i-1},\, T^k_{f^{(i-1)k}(\boldsymbol{x})}\boldsymbol{u}^{(2)}_{i-1}, \dots\, T^k_{f^{(i-1)k}(\boldsymbol{x})}\boldsymbol{u}^{(m)}_{i-1})}{\mathrm{Vol}(U_{i-1})}\ .$$

By iterating the vectors as before ($\boldsymbol{u}^{(j)}_i = T^k_{f^{(i-1)}(\boldsymbol{x})}\boldsymbol{u}^{(j)}_{i-1}/||\boldsymbol{u}^{(j)}_{i-1}||$) and computing the volume for each step, we can, in principle, find the right result; however this method is not feasible, due to the fact that all vectors would soon converge on the direction of maximum expansion, so that the angles between them are beyond the numerical resolution and the volume cannot be calculated.

To circumvent this problem, for each timestep we recompute the vectors defining the volume U_i performing a Gram-Schmidt orthogonalization procedure: U_i does not change, and its volume simply becomes the product of the orthogonal vector norms. In short, if we assume $\langle\cdot,\cdot\rangle$ as the scalar product in the space $T_{f^{ik}(\boldsymbol{x})}M$, we build the series of $\boldsymbol{u}^{(j)}_i$ as:

$$\begin{aligned}
\boldsymbol{u}^{(1)}_i &= T^k_{f^{(i-1)k}(\boldsymbol{x})}\frac{\boldsymbol{u}^{(1)}_{i-1}}{||\boldsymbol{u}^{(1)}_{i-1}||}\ ; \quad \text{for } j>1: \\
\boldsymbol{u}^{(j)}_i &= T^k_{f^{(i-1)k}(\boldsymbol{x})}\frac{\boldsymbol{u}^{(j)}_{i-1}}{||\boldsymbol{u}^{(j)}_{i-1}||} - \sum_{r=1}^{j-1}\left\langle T^k_{f^{(i-1)k}(\boldsymbol{x})}\frac{\boldsymbol{u}^{(j)}_{i-1}}{||\boldsymbol{u}^{(j)}_{i-1}||},\ \boldsymbol{u}^{(r)}_i\right\rangle\frac{\boldsymbol{u}^{(r)}_i}{||\boldsymbol{u}^{(r)}_i||^2}\ .
\end{aligned} \tag{1.8}$$

With this definition $\mathrm{Vol}^p(T^k_{f^{(i-1)k}(\boldsymbol{x})}\boldsymbol{u}^{(1)}_{i-1},\, T^k_{f^{(i-1)k}(\boldsymbol{x})}\boldsymbol{u}^{(2)}_{i-1}, \dots\, T^k_{f^{(i-1)k}(\boldsymbol{x})}\boldsymbol{u}^{(m)}_{i-1})$ is equivalent to:

$$\left(\prod_{j=1}^{m}||\boldsymbol{u}^{(j)}_{i-1}||\right)\cdot\mathrm{Vol}^p(\boldsymbol{u}^{(1)}_i,\, \boldsymbol{u}^{(2)}_i, \dots\, \boldsymbol{u}^{(m)}_i) = \left(\prod_{j=1}^{m}||\boldsymbol{u}^{(j)}_{i-1}||\right)\cdot\left(\prod_{j=1}^{m}||\boldsymbol{u}^{(j)}_i||\right)\ .$$

The last equality is due to the orthogonality of the $\boldsymbol{u}^{(j)}_i$ vectors. From (1.7) we obtain $\mathrm{Vol}^p(U_i) = \prod_{j=1}^{m}||\boldsymbol{u}^{(j)}_i||$, which leads to the result:

$$\sum_{j=1}^{m}\lambda^{(j)}_{\boldsymbol{x}} = \lim_{n\to\infty}\frac{1}{n}\log\left(\prod_{j=1}^{m}||\boldsymbol{u}^{(j)}_0||\cdot\prod_{j=1}^{m}||\boldsymbol{u}^{(j)}_1||\cdot\ldots\prod_{j=1}^{m}||\boldsymbol{u}^{(j)}_n||\right)\ .$$

Rearranging the product indexes and decomposing the logarithm, we finally obtain, for the s^{th} exponent:

$$\lambda_{\boldsymbol{x}}^{(j)} = \lim_{n\to\infty} \frac{1}{n} \sum_{i=1}^{n} \log ||\boldsymbol{u}_i^{(j)}|| \,. \tag{1.9}$$

Equation (1.9) is an extended version of (1.6), with the significant difference that the $\boldsymbol{u}_i^{(j)}$ vectors, for $j > 1$, are calculated according to the orthonormalization procedure (1.8). As we will see in section 1.5 this process can be simply and straightforwardly translated in basic operation on matrices.

Before moving to the calculation of Lyapunov vectors, some considerations about dimensions should to be done. The result of (1.9) is dimensionless, as it represents the logarithm of average expansion *per step*. To obtain a more general quantity, independent of the step lengths used for the evolution of the dynamical system (as long as the intervals are small enough to follow properly the dynamical evolution), we need to rescale the exponents using the duration of a timestep Δt:

$$\lambda_i^{(j)} \leftarrow \frac{\lambda_i^{(j)}}{\Delta t} \tag{1.10}$$

The coefficients are thus expressed in seconds^{-1}.

The system analyzed the present work has the peculiarity of having steps of different time lengths. Since the LCE is defined as an average quantity, we divide it by the interval length averaged on all performed steps: $[\Delta t]_s$ (see for example pag. 120 of [14]).

1.4 Calculating the (local) Lyapunov vectors

As said, the Lyapunov vectors, defined as a base for the eigenspaces of Λ_x, represent the direction of the global average expansion associated to each exponent. It is then possible to define the *local* Lyapunov vectors as the preferred expanding directions for the (linearized) dynamics of each point in time. The local Lyapunov exponents are then the punctual expansion rates in each of those directions.

The identification at any step s of the maximum local exponent $\lambda_s^{(1)}$ and its associated direction $\boldsymbol{v}_s^{(1)}$ is straightforward: as said, a random vector, freely evolving in time, would rapidly align with it. So that, using the $\boldsymbol{u}_s^{(1)}$ vectors as defined above, we obtain, for the vector and the exponent:

$$\boldsymbol{v}_s^{(1)} = \frac{\boldsymbol{u}_s^{(1)}}{||\boldsymbol{u}_s^{(1)}||} \,; \qquad \lambda_s^{(1)} = \log \left(\frac{||T^k_{f^{ik}(\boldsymbol{x})} \boldsymbol{u}_s^{(1)}||}{||\boldsymbol{u}_s^{(1)}||} \right) = \log ||\boldsymbol{u}_{(s+1)}^{(1)}|| \,, \tag{1.11}$$

for values of s reasonably distant from 0, so that $\boldsymbol{u}^{(1)}$ has sufficient time to align, and assuming that the mapping is smooth enough, so the vector properly follows the dominating direction at every point in time.

Moving to $\boldsymbol{v}_s^{(2)}$ and $\lambda_s^{(2)}$, the idea in the series (1.8) is that, after we apply the linear operator, we project the resulting vector on the space orthogonal to $\boldsymbol{v}_s^{(1)}$,

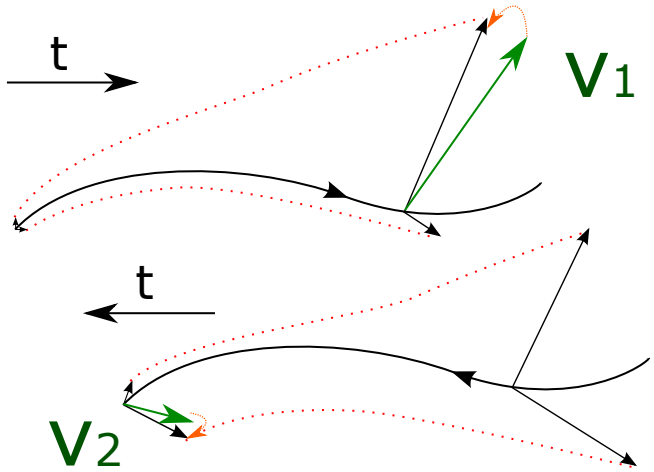

Figure 1.2: In a chaotic dynamical system any perturbation will converge on the direction of the first Lyapunov vector. On the other hand, a time inversion in the dynamics results in the marked domination of the least forward expanding direction, i.e. the second vector.

thus the growth in that direction direction (expected to be dominating) is completely suppressed, while the next highest growing direction, regulated by $\lambda_s^{(2)}$, becomes visible. As a result, $\boldsymbol{u}_s^{(2)}/||\boldsymbol{u}_s^{(2)}||$ has the same direction as *the projection* of $\boldsymbol{v}_s^{(2)}$ on the space perpendicular to $\boldsymbol{v}_s^{(1)}$. In general $\boldsymbol{u}_s^{(2)}/||\boldsymbol{u}_s^{(2)}|| \neq \boldsymbol{v}_s^{(2)}$: no reason forces the Lyapunov vectors, either global or local, to be perpendicular each other. Lacking the knowledge of the correct direction and of the local exponent defined as above (it cannot be found it the corresponding direction is not known), we cannot calculate the true $\boldsymbol{v}_s^{(2)}$.

A solution to circumvent this problem has been proposed only in 2007 [23]. It is based on the quite intuitive and well know principle that a time-inversion in the dynamics of our system inverts the Lyapunov spectrum. A volume normally expanding in some directions, in a backward motion would contract in those same directions with inverted ratios, while a random vector traveling backwards in time would soon follow the direction of less expansion in forward time. See figure 1.2 to have a graphical idea of the process.

For the arguments above, we know that $\text{Span}(\boldsymbol{v}_s^{(1)}, \boldsymbol{v}_s^{(2)}) = \text{Span}(\boldsymbol{u}_s^{(1)}, \boldsymbol{u}_s^{(2)})$. If we take a random combination of $\boldsymbol{u}_s^{(1)}$ and $\boldsymbol{u}_s^{(2)}$ and evolve it backwards, after some iteration (let's say h) it will be aligned with the less *forward* expanding direction of our subspace, namely $\boldsymbol{v}_{s-h}^{(2)}$. For vector $\boldsymbol{v}_{s-h}^{(s)}$ we simply start with a linear combination of vectors $\boldsymbol{v}_s^{(1)}$, $\boldsymbol{u}_s^{(2)}$, $\ldots$ $\boldsymbol{u}_s^{(s)}$, keeping in mind that h should be big enough to let the vectors align properly.

1.5 Matrix Calculation

As said, there is a simple and elegant way to translate the algorithms described above in a sequence of matrix operations. If m is the dimension of our system,

we start defining a random, orthonormal, $m \times m$ matrix whose columns represent a basis for $T_{\boldsymbol{x}}M$: $Q_0 = (\boldsymbol{q}_0^{(1)}|\dots|\boldsymbol{q}_0^{(m)})$. Due to their structure, the $\boldsymbol{q}^{(j)}$ vectors, i.e. the columns of the Q matrix, are called *the Gram-Schmidt basis*.

$T^k_{\boldsymbol{x}}$ is the Jacobian matrix associated to a k-steps evolution, with k chosen so that the exponential growths are kept in the numerical limits of our calculator. We now perform the multiplication:

$$T^1_{\boldsymbol{f^{k-1}}x} \dots T^1_{\boldsymbol{f^1 x}} \cdot Q_0 = (T^k_{\boldsymbol{x}} \boldsymbol{q}_0^{(1)}|\dots|T^k_{\boldsymbol{x}} \boldsymbol{q}_0^{(m)}) = (\tilde{\boldsymbol{q}}_1^{(1)}|\dots|\tilde{\boldsymbol{q}}_1^{(m)}) = \tilde{Q}_1 \; ; \quad (1.12)$$

where $T^1_x \dots T^1_{f^{k-1}x}$ are the Jacobian matrices for a single timestep, computed for the specific dynamical system we are analyzing.

The vectors $\tilde{\boldsymbol{q}}_1^{(j)}$ are not orthogonal. To obtain the correct iterated $\boldsymbol{Q}_1$ matrix, we apply a QR decomposition on $\tilde{Q}_1$. The QR decomposition on a generic square matrix $\tilde{Q}$ consists in writing it as the product $\tilde{Q} = Q \cdot R$, such that Q is *orthonormal* and R is *upper triangular*. Calling $\tilde{\boldsymbol{q}}^{(j)}$ and $\boldsymbol{q}^{(j)}$ the columns of, respectively, $\tilde{Q}$ and Q, the new matrices are defined by:

$$\boldsymbol{q}^{(1)} = \frac{\tilde{\boldsymbol{q}}^{(1)}}{||\tilde{\boldsymbol{q}}^{(1)}||} \; ; \qquad \boldsymbol{q}^{(j)} = \frac{\tilde{\boldsymbol{q}}^{(j)} - \sum_{r=1}^{j-1} \left\langle \tilde{\boldsymbol{q}}^{(j)},\, \boldsymbol{q}^{(r)} \right\rangle \boldsymbol{q}^{(r)}}{\left|\left| \tilde{\boldsymbol{q}}^{(j)} - \sum_{r=1}^{j-1} \left\langle \tilde{\boldsymbol{q}}^{(j)},\, \boldsymbol{q}^{(r)} \right\rangle \boldsymbol{q}^{(r)} \right|\right|} \quad (1.13)$$

$$\{R\}_{ij} = \left\langle \boldsymbol{q}^{(i)},\, \tilde{\boldsymbol{q}}^{(j)} \right\rangle \; , \quad \text{for } i \leq j \; .$$

It is straightforward to see that these values can be expressed in terms of the $\boldsymbol{u}^{(j)}$ vectors (1.8) as $\boldsymbol{q}_1^{(1)} = \boldsymbol{u}_1^{(1)}/||\boldsymbol{u}_1^{(1)}|| \dots \boldsymbol{q}_1^{(m)} = \boldsymbol{u}_1^{(m)}/||\boldsymbol{u}_1^{(m)}||$ Moreover, from the definition of the QR algorithm descends that the diagonal of the R matrix corresponds to the $\boldsymbol{u}_1^{(j)}$ norms: $\{R_1\}_{jj} = ||\boldsymbol{u}_1^{(j)}||$.

The orthonormalized Q_1 is now ready for another iteration:

$$T^1_{\boldsymbol{f^{2k-1}}x} \dots T^1_{\boldsymbol{f^k x}} \cdot Q_1 = \tilde{Q}_2 = Q_2 \cdot R_2 \quad \dots \text{and so on.}$$

The $\boldsymbol{u}_i^{(j)}$ vector modules, given by the diagonal of R_i, are stored in each iteration for the calculation of the Lyapunov spectrum.

This same setting, along with the results already computed, can be also used to find the Lyapunov vectors. The ending point of our computation $T \gg 1$ will be assumed as the starting point of our backward iteration. The starting random vectors $\boldsymbol{v}_T^{(1)} \in \text{Span}\{\boldsymbol{u}_T^{(1)}\}$, $\boldsymbol{v}_T^{(2)} \in \text{Span}\{\boldsymbol{u}_T^{(1)}, \boldsymbol{u}_T^{(2)}\}$ …, $\boldsymbol{v}_T^{(m)} \in \text{Span}\{\boldsymbol{u}_T^{(1)}, \dots \boldsymbol{u}_T^{(m)}\}$ can be defined as the product of Q_T with a random triangular matrix C_T. Considering the time iteration, we obtain:

$$Q_T \cdot C_T = T^k_{f^{(1-T)k}(\boldsymbol{x})} \cdot Q_{T-1} \cdot C_{T-1} = \tilde{Q}_T \cdot C_{T-1} = Q_T \cdot R_T \cdot C_{T-1} \; ;$$
$$\text{so that} \qquad C_{T-1} = (R_T)^{-1} \cdot C_T \; . \quad (1.14)$$

The previously calculated triangular R_s matrices must thus be fully stored, inverted and used to iterate backward in time the C_i matrix:

$$C_i = (R_{i-1})^{-1} \cdot (R_{i-2})^{-1} \cdot \dots \cdot (R_T)^{-1} \cdot C_T \; .$$

Since we are interested only in the vector directions, we can freely normalize the columns of the C_i matrices. If we do that at every step, we can identify the normalization factors at point i with the local Lyapunov exponents $\lambda_s^{(j)}$, while the Lyapunov local vectors are simply the (normalized) columns of $Q_s \cdot C_s$.

1.6 Information and Entropy

Consider two points very close one another in the phase-space of a chaotic system: for any observer whose instruments have a precision coarser than their distance, they will appear completely indistinguishable. Eventually, as the system evolves in time, the trajectory separation due to chaotic dynamics makes the distance significant, so that the points are perceived as separate. Thus, systems very sensitive to initial conditions can be seen as producers of information.

Let $\{\mathcal{A}_1,\ \mathcal{A}_2,\ \ldots, \mathcal{A}_\alpha\}$ be a finite, μ-measurable partition of the phase space. We can assume it corresponds to the resolution of our instruments, so that two points in the same set of the partition $\mathcal{A}$ cannot be seen as distinct. We can then define $f^{-k}(\mathcal{A}_i)$ as the set of points $\boldsymbol{x}$ such that $f^k(\boldsymbol{x}) \in \mathcal{A}_i$, and call $f^{-k}(\mathcal{A}\ )$ the partition $\{f^{-k}(\mathcal{A}_1),\ \ldots f^{-k}(\mathcal{A}_\alpha)\}$. We finally consider the partition given by the least common refinement:

$$\mathcal{A}^{(n)} = \mathcal{A} \vee f^{-1}(\mathcal{A}\ ) \vee f^{-2}(\mathcal{A}\ ) \vee \ldots \vee f^{1-n}(\mathcal{A}\ )\ ;$$

it is defined so that a generic set in it has the form:

$$\mathcal{A}_{i_1} \cap f^{-1}(\mathcal{A}_{i_2}) \cap \ldots \cap f^{1-n}(\mathcal{A}_{i_n}) \qquad \text{for} \quad i_j \in \{1, 2,\ \ldots, \alpha\}$$

It is clear that the latter, dynamics-related, partition has a resolution much finer than the starting one, since any element in it is discriminated by its past history, up to $n-1$ steps.

Now, we can define the information content of the partition $\mathcal{A}^{(n)}$ with respect to measure μ as:

$$H(\mathcal{A}^{(n)}) = \sum_{i_1,\ldots,i_n} \mu(\mathcal{A}_{i_1} \cap \ldots \cap f^{1-n}\mathcal{A}_{i_n}) \log \mu(\mathcal{A}_{i_1} \cap \ldots \cap f^{1-n}\mathcal{A}_{i_n})\ ;$$

where we sum over every element of $\mathcal{A}^{(n)}$. The rate of information creation, with respect to the initial partition $\mathcal{A}$ is then given by the limit:

$$\hbar(\mu, \mathcal{A}) = \lim_{n\to\infty} \left(H(\mathcal{A}^{(n+1)}) - H(\mathcal{A}^{(n)}) \right) = \lim_{n\to\infty} \left(\frac{1}{n} H(\mathcal{A}^{(n)}) \right)\ .$$

The Shannon-MacMillan theorem guarantees the existence of this limit.

The Kolgomorov-Sinai entropy $\hbar(\mu)$ is then defined as the further limit of $\hbar(\mu, \mathcal{A})$ for finer and finer starting partitions $\mathcal{A}$.

As stated at the beginning of this section, the information creation rate is originated by the expanding motion of the system in the phase space, connected with its chaotic behavior. In 1978 Ruelle demonstrated that its value cannot be greater than the total positive expansion rate of the system, given by the sum over all positive Lyapunov global exponents:

$$\hbar(\mu) \leq \sum_{\lambda^{(i)}>0} \lambda^{(i)}\ . \tag{1.15}$$

Pesin extended this theorem, proving that (1.15) is an identity if (and only if) the measure μ is a *SRB measure*. We shall briefly define and discuss SRB measures at the end of the next section, since they result crucial also in the valuation of the attractor dimension.

1.7 Information Dimension of the Attractor

As mentioned at the beginning of this chapter, (see pag 17) the attractor in the phase space $A \subseteq M$ has, in general, a fractal structure. We assume the notion of Hausdorff dimension as given, with the notation $\dim_H$, and define the *information dimension* of the measure μ as:

$$\dim_H(\mu) = \inf\{\dim_{\mathrm{H}}(S) | \mu(S) = 1\} .$$

Young's theorem (1982) shows that, if μ is an ergodic measure, this value is equivalent to:

$$\dim_{\mathrm{H}}(\mu) = \lim_{r \to 0} \frac{\log \mu(B_{\boldsymbol{x}}(r))}{\log r} .$$

Here $B_{\boldsymbol{x}}(r)$ represents the ball centered in $\boldsymbol{x}$ of diameter r. The expression is valid and constant for every $\boldsymbol{x} \in A$ except, possibly, for a set of 0 μ-measure.

Now, if $\lambda^{(1)}, \ldots, \lambda^{(m)}$ are the global Lyapunov exponents associated to μ, and $k = \max\{ i \mid \lambda^{(1)} + \ldots + \lambda^{(i)} \geq 0\}$, we can define the Lyapunov dimension as:

$$\dim_\Lambda(\mu) = k + \frac{\lambda^{(1)} + \ldots + \lambda^{(k)}}{|\lambda^{(k+1)}|} ; \tag{1.16}$$

the second term is a small, noninteger correction for the case: $\sum_{i=1}^{k} \lambda^{(i)} > 0$ and $\sum_{i=1}^{K+1} \lambda^{(i)} < 0$. In our system, due to great dimensionality, it results negligible.

The connection between the two quantities defined here is given by the following *conjecture* by Kaplan and Yorke: if μ is an ergodic, SRB measure, then

$$\dim_{\mathrm{H}}(\mu) = \dim_\Lambda(\mu) . \tag{1.17}$$

It is analytically proved that this equality holds in some specific cases, but exceptions are found.

SRB measures and hyperbolicity

In the previous two sections we stated that a crucial property of the measure we use, both for the *exact* calculation of entropy production and a *reasonable* esteem of the attractor dimension, is being a SRB measure (from Sinai, Ruelle, Bowen); namely a measure which is *absolutely continuous along unstable manifolds.* A rigorous definition can be found in [10, 11].

It is proved that for a class of dynamical systems, namely the *Axiom-A* systems, exists a unique SRB measure, which can be expressed "physically" as the ergodic average:

$$\rho = \lim_{n \to \infty} \frac{1}{n} \sum_{k=0}^{n-1} \delta_{f^k x} .$$

The problem is then transferred on demonstrating that the dynamical system is Axiom-A: in that case the SRB measure naturally corresponds to an average over long dynamical trajectories, as the ergodic principle states; consequently Pesin identity holds and Kaplan-Yorke conjecture is on solid ground.

The crucial property of Axiom-A system is *hyperbolicity.* A set A is hyperbolic for a diffeomorphism f (mapping of flow), if $\forall \boldsymbol{x} \in A$ there exists a direct sum

decomposition of the tangent space between *stable* (expanding over time) and *unstable* directions (expanding on *inverted* time). If A is a hyperbolic attracting set and the periodic points of f are dense in A, the conditions for an Axiom-A diffeomorphism are satisfied. In case the whole manifold M is hyperbolic, we have the stronger conditions of *Anisov diffeomorphism* and *structural stability*.

Proving that a system is Axiom-A is, in general, a very hard task. However, the present work represents an example of how Lyapunov Vectors can be used to identify the expanding and contracting directions of the tangent space. The measure of their transversality represents then a quantitative esteem of the global degree of hyperbolicity of the system.

Chapter 2

Model

In this chapter a basic model for a static, large scale network of cortical neurons is built. Starting form the Hodgkin-Huxley classic equations, simpler models are inferred. It is then explained why the canonical quadratic integrate and fire model (QIF) is a suitable to describe the dynamics of very large scale networks. In the next section a more general model for pulse-coupled neuronal networks is presented. Explicit equations are obtained from the QIF model and used to calculate analytically different global parameters of the network; then a formula for the Jacobian at any given spiketime is presented. Such analytical expressions will be the basis of the actual network simulation and of all the subsequent results presented in next chapters.

2.1 Single Neuron Dynamics

Hodgkin and Huxley model

The best known and most widely accepted equations used to describe the potential of a neural cell soma as a function of external current and internal conductance parameters, dates back to the pionieristic work of Hodgkin and Huxley [24]. The equations in their standard form are:

$$\begin{aligned} C\frac{dV}{dt} &= I - g_{\mathrm{L}}(V - E_{\mathrm{L}}) - g_{\mathrm{Na}} m^3 h (V - E_{\mathrm{Na}}) - g_{\mathrm{K}} n^4 (V - E_{\mathrm{K}}) \,; \\ \frac{dm}{dt} &= \frac{1}{\tau_m(V)} \left(m_\infty(V) - m\right) \,; \\ \frac{dh}{dt} &= \frac{1}{\tau_h(V)} \left(h_\infty(V) - h\right) \,; \\ \frac{dn}{dt} &= \frac{1}{\tau_n(V)} \left(n_\infty(V) - n\right) \,; \end{aligned} \tag{2.1}$$

$$\begin{aligned} \text{with} \quad & m_\infty(V) = \alpha_m(V)/(\alpha_m(V) + \beta_m(V)) \,, \quad && \tau_m(V) = 1/(\alpha_m(V) + \beta_m(V)) \,, \\ & h_\infty(V) = \alpha_h(V)/(\alpha_h(V) + \beta_h(V)) \,, && \tau_h(V) = 1/(\alpha_h(V) + \beta_h(V)) \,, \\ & n_\infty(V) = \alpha_n(V)/(\alpha_n(V) + \beta_n(V)) \,, && \tau_n(V) = 1/(\alpha_n(V) + \beta_n(V)) \,. \end{aligned}$$

The variable I represents the current, C is the membrace capacitance, the $E_\bullet$ are the Nerst equilibrium potentials, while the g parameters are the maximal conductance for Na^+ ions, K^+ ions and other ions (leakage currents). The m, h, n functions are biologically interpreted as the open fraction of independent gates which compose each single ion channel. One Na^+ channel is open only if its three m-type gates and one h-type gate are open, while a K^+ channel is composed of four n gates. Such functions depend on the steady state activation parameters m_∞, h_∞, n_∞ and on the activation time constants τ_m, τ_h, τ_n.

A proper choice of parameters, often fitted on *in vitro* and *in vivo* voltage-clamp measures on living cells, makes the observation of a wide variety of behaviors, corresponding to different kinds of neural cells, possible. We can divide neurons in two main classes of excitability. Neurons of class 1, also called Type 1 neurons, are able to produce action potential trains with frequencies varying smoothly on a wide range $\sim 1 - 100\ Hz$. Neurons of class 2 have an "all or none" kind of response, with a fixed spike frequency $\sim 150 - 200\ Hz$, arising when the incoming current increases over a certain threshold. For the scope of the present work we consider only class 1 neurons.

A complete derivation of the Hodgkin and Huxley equations and a detailed explanation for their dynamics can be found in the original article [24] or in [25, 26, 27]).

Reduction to Two Dimensions

One of the first and most well-known reduction of the (2.1) comes from the work by C. Morris and H. Lecar on the muscle fibers of the barnacle [28]. Since we are directed to the study neocortex rather than muscular fibers, we will use a model dynamically equivalent, the *persistent sodium slow potassium* or $I_{\mathrm{Na,p}} + I_{\mathrm{K}}$ model, introduced in 1993 by X. J. Wang to simulate the behavior of pyramidal neurons of the cat sensorimotor cortex [29]. The equations are:

$$\begin{aligned} C\frac{dV}{dt} &= I - g_{\mathrm{L}}(V - E_{\mathrm{L}}) - g_{\mathrm{Na}} m_\infty(V)(V - E_{\mathrm{Na}}) - g_{\mathrm{K}} n (V - E_{\mathrm{K}})\,; \\ \frac{dn}{dt} &= \frac{n_\infty(V) - n}{\tau(V)}\,; \end{aligned} \tag{2.2}$$

$$m_\infty(V) = \frac{1}{1 + \exp\frac{V_{m,1/2} - V}{K_m}} \qquad n_\infty(V) = \frac{1}{1 + \exp\frac{V_{n,1/2} - V}{K_n}} \tag{2.3}$$

Unlike the Hodgkin-Huxley model, here each channel is composed by a single gate, and the sodium channels react istantaneously to voltage change (i.e. on a timescale much lower than the potassium channels). It should be pointed out that this model is less biologically meaningful, and lacks, even qualitatively, some dynamics intrinsic in the HH equations (see [30]). On the other hand it is easier to study with the standard procedure used for two dimensional dynamical systems, as and covers the specific regime we are interested in.

Equations (2.2) can be qualitatively investigated with the approach and formalism used for generic 2-dimensional dynamical systems, such as the Van der

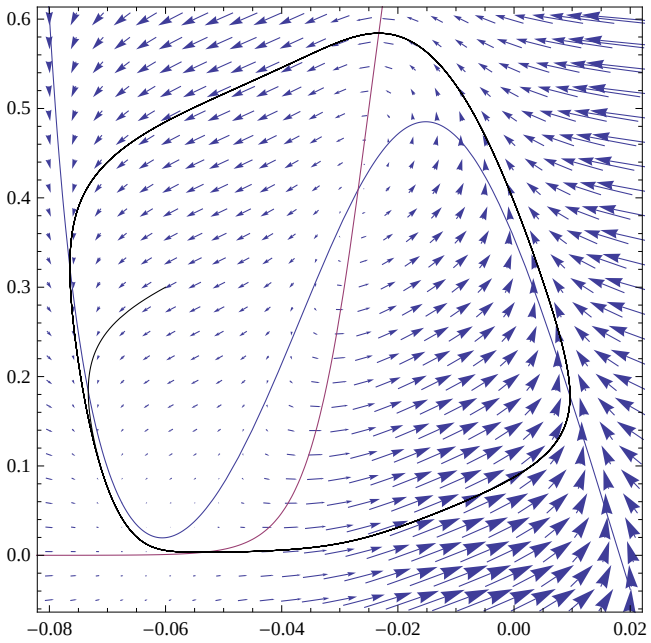

Figure 2.1: Nullclines, vector field and an example of trajectory for the $I_{\mathrm{Na,p}} + I_{\mathrm{K}}$ model. It is clear that for almost all staring points the dynamics will fall on the periodic attractor. The parameters used are in table 2.1

Table 2.1: Parameters used for the $I_{\mathrm{Na,p}} + I_{\mathrm{K}}$ model, taken from in-vivo measures on a rat as reported in [25]

$C = 1$ mF,	$I = 0.01$ mA/cm^2,	$g_{\mathrm{L}} = 8$ mS/cm^2,	$E_{\mathrm{L}} = -80$ mV,
$K_n = 5$ mV,	$V_{n,1/2} = -25$ mV,	$g_{\mathrm{Na}} = 20$ mS/cm^2,	$E_{\mathrm{K}} = -90$ mV,
$K_m = 15$ mV,	$V_{m,1/2} = -20$ mV,	$g_{\mathrm{K}} = 10$ mS/cm^2,	$E_{\mathrm{Na}} = -60$ mV,
$\tau(V) \equiv 1$.			

Pol oscillator [12, 31]. We draw the *nullclines*, i.e. the curves $dV/dt = 0$ and $dn/dt = 0$, in the $V - n$ diagram. Solving the (2.2) we have:

$$\begin{aligned} n_{\mathrm{null}\ n} &= n_\infty(V)\ ; \\ n_{\mathrm{null}\ V} &= \frac{I - g_{\mathrm{L}}(V - E_{\mathrm{L}}) - g_{\mathrm{Na}} m_\infty(V)(V - E_{\mathrm{Na}})}{g_{\mathrm{K}}(V - E_{\mathrm{K}})}\,. \end{aligned} \tag{2.4}$$

In figure 2.1 the nullclines and the vector field of the velocities $(dV/dt,\ dn/dt)$ are plotted. The parameters used are modeled on fits of patch-clamp measures on pyramidal neurons of the rat's visual cortex, as reported on [25], and are shown in table 2.1.

With this choice, the result a is periodic movement on an invariant cycle, as shown in figure 2.1. Changing the parameters, a wide variety of dynamics can be reproduced, all described in detail in the reference cited above. For the scope of the present dissertation, however, it is enough to consider slow changes in the

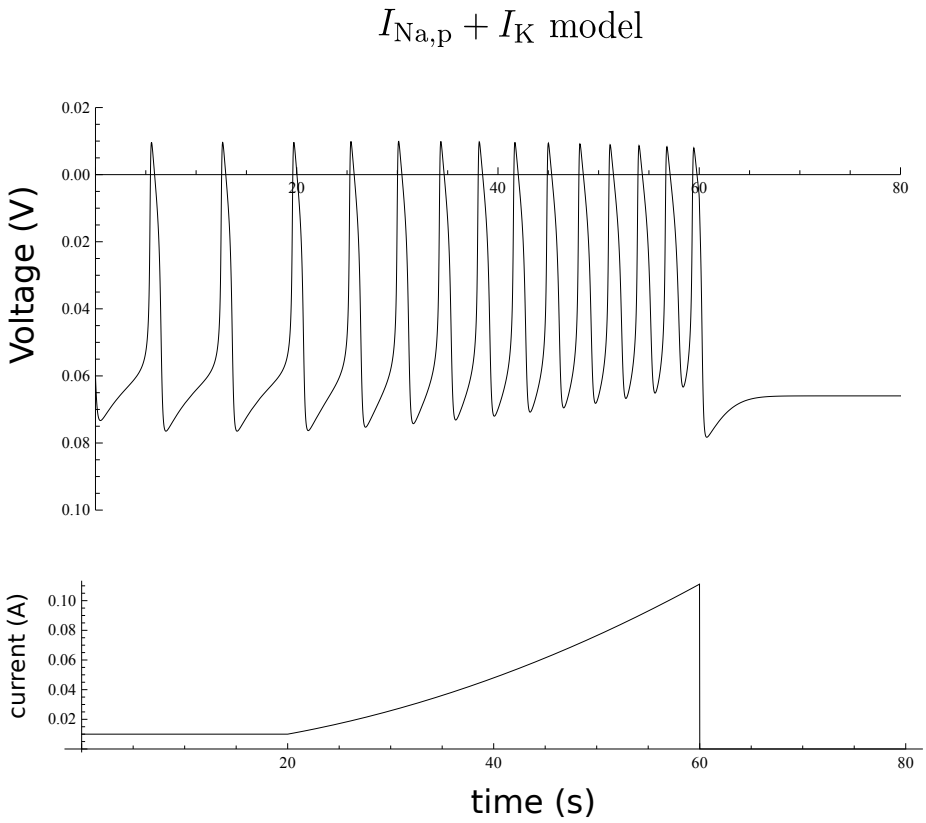

Figure 2.2: Spiking activity for quadratically increasing injected current I_0 for the $I_{\mathrm{Na,p}} + I_{\mathrm{K}}$ model, regulated by equation (2.2) and parameters in table 2.1

input current: a change in the I parameter has the effect of moving vertically the V-nullcline. The narrowing in the space between the two curves around the local minimum V^* causes an increase in the cycle period. When the nullclines intersect in one point, the time for a cycle becomes infinite. Finally a negative I generates two intersections, thus breaking the periodic dynamics. From this behavior whe can state that our system in near a *saddle-node* bifurcation on an invariant cycle, regulated by the fine-tuning of the I parameter.

In figure 2.2 we can see the plot of $V(t)$ for a system near the saddle-node condition with a current slowly increased in time (quadratically). The result is a smooth increase in the frequency of spiking, while the spiking signals themselves don't change in shape or intensity: the invariance of the action potential is preserved.

The equations described here have the same qualitative behavior as the typical type 1 neuron, thus we can say they represent a *canonical model* for this kind of dynamical system.

Quadratic Integrate and Fire Model

We have shown that the most crucial part for the smooth regulation of the spiking frequency lies in the near-bifurcation area. To proceed to further sim-

plifications we thus perform a series expansion of $dV(t)/dt$ around V^*. In this area n lies near its nullcline, too, so we can make the assumption $n \to n_\infty(V)$ and reduce the dynamical system to one dimension (equivalent to say that all ion channels react instantaneously). Then, for the properties stated on V^*, the first derivative is zero. We stop at the second order, obtaining:

$$C\frac{dV(t)}{dt} \approx \frac{g_{\mathrm{Q}}}{\gamma}\,(V(t)-V^*)^2 + I(t)\;. \tag{2.5}$$

Here g is a conductance and γ has the dimension of a voltage. Such values can be inferred from fits on type 1 neurons near saddle-node bifurcation.

If the current is constant in time, i.e. $I(t) \equiv I_0$, we have an analytical solution:

$$V(t) = \sqrt{\frac{\gamma I_0}{g_{\mathrm{Q}}}}\tan\left(\frac{\sqrt{g_{\mathrm{Q}}}}{\sqrt{\gamma}\,C}\sqrt{I_0}t + \alpha\right)\;; \tag{2.6}$$

where the constant α depends on the starting point $V(0)$:

$$\alpha = \arctan\left((V(0)-V^*)\sqrt{\frac{g_{\mathrm{Q}}}{\gamma\, I_0}}\right)\;. \tag{2.7}$$

If we assume that $V(0) < V^*$ and $\sqrt{g_{\mathrm{Q}}}/\sqrt{\gamma\, I_0} \gg 1$, we have $\alpha \approx -\pi/2$. Writing g_{Q} as the inverse of a membran resistance r_{m}, the latter hypotesis becomes $\gamma\, I_0\, r_{\mathrm{m}} \ll 1$, justified by the fact that membranes have resistance of the order of $\mathrm{m}\Omega\ \mathrm{cm}^2$, the currents are usually expressed in $\mu\mathrm{A}/\mathrm{cm}^2$ and the voltages in mV.

The equation (2.6) goes to a $+\infty$ voltage in finite time, reflecting the fact that if we get too far from V^* the series expansion loses its meaning. Thus, to obtain a periodic dynamics, an artificial reset is necessary: if $V(t) > V_{\mathrm{threshold}}$, then $V(t) \leftarrow V_{\mathrm{reset}}$. With the same hypothesys on V_{reset} as the ones mentioned above, we can assume V starts at $-\infty$, peaks at $+\infty$ and then is resetted back at $-\infty$.

The most convenient way to describe this model is though a phase description [32], with a rescaling and changing of variables in the form

$$I_0 \leftarrow I_0\,\frac{\gamma}{g_{\mathrm{Q}}}\;, \qquad t \leftarrow t\,\frac{g_{\mathrm{Q}}}{\gamma\, C}\;, \qquad V = \sqrt{I_0}\tan\frac{\theta}{2}\;, \tag{2.8}$$

equation (2.6), in the $\alpha \approx \pi/2$ limit , is simplified to:

$$\theta(t) = 2\sqrt{I_0}t - \pi;\,. \tag{2.9}$$

With this phase description, the QIF model is often reffered to as *theta model*. With the scaling we used, the range in which the theta neurons evolve their phase is $[-\pi,\, \pi)$. In the literature the interval interval $[0,\, 1)$ is also frequenntly used.

As an example, in figure 2.3, we plotted dV/dt versus V for $I_{\mathrm{Na,p}} + I_{\mathrm{K}}$ model, using the same parameters as above, and we performed a quadratic fit of the points around $V^* \approx -60\mathrm{mV}$ (in red).

The behavior of a QIF neuron under a constant positive current and under a quadratically increasing current is shown in figure 2.4 It clearly follows a type 1 excitation, thus being the simpler canonical spiking model for a type 1 neuron, and, for its analyticity, the most suitable for large scale network simulations [30].

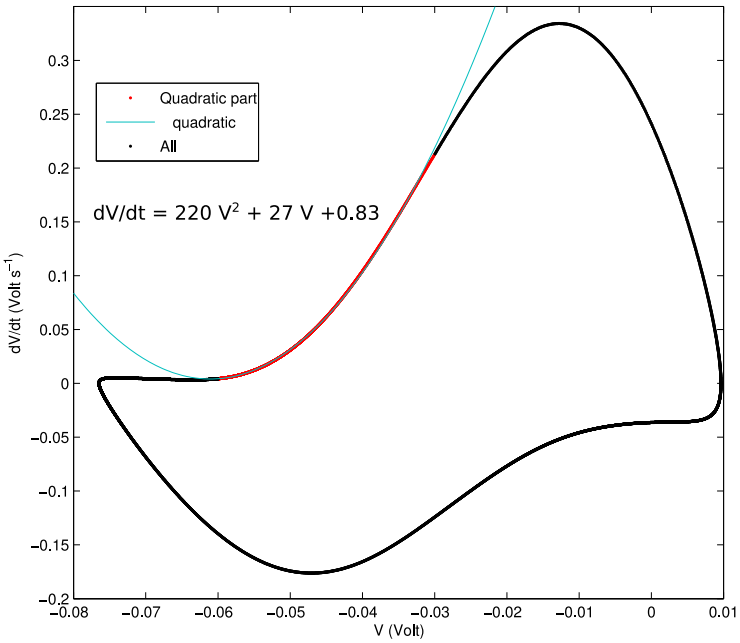

Figure 2.3: dV/dt versus V in the $I_{\mathrm{Na,p}} + I_{\mathrm{K}}$ model. The curve (2.5), corresponding to a second order expansion in the point $V = V^*$, is fitted and plotted.

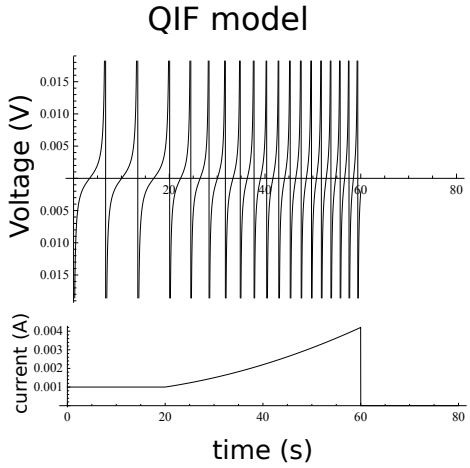

Figure 2.4: An example of spiking activity for a QIF neuron with dynamics regulated by (2.6) and parameters obtained confronting (2.5) with the quadratic fit represented figure 2.3

2.2 Network Dynamics

The system of our concern is a **large, static, sparsely connected pulse-coupled neuronal network**.

We call the N elementary components of our system *neurons*. Each of them has a single degree of freedom: its trans-membrane potential $V(t)$, which varies dynamically depending on the electric current $I(t)$ the neuron is subjected to. The dynamics of neuron i is then given by a differential equation of the form:

$$\frac{dV_i(t)}{dt} = F\left(V_i(t), I_i(t)\right) \ . \tag{2.10}$$

If we use the QIF model, the $F(V, I)$ is given by (2.5), but is important to notice that what stated in this section is valid in general for any one-parameter type 1 neuron model, such as leacky integrate-and-fire neurons and possible variations on the theta model.

A neuron is said to emit a *spike* when its internal variable reaches some particular condition (usually when it reaches a given $V_{\text{threshold}}$ potential). In most models, after the event, the potential decreases again to a V_{reset} value. The times when a spike is *received* by neuron i are indicated as $\{t_1^i, t_2^i, \dots, t_{N_i^{\text{spi}}}^i\}$, N_i^{spi} being the total number of such events.

At this point we need to define the *synaptic connection matrix* $\boldsymbol{J}_{ij}$: it establishes whether the neuron j is connected to i, the nature of its connection (excitatory or inhibitory), and its strength. The *presynaptic* and *postsynaptic neurons sets* are defined so that: $\text{pre}(i) \coloneqq \{\text{neurons } j \mid j \text{ is connected to } i\}$ and $\text{post}(i) \coloneqq \{\text{neurons } j \mid i \text{ is connected to } j\}$.

In our model, when some neuron j^* emits a spike, it injects to all neurons of the $\text{post}(j^*)$ set a current waveform, with intensity proportional to the connection strength and shape given by a stereotypic function $\zeta(t)$, assumed to be the same for all neurons.

Thus we can write the current received by a single neuron as the sum of an external component $I_i^{\text{ext}}(t)$ plus the contribution of the internal dynamics from its presynaptic set, in the form:

$$I_i(t) = I_i^{\text{ext}}(t) + \sum_{j \in \text{pre}(i)} \sum_{p=1}^{N_i^{\text{spi}}} \boldsymbol{J}_{ij}\, \zeta(t - t_j^p) \ . \tag{2.11}$$

We assume that $\zeta(t)$ has the properties:

$$\zeta(t) = 0 \ \text{ for } t < 0 \,, \qquad \zeta(t) \geq 0 \ \text{ for } t \geq 0 \,, \qquad \int_{-\infty}^{+\infty} dt\, \zeta(t) = 1 \,. \tag{2.12}$$

The connections given by $\boldsymbol{J}_{ij}$ are not symmetric, so that the pre and post-synaptic sets of a given neuron are, in general, different, but they are costant in time, making the network *static*. The strengths may vary, depending on the population of the connected neurons - excitatory or inhibitory. Further considerations about the synaptic matrix, its values, and the implications on network dynamics will be done in the next part.

Basically The network evolves continuously in time, free of internal interactions, with every neuron subjected only to external currents, until some j neuron reaches the $V_{\text{threshold}}$ and fires. Then all the neurons in the post(j) set will change their dynamics due to the f-shaped injection of current from j, with sign and strength stated by the $\boldsymbol{J}$ matrix.

We should mention that, to keep the system biologically meaningful, we need the decay of $\zeta(t)$ to be on a timescale much lower than the average interval between two spikes of the same neuron: in the described model the currents injected by a single neuron, if too near in time, would just sum up, in contrast with the well-know invariance of the neuron's action potential and to the presence of a refractory time.

For this reason, and taking into account the properties (2.12), we will later approximate $\zeta(t)$ with a Dirac delta function.

2.3 The Balanced State

As mentioned in the introduction, the physical system we are considering for our network model are the pyramidal neurons of the neocortex.

Between the fifties and the early sixties, electrophisiological and data analysis techologies permitted measures on the potential of single living neuronal cells. In particular it was widely accepted that the spiking activity of pyramidal neurons, in the regime we are interested in, can be seen as a stochastic, stationary point-process [33]. From many *in vivo* observations on the activity of cortical neurons, and measures of the time between two consecutive spikes, the *inter-spike interval* or ISI, performed on different animals, resulted that the spiking events are, with good approximation, nearly independent one another, thus following approximately the Poisson point-process statistics. This results in an exponential distribution of the ISI.

The *balanced state* model [34] has the purpose of explaining and reprodicing this behavior. The fundamental idea of the model is that the net potential of each neuron, due to the signals coming from its presynaptic set, is constantly *balanced* in a near-threshold condition by the intrinsic net dynamics. When the input, due to weak correlations, is not averaged out, it causes the neuron to fire. With this mechanism the sensitivity and the rapidness are much greater then they would be for a neuron laying in its resting potential. The weak correlation guarantees that spikes very near in time come mostly from neurons very scarcely dependent between each other, so that the total spike train has the desired structure of a Poisson point process.

After this model was introducted, numerous experiments confirmed it with in-vivo measures on different animals. Just to cite a few: in-vivo measures on the intact neocortex of ferrets [35], on the rat's sensorimotor cortex (in the area that controls the whiskers) [36], and in the spinal cord of audult turtles[37], proved that the spontaneous balancing between excitation and inhibition is fundamental in regulating the dynamics of the neurons.

To mimic this model, we use for our pulse-coupled network the topological structure of random graph, in which every node has, on average, K connections

to other nodes randomly chosen. The fundamental condition implicit in all our statistical studies is:

$$N \gg K \gg 1. \tag{2.13}$$

Such structure is obtained by defining the synaptic matrix in the form.

$$\boldsymbol{J}_{ij} \coloneqq \begin{cases} \mathrm{J}_{\alpha\beta}, & \text{with probability } K/N \\ 0, & \text{with probability } (1 - K/N) \end{cases} \tag{2.14}$$

The value and sign of $\mathrm{J}_{\alpha\beta}$ depends on which population the neurons i and j belong to. If we consider both excitatory E and inhibitory I neurons we have four possible values: J_{EE}, J_{EI}, J_{IE}, J_{II}. The external current will be assumed constant in time and equal for all members of the same population: $I_i^{\mathrm{ext}}(t) \equiv I_\gamma^{\mathrm{ext}}$, $\gamma = \{E, I\}$.

To preserve the scalability of the system we impose the requirements:

$$\mathrm{J}_{\alpha\beta} \propto \frac{1}{\sqrt{K}} \qquad \text{and} \qquad I_\gamma^{\mathrm{ext}}(t) \propto \sqrt{K}\,. \tag{2.15}$$

This is physically equivalent to rescaling the $V_{\mathrm{threshold}}$ of a $\sqrt{K}$ factor, as to say that, in our weakly correlated model, the minimum number of inputs a neuron requires for a sensitive change in its dynamics is proportional to the square root of the total connections, and not to all of them.

We will now show that, with this choice, the time averaged firing rate of a neuron is K-independent. For time average and population average we use the notations:

$$< \bullet(t) >_t \coloneqq \frac{1}{T}\int dt\, \bullet(t) \qquad \text{and} \qquad [\bullet_i]_i \coloneqq \frac{1}{N}\sum_i^N \bullet_i\,. \tag{2.16}$$

The average firing rate for neuron i is then: $\bar{\nu}_i = 1/\langle \mathrm{ISI}_i \rangle_t$.

For now we restrict ourselves to a system composed only by inhibitory neurons and subjected to a positive external current:

$$\begin{aligned} &I_\gamma^{\mathrm{ext}}(t) = I_I^{\mathrm{ext}} = \sqrt{K} I_e\ ; \\ &\boldsymbol{J}_{ij} = \boldsymbol{J}_{II} = -\frac{J_0}{\sqrt{K}} \text{ when different from 0}\ . \end{aligned} \tag{2.17}$$

We start calculating the current as given by equation (2.11), averaged over time and neuron ensemble. The external term, being constant, is not changed. Looking at the conditions (2.12), we can say that for long times the second term will depend on the total connections, their strength and how often, on average, the pulse is received. This leads to the result:

$$[\langle I_i(t) \rangle_t]_i \approx I_I^{\mathrm{ext}} - K\frac{J_0}{\sqrt{K}}\bar{\nu} = \sqrt{K}(I_e - J_0\bar{\nu})\ . \tag{2.18}$$

A more rigorous calculation is performed in appendix A.

We now take into consideration the term $(I_e - J_0\bar{\nu})$ in the $K \to \infty$ limit, with the assumption that $N \gg K$ is still valid, so that the statistical structure is preserved.

If $(I_e - J_0\bar{\nu}) < 0$, the average current given by (2.18) will go to $-\infty$ for increasing K. But a high negative current means high negative polarization: the neurons would stop firing and $\bar{\nu} \to 0$. Since both I_e and J_0 are positive constants, this would lead to $(I_e - J_0\bar{\nu}) > 0$, contrary to the starting hypothesis.

If we start with $(I_e - J_0\bar{\nu}) > 0$, for the same considerations as above, the neurons would be injected with a strong positive current, firing with higher and higher frequency. For very large $\bar{\nu}$ we then have, $(I_e - J_0\bar{\nu}) < 0$, contradicting the hypothesys

Therefore the limit must be 0, leading to the result:

$$\bar{\nu} = \frac{I_e}{J_0} \quad \text{for K} \to \infty; \tag{2.19}$$

while, to keep the average current finite, $(I_e - J_0\bar{\nu}) = \mathcal{O}(1/\sqrt{K})$ in the large K limit.

In a case of different populations, the mean current (2.18) would include the average of the different strengths, weighted on the respective populations, instead of $-J_0$. If such value is negative, the proof doesn't change; if positive, we would have a positive external current with overall positive interactions, which would lead to the loss of large-K scalability and to an unnatural network dynamics.

The result is that, with the rescaling of currents and connection strengths given by (2.17), and the requirement of an average negative net current contribution from the network, we can build a neural network with scale-free statistical properties, which we can study in the limits $N \to \infty$, $K \to \infty$, $N \gg K$.

2.4 Model Architecture

To to simplify our problem we use a *phase description* of the neurons, choosing a phase map of the form

$$U : [V_{\text{reset}}, V_{\text{threshold}}] \to [\theta_{\min}, \theta_{\max}] \ , \quad \text{smooth and monotonically increasing.}$$

The phase of neuron i at time t is then:

$$\theta_i(t) \ = \ U(V_i(t)) \ .$$

The interval $[\theta_{\min}, \theta_{\max}]$ can be arbitrarly chosen. In our particular choice for the QIF model will be $[+\pi, -\pi]$.

We now define a function for the complete time evolution followed by the phase of a neuron which gets no signals from the network: the *unperturbed time evolution function*.

$$\psi \ : \ [0, \ t_{\max}] \to [\theta_{\min}, \theta_{\max}]; \tag{2.20}$$

it is assumed to be monotonic, smooth and invertible, as well, and is derived from the dynamics of the specific neuron model, taking the time evolution of a neuron which starts at V_{reset} and doesn't interact with the network until it reaches its threshold. If we reduce to 0 the internal interactions, we impose that $V(0) = V_{\text{reset}}$ and we define $t_{\max}$ so that $V(t_{\max}) = V_{\text{threshold}}$, then:

$$\psi(t) \coloneqq U(V(t)) \ , \quad t \in [0, \ t_{\max}] \tag{2.21}$$

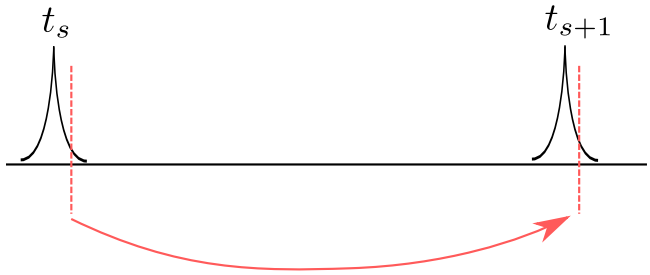

Figure 2.5: Times considered for the mapping

If we have a phase at a specific time $\theta_i(t_0 + \Delta t)$ the value it has after the time interval Δt, on the condition it gets no perturbations, is then:

$$\theta_i(t_0 + \Delta t) = f(\theta_i(t_0), \Delta t) \coloneqq \psi\left(\psi^{-1}(\theta_i(t_0)) + \Delta t\right) \ . \tag{2.22}$$

For the reasons stated on page 38, we assume that the current injection function $\zeta(t)$ can be reasonably approximated by a Dirac delta function. The network currents, given by the second therm of (2.11) are then pulses, which cause step-like changes in the potential proportional to the connection strengths $\boldsymbol{J}_{ij}$, given by (2.14).

The function which gives the resulting phase a moment after such injection is called *phase transition curve* and has the form:

$$\theta_i(t_s^+) \ = \ g(\theta_i(t_s^-)) \ ;$$

where t_s^- and t_s^+ are the times right before and right after the reception of the spike by i neuron. We can express the phase transition curve in terms of the phase map as:

$$g(\theta_i(t_s^-)) \ = \ U\left(U^{-1}\left(\theta_i(t_s^-)\right) + \boldsymbol{J}_{ij}\right) ; \tag{2.23}$$

where the presynaptic spiking neuron has index j.

Finally we need to know how long it is until a neuron of given phase $\theta_i(t)$ reaches the threshold value $+\pi$ in the unperturbed evolution. The *spiking time function* is defined as:

$$\Delta t_{\text{spi}} \ = \ h(\theta_i(t)) \ , \qquad \text{so that:} \qquad \theta(t + \Delta t_{\text{spi}}) = \theta_{\max} \ . \tag{2.24}$$

It can be derived in terms of $\psi(t)$ starting from (2.22):

$$\begin{aligned} f(\theta_i(t_0), \Delta t_{\text{spi}}) = \psi\left(\psi^{-1}(\theta_i(t)) + \Delta t_{\text{spi}}\right) = \theta_{\max}; \\ \psi^{-1}(\theta_i(t)) + \Delta t_{\text{spi}} = \psi^{-1}(\theta_{\max}) \ ; \\ h(\theta_i(t)) \coloneqq \psi^{-1}(\theta_{\max}) - \psi^{-1}(\theta_i(t_0)) \ . \end{aligned} \tag{2.25}$$

The convention that we use to index the neurons in a given time interval Δt is the following:

$$\begin{aligned} &\{i\} = \{\text{neurons}\} \ ; && j^* = \text{the neuron which spikes in } \Delta t \ ; \\ &i = i^* \Rightarrow j^* \in \text{pre}\,(i) \ ; && i \neq i^* \Rightarrow j^* \notin \text{pre}\,(i) \ . \end{aligned}$$

Namely the $i = i^*$ neurons receive the signal form the spiking j^* neuron, while the $i \neq i^*$ neurons are unperturbed. Using our formalism we can finally write the phase map, defined as the function which maps the phase of a given neuron from the moment immediately after a spike t_s to the time immediately after the next spiking event (by neuron j^*) t_{s+1}, as represented in figure 2.5 .

$$\theta_i(t_{s+1}) = \begin{cases} \theta_{\min} , & \text{if} \quad i = j^* ; \\ f(\theta_i(t_s), t_{s+1} - t_s) = f\big(\theta_i(t_s), h(\theta_{j^*}(t_s))\big) , & \text{if} \quad i \neq i^* ; \\ g\Big(f\big(\theta_i(t_s), h(\theta_{j^*}(t_s))\big)\Big) , & \text{if} \quad i = i^* . \end{cases} \tag{2.26}$$

The equations can be written explicitly in terms of the phase map and the unperturbed time evolution functions. The $j^* \in \mathrm{pre}(i)$ case, for example, becomes:

$$\theta_{i^*}(t_{s+1}) = U\Big(U^{-1}\Big(\psi\big(\psi^{-1}(\theta_{i^*}(t_s)) + \psi^{-1}(\theta_{\max}) - \psi^{-1}(\theta_{j^*}(t_s))\big)\Big) + \boldsymbol{J}_{i^*j^*}\Big) . \tag{2.27}$$

Computationally, starting from timestep t_s, we select the neuron closest to spiking, i.e. the one with the highest phase, and we compute each phase to the moment after the new spike, using equations (2.26). Then we select the highest phase and we iterate the process. In such a model the time dependency is implicit: the interspike intervals are not fixed steps, but vary according to the spiking times of single neurons, calculated with machine precision. This qualifies our network simulation as *event based*.

2.5 Equations for a QIF Network

Now we restrict ourself on a QIF model, expressing explicitly and analytically all the equations defined above. the result is the backbone of all the computational large scale simulations performed in our work.

In the QIF model the dynamics is given by equation (2.5), with the approximated value for α. The current is assumed to have the form of equation (2.11), with external currents constant in time and delta-shaped network pulses. For sake of simplicity we assume $V^* = 0$, and we rescale the I_0 and t variables as in (2.8) In absence of pulses, the solution is:

$$V_i(t) = \sqrt{I_i^{\mathrm{ext}}} \tan\left(\sqrt{I_i^{\mathrm{ext}}}\, t - \frac{\pi}{2}\right) . \tag{2.28}$$

The phase description we are using, as alredy mentioned in section 2.1 is:

$$U^{\mathrm{QIF}}(V_i(t)) = \theta_i(t) = 2 \arctan \frac{V_i(t)}{\sqrt{I_i^{\mathrm{ext}}}} . \tag{2.29}$$

It has $\theta_{\min} = -\pi$ and $\theta_{\max} = \pi$. The unperturbed time evolution function, as described by (2.21), is then:

$$\psi^{\mathrm{QIF}}(t) = 2\sqrt{I_i^{\mathrm{ext}}}\, t - \pi . \tag{2.30}$$

The evolution of a neuron with a phase description can now be derived from (2.22):

$$f^{QIF}(\theta_i(t_0), \Delta t) = \theta(t_0) + 2\sqrt{I_i^{\mathrm{ext}}}\, \Delta t . \tag{2.31}$$

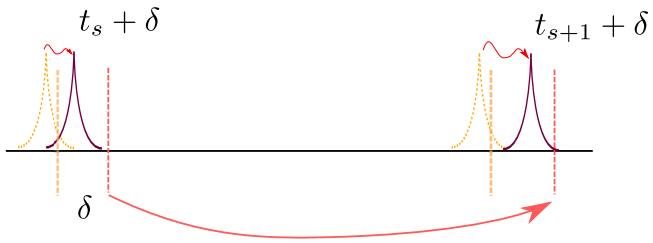

Figure 2.6: Times considered for the mapping in the calulation of the Jacobian

The spiking time function comes from (2.25):

$$h^{\mathrm{QIF}}(\theta_i(t)) = \frac{\pi - \theta_i(t)}{2\sqrt{I_i^{\mathrm{ext}}}} \tag{2.32}$$

Finally, the phase transition curve is inferred from (2.29) and (2.23).

$$g^{\mathrm{QIF}}(\theta_i(t_s^-)) = 2 \arctan\left(\tan\left(\frac{\theta_i(t_s^-)}{2}\right) + \frac{\boldsymbol{J}_{ij^*}}{\sqrt{I_i^{\mathrm{ext}}}}\right) . \tag{2.33}$$

2.6 Calculating the Jacobian

If the system is composed by N neurons, we can describe the phases at a given time defining the N dimensional vector

$$\boldsymbol{\theta}(t) = (\theta_1(t),\ \theta_2(t),\ \ldots, \theta_N(t))$$

The phase map is such as $\boldsymbol{\mathcal{F}}(\boldsymbol{\theta}(t_s)) = \boldsymbol{\theta}(t_{s+1})$. The Jacobian matrix $\boldsymbol{D}(t)$ represents the linearized version of $\mathcal{F}$, and gives the first order correction in case of small phase perturbation:

$$\boldsymbol{\mathcal{F}}(\boldsymbol{\theta}(t) + \epsilon\, \boldsymbol{\delta\theta}) \approx \mathcal{F}(\boldsymbol{\theta}(t)) + \epsilon\, \boldsymbol{D}(t)\, \boldsymbol{\delta\theta} .$$

It is important to notice that a perturbation in phases will result in a shift in spike times, therefore we need to define a slightly different phase map to take this shift into account. Our strategy consists in shifting the times considered for the mapping of an interval δ, assumed to be bigger than the shift in spiking times caused by the perturbation. As the perturbation tends to 0 we will eventually go in the $\delta \to 0$ limit. The interval we are considering is shown in figure 2.6, the steps will be:

- start with phases at time $t_s + \delta$;
- calculate new phases at next (perturbed) spiking time;
- evolve the system furtherly, till time $t_{s+1} + \delta$.

In this case the time t_s, t_{s+1} are considered as independent from phases. They will turn into the actual spiking times in the small perturbation limit.

The phase map is thus a little more structured than (2.26), with the form:

$$\theta_i(t_{s+1}+\delta)=\begin{cases} f\big(\theta_{\min}, t_{s+1}-t_s-h(\theta_{j^*}(t_s+\delta)\big)\,, & \text{if} \quad i=j^*\,; \\ f(\theta_i(t_s+\delta), t_{s+1}-t_s)\,, & \text{if} \quad i\neq i^*\,; \\ f\Big(g\Big(f\big(\theta_i(t_s+\delta), h(\theta_{j^*}(t_s+\delta))\big)\Big), t_{s+1}-t_s-h(\theta_{j^*}(t_s+\delta))\Big), & \\ & \text{if} \quad i=i^*\,. \end{cases} \tag{2.34}$$

Using this perturbed map, we can define the Jacobian matrix elements as:

$$\boldsymbol{D}_{ij}(t_s)=\lim_{\delta\to 0}\frac{\partial\theta_i(t_{s+1}+\delta)}{\partial\theta_j(t_s+\delta)} \tag{2.35}$$

Looking at the map dependencies, we can infer that the nonzero elements are the diagonal ones, i.e. $j=i$, and the derivations with respect to the phase of a presynaptic spiking neuron, espressed by the conditions: $j=j^*$ AND $i=i^*$.

As an example, we show the explicit calculation of a diagonal element such that $i=i^*$ .For simplicity of notation the $\delta\to 0$ limit is omitted and $\theta_{i^*}:=\theta_{i^*}(t_s+\delta)$, $\theta_{j^*}:=\theta_{j^*}(t_s+\delta)$.

$$\frac{\partial}{\partial\theta_{i^*}} f\big(g\big(f(\theta_{i^*},h(\theta_{j^*}))\big), t_{s+1}-t_s-h(\theta_{j^*})\big) =$$
$$\partial_\theta f(\theta, t_{s+1}-t_s-h(\theta_{j^*}))\Big|_{\theta=g(f(\theta_{i^*},h(\theta_{j^*})))}\partial_\theta g(\theta)\Big|_{\theta=f(\theta_{i^*},h(\theta_{j^*}))}\partial_\theta f(\theta,h(\theta_{j^*}))\Big|_{\theta=\theta_{i^*}}$$

The f, h, g functions can be derived from the phase map and the unperturbed time evolution function, according to, respectively, (2.22), (2.25),(2.23). Since we are in a QIF model we can write them explicitly, using the (2.31), (2.32), (2.33), and find an analytical solution.

We have $\partial_\theta f^{\mathrm{QIF}}(\theta,\Delta t)=1$, the only contribution comes then from the $\partial_\theta g^{\mathrm{QIF}}(\theta)$ derivative, calculated in point $\theta=f^{\mathrm{QIF}}(\theta_{i^*},h(\theta_{j^*}))=\pi+\theta_{i^*}-\theta_{j^*}$:

$$\partial_\theta g^{\mathrm{QIF}}(\theta)\Big|_{\theta=\pi+\theta_{i^*}-\theta_{j^*}} = 2\,\frac{1+\tan^2\frac{\pi+\theta_{i^*}-\theta_{j^*}}{2}}{1+(\tan\frac{\pi+\theta_{i^*}-\theta_{j^*}}{2}+\frac{\boldsymbol{J}_{i^*j^*}}{\sqrt{I^{\mathrm{ext}}_{i^*}}})^2}\,.$$

From (2.17) we have $\boldsymbol{J}_{i^*j^*}/\sqrt{I^{\mathrm{ext}}_{i^*}}\propto K^{-3/4}$. For large K we can therefore write a first order approximation, with the result:

$$\begin{aligned}\boldsymbol{D}_{i^*i^*}(t_s) &= 2\left(1+\frac{\boldsymbol{J}_{i^*j^*}}{\sqrt{I^{\mathrm{ext}}_{i^*}}}\sin\big(\pi+\theta_{i^*}(t_s)-\theta_{j^*}(t_s)\big)\right)= \\ &= 2\left(1+\frac{\boldsymbol{J}_{i^*j^*}}{\sqrt{I^{\mathrm{ext}}_{i^*}}}\sin\big(\theta_{i^*}(t_s)\big)\right)+\mathcal{O}\Big(\big(\pi-\theta_{j^*}(t_s)\big)\cos\big(\theta_{i^*}(t_s)\big)\Big)\,.\end{aligned} \tag{2.36}$$

The last passage is justified by the fact that we expect $\theta_{j^*}(t_s)$ to be close to π, being the phase of the neuron closest to spiking.

For $i\neq i^*$ the resulting diagonal element is simply:

$$\boldsymbol{D}_{ii}(t_s)=\partial_\theta f^{\mathrm{QIF}}(\theta,t_{s+1}-t_s)\Big|_{\theta=\theta_i}=1; \tag{2.37}$$

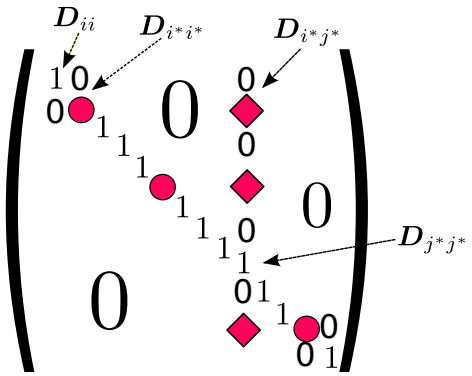

Figure 2.7: Jacobian matrix

In the $i = j^*$ case we obtain:

$$\boldsymbol{D}_{j^*j^*}(t_s) = \partial_{\Delta t} f(\theta_{\min}, \Delta t)\Big|_{\Delta t = t_{s+1} - t_s - h(\theta_{j^*})} (-1)\ \ \partial_\theta h(\theta)\Big|_{\theta=\theta_{j^*}} = 1\,. \quad (2.38)$$

Finally, when deriving a postsynaptic neuron by $\theta_{j^*}(t_s)$ phase, we get the out-of-diagonal elements:

$$\boldsymbol{D}_{i^*j^*} = \sqrt{\frac{I^{\text{ext}}_{i^*}}{I^{\text{ext}}_{j^*}}}\,(1 + \boldsymbol{D}_{i^*i^*}(t_s))\,. \quad (2.39)$$

The Jacobian matrix has therefore a nonzero diagonal with $\boldsymbol{D}_{i^*i^*}$ elements corresponding to the postsynaptic neurons, a series of ones in the remaining $(i,\ i)$ and $(j^*,\ j^*)$ locations, finally, out of diagonal, confined in the j^*th colum, we have a $\boldsymbol{D}_{ij^*}$ nonzero element for each $i \in \text{post}(j)$. A scheme of such structure is shown in figure 2.7.

While in a general Jacobian N^2 elements should be computed, in our system the nontrivial values are of the order of K, which, together with the simple model we used, makes the simulation of large scale networks possible.

Chapter 3

Computation and Results

In this chapter the simulation procedure is described in detail, and the achieved results are reported and analyzed.

The first part summarizes the structure of the simulating program in use, describes the input parameters and the elaboration performed on the output. Afterwards we analyze the *forward evolution* of the neural network, i.e. the succession of spikes and phases of every single neuron in time. We probe to which extent the statistic resembles a Poisson point process, and we try to quantify the synchronicity of our model. After that, from the Lyapunov spectrum, we estimate the entropy and attractor dimension.

In the next section the system is evolved backwards and the Lyapunov vectors are calculated. A check on the convergence of the vectors is performed; after some considerations on the evolution and the general appearance of the vectors, we examine the angles between them, drawing some conclusions on the hyperbolicity of the dynamical system.

The vectors are subsequently used to characterize the participation of single neurons to the global dynamics of the system. This is accomplished by confronting the average participation ratios of vectors and the chaos index components with the spiking frequencies associated to single neurons.

The last section takes into consideration possible optimizations to the simulation and further analyses on the system.

3.1 Network Computation

The neural network simulation program, written in C++, is the slight adaptation of the code used by M. Monteforte for his works [8, 9]. The inputs and their ranges are described in table 3.1

The connection strengths J_0 are all fixed on 1, while the external current I_e is approximately calculated from (2.19) and then fine tuned with several iterations, until the average neuron frequency is close enough to the input parameter f. The parameter s_{sk} can be identified with the k introduced at page 22: it is the number of single steps we group together in a single GS (and vector) iteration. The time length of the simulation is given by:

$$T = \frac{S\, s_{\mathrm{sk}}}{f\, N} \ . \tag{3.1}$$

Table 3.1: Arguments for the simulating program.

Parameter	Description	range
N	Number of neurons	$200 - 1000$
K	Average connections per neuron	$20 - 100$
S	Timesteps to compute	$3000 - 10000$
f	Average neuron frequency	1 Hz
S_{Al}	Timesteps for the alignment of the vectors	$8000 - 15000$
s_{sk}	Iteration of system and GS basis with no QR decomposition	$1 - 5$
nI	Total iterations with different network initializations	$1 - 300$

The functioning of the simulation can be divided into three modules: one for the network evolution, the second for the computation of the Lyapunov spectrum, and the third devoted to the vectors. Their schematic description can be found in the appendix figures B.1 and B.2.

The first module initializes and iterates the network. A connection matrix with a random graph structure is created, then a random phase between $-\pi$ and π is assigned to each neuron. The neuron closest to spiking is the one with the highest phase. Its spiking time is calculated using (2.32), then the phases of the postsynaptic neurons (given by the connection matrix) are updated to the after-signal state, according to (2.33). Finally all phases are computed to next spiking time with equation (2.31), and the process is iterated.

The second module has the purpose of calculating the Lyapunov spectrum and store the information necessary for computing the Lyapunov vectors. The procedure, already explained in sections 1.4 and 1.5, is shortly and operatively summarized here.

We initialize the Gram-Schmidt basis with a set of N, N-dimensional random orthonormal vectors, grouped in a matrix: $Q_{s-1} = (\boldsymbol{q}_{s-1}^{(1)}|\ldots|\boldsymbol{q}_{s-1}^{(m)})$. The Jacobian D_{s-1} at the current state of the network is calculated according to (2.36 - 2.39), and the *push-forward* of the GS vectors is obtained via the multiplication $D_{s-1} \cdot Q_{s-1} = \tilde{Q}_{s_1}$ at this point the neurons and the Jacobian are updated, and this is repeated s_{sk} times, as in (1.12). Then the resulting matrix undergoes a QR decomposition, according to equations (1.13): $\tilde{Q}_s = Q_s \cdot R_s$. Both matrices are stored for the calculation of vectors, and the iteration can enter in the s_{sk} cycle again.

At the end of the evolution, the Lyapunov exponents can be computed using the stored data. From $\{R_s\}_{jj} = ||\boldsymbol{u}_s^{(j)}||$ and equations (1.9) and (1.10), we have:

$$\lambda^{(j)} = \frac{1}{[\Delta t]_s}\frac{1}{S}\sum_{s=1}^{S}\log\{R_s\}_{jj} = \frac{1}{T}\sum_{s=1}^{S}\log\{R_s\}_{jj}\ ; \tag{3.2}$$

The last module computes the time evolution of all Lyapunov vectors. It must be necessarily called after the end of module 2, so that its initial time, $s+1$,

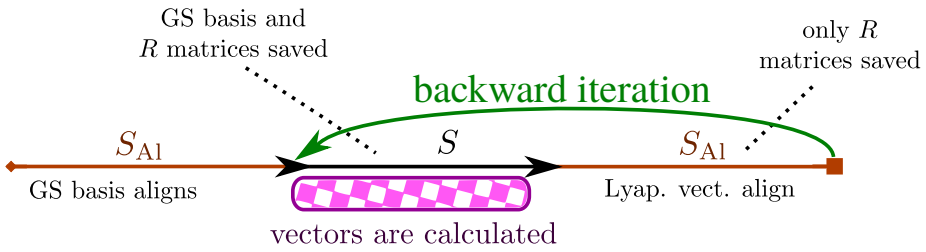

Figure 3.1: Calculation of Lyapunov vectors

corresponds to the final step reached by the system, and it proceeds backwards. Firstly, the matrix of vector coefficients in the GS basis, C_{s+1}, is initialized as a triangular random array with normalized columns. The previously stored R_{s+1} matrix is inverted, and the next C_s is calculated as the normalized form of $\tilde{C}_s = R_{s+1}^{-1} C_{s+1}$. The norms are stored as *local Lyapunov exponents*: processed with an equation equivalent to (3.2), they give a backward version of *global Lyapunov exponents*. Finally the vectors are calculated for every timestep using the GS basis saved at the corresponding instant:

$$\boldsymbol{v}_s^{(j)} = \sum_{i=1}^{j} \{C_s\}_{ij} \, \boldsymbol{q}_s^{(i)} \; . \tag{3.3}$$

The parameter S_{Al} adds a $2\,S_{\mathrm{Al}}$ factor to the number of iterations performed by the second module: for the initial S_{Al} steps the GS vectors are evolved but not saved, while for the final S_{Al} the C matrices are iterated but no Lyapunov vectors are calculated. This process is represented in figure 3.1.

Finally some considerations on memory usage should be done: of the total random-access memory allocated by the program, the largest amount is used to store the triangular R matrix and the GS basis for every timestep. The saving of the R matrix is required also for the final S_{Al} steps. The free memory needed thus amounts (in bytes) to:

$$\mathrm{free\_mem} = \left(\frac{N(N-1)}{2} (S + S_{\mathrm{Al}}) + N^2 S \right) \cdot 8 = \frac{3\,N^2 S + N(N-1) S_{\mathrm{Al}}}{2} \cdot 8 \; . \tag{3.4}$$

Combining the latter equation with (3.1), we infer that if we want to keep the time length constant, the memory usage grows as $\mathrm{M} \propto N^3$. For N above 500, this rapidly causes a RAM shortage. In the final section of the chapter future possible optimizations to overcome this difficulty are considered.

3.2 Output Data

Depending on the data we are interested in, different versions of the simulation are run. The simplest one is composed only by module 1 and 2, and is used only to obtain the forward evolution of the system and the Lyapunov spectrum. After a warm-up of S_{Al} steps, for every further step, the time t_s, the index of the spiking neuron j^*, and the phases of all neurons $\{\theta_i(t_s)\}$ are saved on a binary

Table 3.2: Possible outputs of the program. s is the time index, j the order of the vector and i indexes the neurons.

Name	Value	Description
t_s	t_s	spiketimes
$\lambda^{(j)}(t_s)$	norms of C_s columns	local backward Lyap. exponents
$\langle \cos \alpha_{ij}(t) \rangle_t$	$\left\langle \boldsymbol{v}^{(i)}(t) \cdot \boldsymbol{v}^{(j)}(t) \right\rangle_t$	time-averaged angles between vectors
$\alpha_{\min}(t_s)$	$\min_{ij}\{\alpha_{ij}(t_s) \vert \lambda^{(i)} > 0 \wedge \lambda^{(j)} < 0\}$	min. angle between exp. and contracting directions
$\mathrm{PR}^{(j)}(t_s)$	$\left(\sqrt{\sum_{i=1}^{N} (\boldsymbol{v}_i^{(j)}(t_s))^4} \right)^{-1}$	Participation Ratio
$c_i^{(j)}$	$\frac{1}{S} \sum_{s=1}^{S} (\boldsymbol{v}_i^{(j)}(t_s))^2$	chaos index (avg. of square components)

file. The logarithms of the R_s matrix are cumulatively added in a N-length array which, divided by the last t_S, gives the Lyapunov spectrum. Not having the necessity of storing the time series of big matrices, the simulation requires much less RAM, and runs relatively faster. In this way performing many iterations ($nI = 100 - 200$) for longer times and larger networks is possible.

To check the presence of errors and to perform the convergence tests described in the next section, we use another version of the program, which saves and stores the complete time evolution of each Lyapunov vector, derived from equation (3.2); this requires the full amount of memory calculated in (3.4). The output consists in the $N \times N \times S$ double precision array containing all vectors for every timestep. Due to the big size of the output, the value of repetitions nI is limited to 1.

The last version of the program calculates the vectors, using the full amount of estimated memory, but, rather than saving the vector themselves, processes them in different ways, thus requiring less space on the hard drive and making multiple iterations ($30 - 50$) feasible. The output parameter list is in table 3.2. All values in the left column are sampled for each of their indexes.

3.3 Spike Train

We start our analysis observing the time sequence of the pulses emitted by the neurons, i.e. the spike train of the network. Figure 3.2 depicts the spikes for the first 50 neurons of a $N = 200$, $K = 50$ system. We know that the average frequency of the system is approximately 1 Hz per neuron, however it is clear that individual neurons may fire at very different rates. Figure 3.3 shows the phase of two neurons taken from the same set. In accordance to what we expect,

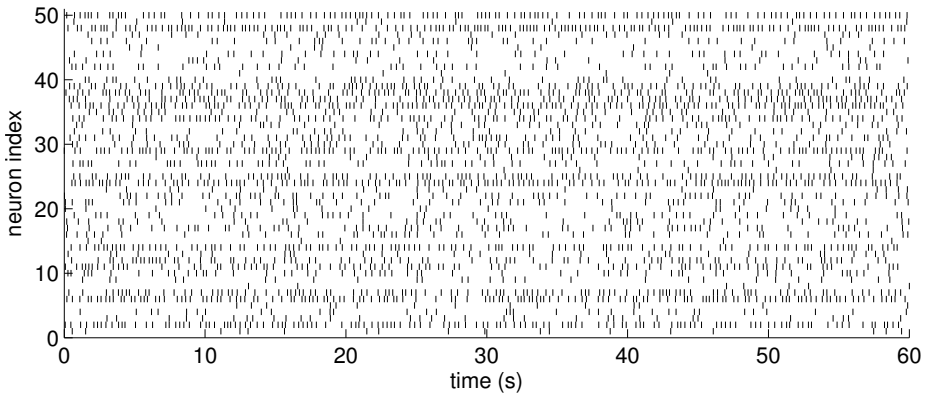

Figure 3.2: Sequence of spikes for the first 50 neurons of a $N = 200$, $K = 20$ network.

the phase evolves with a constant linear velocity given by the positive external current, as in (2.9), it receives inhibitory pulses of varying intensity from the presynaptic neurons, finally when π is reached, a signal is emitted, and the phase is instantly reset to $-\pi$. An example of frequency distribution for a $N = 500$, $K = 20$ is represented in figure 3.5 (b) .

The first quantity we examine is the *coefficient of variation* (C_v) of the inter-spike intervals, it is defined, in general, as

$$C_v = \frac{\sigma}{|\mu|} \; ; \tag{3.5}$$

where μ is the average of our data-set and σ its standard deviation. For a perfectly Poissonian network we would have $C_v = 1$ [27].

The values we have found for system of different sizes and different number of connections are plotted in figure 3.4 (a). They are computed averaging over 380 repetitions for $N = 200$ networks, 300 repetitions for $N = 300$ networks, 100 repetitions for $N = 400$ and $N = 500$, 70 for $N = 700$ and 20 for $N = 1000$. It is clear that larger and more sparsely connected networks tend asymptotically to the ideal value of 1.

Instead of considering the spike train of the network as a whole, we may wonder whether the activity of a single neuron in the network follows nearly Poissonian statistics or not. In figure 3.4 (b) we have represented the distribution of the variation coefficients of single neurons, taken from several repetitions ($nI = 100$) on a $N = 500$, $K = 20$ network. The distribution tends toward one, with a mean of $[C_{v\,i}]_i = 0.73$. This value is far from the one obtained from the network as a whole, namely $C_v = 0.94$

As a further proof of the fact that the process is nearly Poissonian, we show in figure 3.5 (a) the distribution corresponding to $P\{\text{ISI} < t\}$ for a $N = 500$, $K = 20$ network (ISI is the inter-spike interval, i.e. the time between two pulses in the network). It is fitted with the curve (in red): $y = 0.9979(5) + 0.9819(5)\exp(-501(1)\ x)$. For a purely Poissonian process: $P\{\text{ISI} < t\} = 1 - \exp(-\nu\, t)$. The frequency found with this fit is in very good agreement to what we would expect in a network of 500 neurons with an average firing rate of 1 Hz.

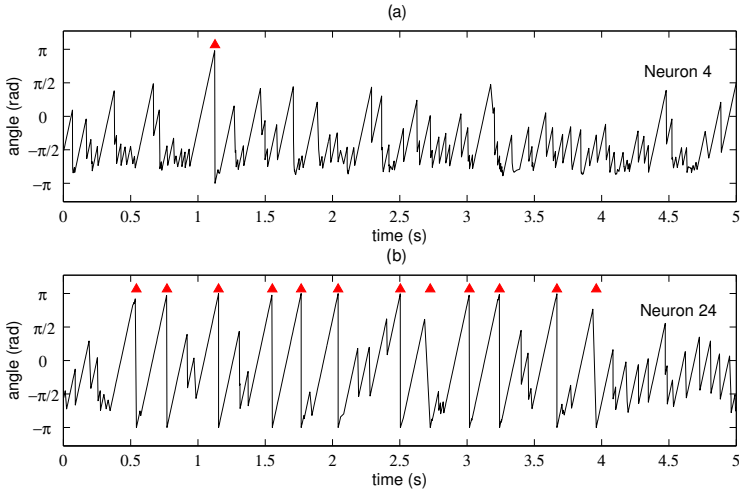

Figure 3.3: Time evolution of the phase of neuron 4, with average spiking frequency $\simeq 0.5$ Hz (a) and neuron 24, with frequency $\simeq 2.4$ Hz (b) selected from the set showed in figure 3.2. Red triangles are drawn when spikes occur (and the value is reset to pi). Neurons evolve linearly as in (2.9), are instantly inhibited by other neurons, and are reset to $-\pi$ after spiking.

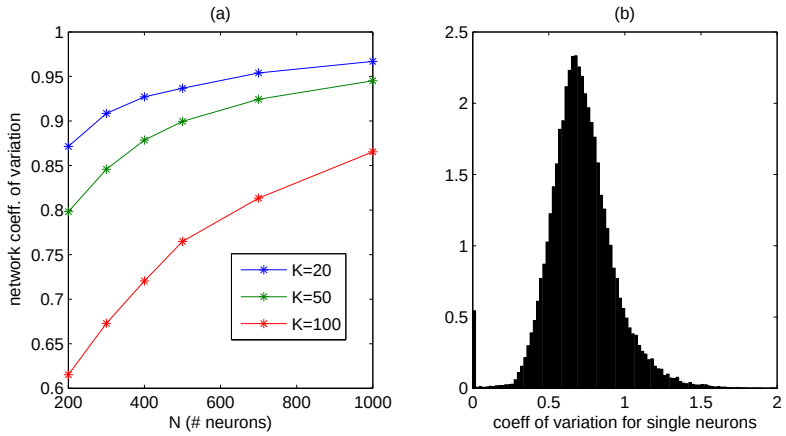

Figure 3.4: (a): coefficient of variation (3.5) for network of different sizes N and different number of average connections per neuron K (color). (b): distribution of $C_{v\,i}$ for single neurons in a $N = 700$ $K = 20$ network, calculated on $nI = 70$ repetitions

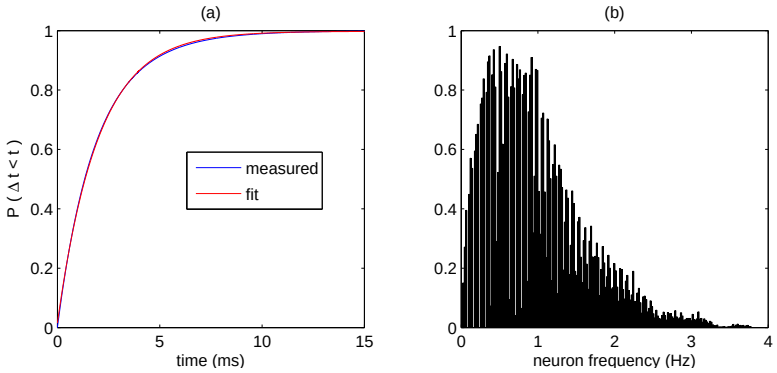

Figure 3.5: (a): the probability $P\{ISI < t\}$ follows very close the curve expected for a Poissonian process: $1 + \exp(-\nu t)$ with a frequency corresponding to the overall frequency of the system. (b): distribution of firing frequencies for single neurons in the same system.

Finally figure 3.5 (b) depicts the distribution of the frequencies for single neurons with the same network parameters as before. Although they average to 1 Hz, their distribution shows a certain spreading, almost touching the frequency we expect for a neuron with no inhibitory synapses, corresponding to ~ 4.6Hz in the network considered.The broad inhomogeneity is another distinctive characteristic of the balanced state [34].

To sum up, our model, although completely deterministic in its evolution, follows closely the statistic of a Poisson point process. The discrepancy appears to decrease as we approach our ideal limit of $N \gg K \gg 1$: many neurons, but very weakly correlated. As already mentioned in the introduction, typical numbers for 1 mm^3 of neocortical tissue are $N \sim 10^6$ and $K \sim 10^4$; therefore it is reasonable to assume that if our system reached those parameters, its global statistics would be practically indistinguishable from an ideal Poissonian process. On the other hand, when we look at single neurons, we see that their spiking is not, in general, a renewal process: a clear sign, along with the nontrivial distribution of frequencies, of the underlying complexity of connections and dynamical interplay between neurons.

3.4 Collective Dynamics

Another interesting investigation on the network is represented by the collective dynamics of its neurons. As said before, neurons in balanced state should ideally be completely asynchronous. From a simple observation of the spike train, in figure 3.2, we would say the requirement is fulfilled. However, we saw in previous section that singular neurons are not Poissonian in general, while the distribution of their frequencies is far from smooth. Therefore is not possible to exclude the presence of some small degree of synchronization. Several methods and measures have been developed to quantify this value.

Following the example of other papers on pulse-coupled network synchronizations [38], we can use the order parameter, first introduced by Y. Kuramoto, in

the form:

$$r(t) \coloneqq \left| \left[\exp(i\theta_j(t)) \right]_j \right| . \tag{3.6}$$

It can be shown [39] that $N \to \infty$ independent oscillators would bring $r(t) \equiv 0$, while synchronized oscillators result in $r(t) \equiv 1$. Intermediate values $0 < r(t) < 1$ represent a *partial synchronization*: some oscillators have a similar phase, while some others are independent.

Another way to assess the synchronicity of a system is the *measure of neuron coherence* [40].

$$\chi^2 \coloneqq \frac{\mathrm{VAR}\left([\theta_i(t)]_i\right)}{\left[\mathrm{VAR}_i\left(\theta_i(t)\right)\right]_i} = \frac{\left\langle \left([\theta_i(t)]_i - \langle [\theta_i(t)]_i \rangle_t\right)^2 \right\rangle_t}{\left[\left\langle \left(\theta_i(t) - \langle \theta_i(t) \rangle_t\right)^2 \right\rangle_t \right]_i} ; \tag{3.7}$$

where $\mathrm{VAR}(\theta_i(t))$ represents the variance for the time evolution of the phase of the i^{th} neuron.

This measure is the ratio between the variation of the average phase and the average variation of single phases. In a incoherent state, in the ideal $N \to \infty$, $T \to \infty$ limit, averaging on all phases would give $[\theta_i(t)]_i \approx 0$ with very small oscillations, thus $\chi^2 \approx 0$. A perfect synchronization, with all equal phases, would clearly result in $\chi^2 = 1$. The great advantage of the network coherence is that it depends only on *variations* of the phases, and not on possible net average value, moreover is much less computationally costly than $r(t)$.

In figure 3.6 (a) the measure of coherence is represented for different network sizes. From a qualitative point of view, we see that the improvement in *de*synchronization follows the same trend a the coefficient of variation: larger networks with neurons less connected (thus less correlated) show smaller levels of synchronization.

The continuous lines are fits in the form $\alpha + \beta N^{-\gamma}$. It has been reported [9] that $\chi^2 \propto 1/N$. Although the data points fall well on the curve, the results are $\gamma = 0.75$ for $K = 20$, $\gamma = 0.71$ for $K = 50$ and $\gamma = 0.33$ for $K = 100$. The value $\gamma = 1$ can be a limit case, when conditions are close to ideal (i.e. much larger networks weakly connected). However the power law decrease suggests that synchronicities are due to finite-size effect on the network, and the decrease of synchronization is more effective when neurons have fewer connections.

In figure 3.6 (b) a sample of $r(t)$ for a $N = 500$, $K = 20$ network is shown. Its offset seems much closer to 1 than we would expect, namely $< r(t) >_t = 0.486$. This is due to the fact that, in a system like ours, the $r(t)$ parameter is not well suited to capture the global synchronization, as it is sensitive to the overall net angle distribution. Due to the nonlinear instant inhibitions, phases tend to linger more on certain ranges, so that they hardly average to zero. As a check, we performed a complete randomization on the ordering of the phases (bot for neurons and times), and recomputed the order parameter, obtaining $< r_{\mathrm{rand}}(t) >_t = 0.4660$, far from the value $r(t) \simeq 0$ we would expect in completely decoupled systems.

The benefit found in the computation of the Kuramoto order parameter is that, as clearly visible in figure 3.6 (b), it reveals the actual frequency of the weak synchronization of the network. The period appears to depend only on K, while the difference in the amplitude reveals disordered excursions from more

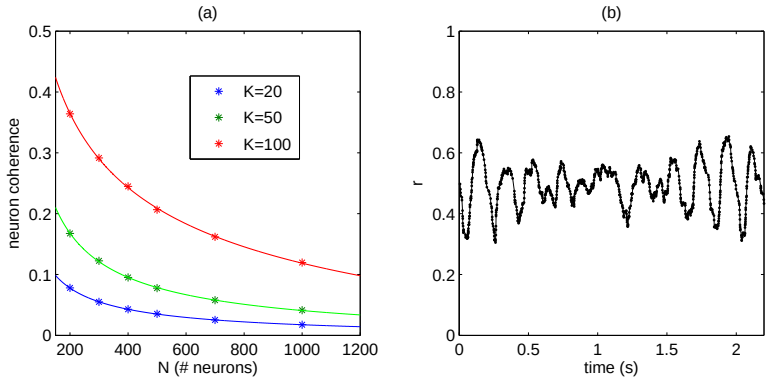

Figure 3.6: Network coherence as defined in (3.7) and an example of $r(t)$ (3.6) evolution in a $N = 500$, $K = 20$ system

synchronized periods to almost completely desynchronized ones. The frequencies found for $K = 20$, $K = 50$, $K = 100$ are, respectively: 4.8 ± 1 Hz, 6.7 ± 1 Hz and 7.9 ± 1 Hz.

3.5 Attractor Dimension and Entropy

At this point we can start the analysis of the Lyapunov spectrum and of the information we can obtain from its analysis. The typical signature of deterministic extensive chaos would be a Lyapunov spectrum invariant of the system size: the values are on the same curve, but denser as the number of dimensions increase [8].This seems to be the case for diluted networks, as clear from figure 3.7 (a). Nevertheless figure 3.7 (b) shows that the spectrum shapes seem more dependent on the size as the coupling becomes higher ($K = 100$) . The effect tends to decrease for larger networks, as we can say confronting the distance between $N = 500$ and $N = 1000$, with the separation between $N = 200$ and $N = 300$. Qualitatively, this behaviour follows the same trend of the network coefficient of variation: increasing the connections compromises the vicinity to optimal condition, but the discrepancy is slowly regained as the network size increases. In the end is reasonable to expect, as reported in [8, 9], that on very large network scales, such as $N = 10^3 - 10^4$, the spectra would always show a good superimposition.

As reported in section 1.6 the rate of entropy production for a SRB measure is given by Pesin identity:

$$\hbar(\mu) = \sum_{\lambda^{(i)}>0} \lambda^{(i)} \ .$$

For general measures the $=$ sign becomes an upper bond $\leq$.

The information dimension comes from the Kaplan-Yorke conjecture, mentioned in section (1.7)

$$\dim_\Lambda(\mu) = k + \frac{\lambda^{(1)} + \ldots + \lambda^{(k)}}{|\lambda^{(k+1)}|} \ ;$$

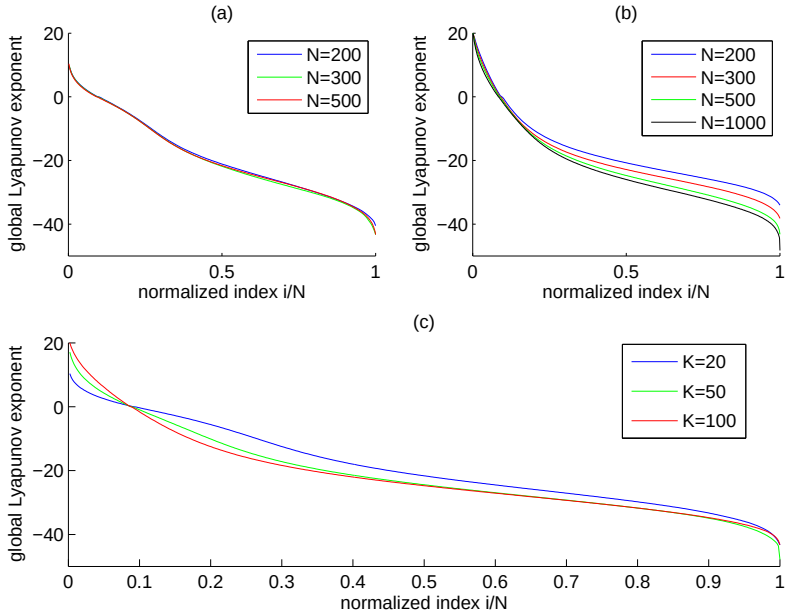

Figure 3.7: Different examples of Lyapunov spectrum. The spectra for all the computed network sizes and $K = 20$ are shown in (a); in (b) the parameter is $K = 100$; in figure (c) we fixed $N = 500$, and plotted the spectra for all values of K.

From figures 3.8 (a) and (b) we see that both $\hbar(\mu)$ and $\dim_\Lambda(\mu)$ grow linearly with N, as typical for extensive properties. The attractor dimension shows a very small growth for decreasing K, reflecting the fact that the system is slightly less synchronized. For the entropy this trend in much marked: weakly connected network produce less entropy as their Lyapunov spectrum results a little more flattened. The data substantially confirms what has already been found for a broader range of network dimensions in [8].

Whether our ergodic measure is SRB or not, remains an open question. In section 3.7 we tackle the problem by giving an esteem of the hyperbolicity of the dynamical systems we are considering. As explained in the last part of chapter 1 (see page 28) if a dynamical system is hyperbolic and satisfies the further requirement of having its periodic points dense on the attractor, we can "naturally" define a unique SRB measure over it.

3.6 Lyapunov Vectors Convergence

Before expressing any result or measure concerning the Lyapunov vectors, it is fundamental to test their reliability from every possible perspective. Firstly we check the coincidence between the Lyapunov spectra computed in the backward and in the forward iterations, respectively from the normalization coefficients of the the Gram-Schmidt basis and of the Lyapunov vectors. Although locally different, when used to compute the Lyapunov spectrum they superimpose, as shown in figure 3.9 (a). Figure 3.9 (b) shows how the quadratic deviation

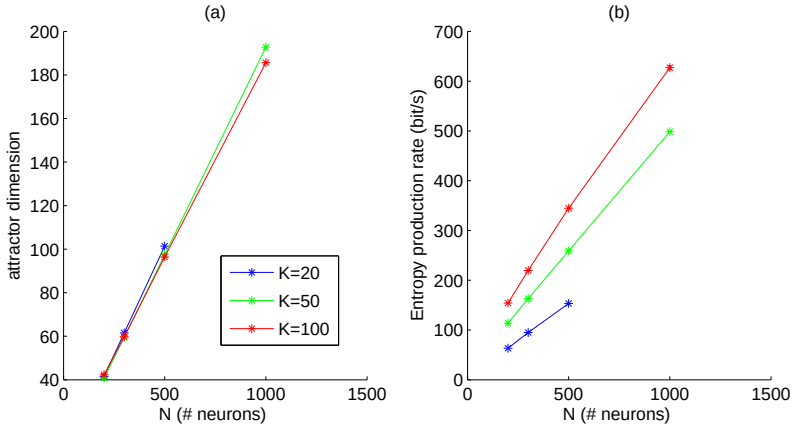

Figure 3.8: Attractor dimension (a) and entropy production rate for different values of N and K (color). They are calculated using, respectively (1.16) and (1.15).

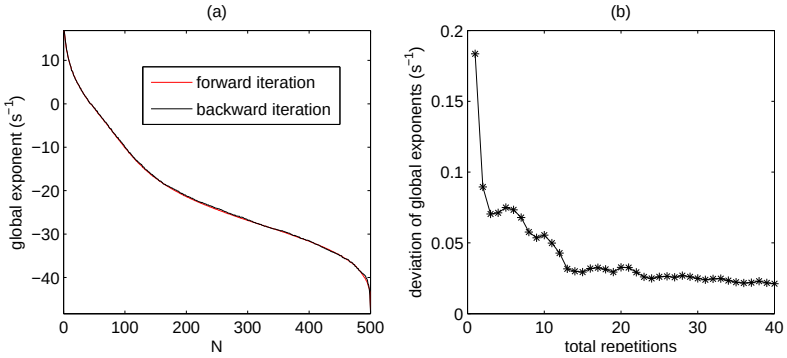

Figure 3.9: (a): superimposition of Lyapunov spectra calculated evolving the GS vectors (in red) and the Lyapunov vectors (in black). Figure (b) shows the quadratic deviation for averages on an increasing number of iterations

$\Delta\lambda^2 = 1/N \sum_{j=1}^{N} (\lambda_{\mathrm{FW}}^{(j)} - \lambda_{\mathrm{BW}}^{(j)})^2$ decreases when the spectra are averaged over several repetitions with different starting phases.

Afterwards, we consider the vector invariance under different initializations of the starting random C matrix. Using the parameters $S_{\mathrm{All}} = 15000$ and $s_{\mathrm{sk}} = 3$, we compute the full set of vectors in time $\boldsymbol{v}^{(j)}(t_s)$ for 6 different random initial conditions on C . All vectors are normalized, thus we measure their variation using the angles. Taking the first simulation as a reference, and calling $\tilde{\boldsymbol{v}}^{(j)}(t_s)$ the vector calculated with changed initial conditions, we measure: $\alpha^{(j)}(t_s) = \arccos\left(\boldsymbol{v}^{(j)}(t_s) \cdot \tilde{\boldsymbol{v}}^{(j)}(t_s)\right)$.

In figure 3.10 the time averages of $\alpha^{(j)}(t_s)$ are plotted for every vector, in systems of size $N = 300$ and $N = 500$ and with the 5 different C initializations coded by colors. Vectors are represented in abscissa by their corresponding global exponent. The first thing we notice is that vectors mostly do align in the same direction, but might have an opposite orientation: from the linearity of our calculations is clear that if we initialize the system with $\tilde{C}_{s+1} = -C_{s+1}$ we will get exactly the same evolution in time, except all vectors will be inverted. Such

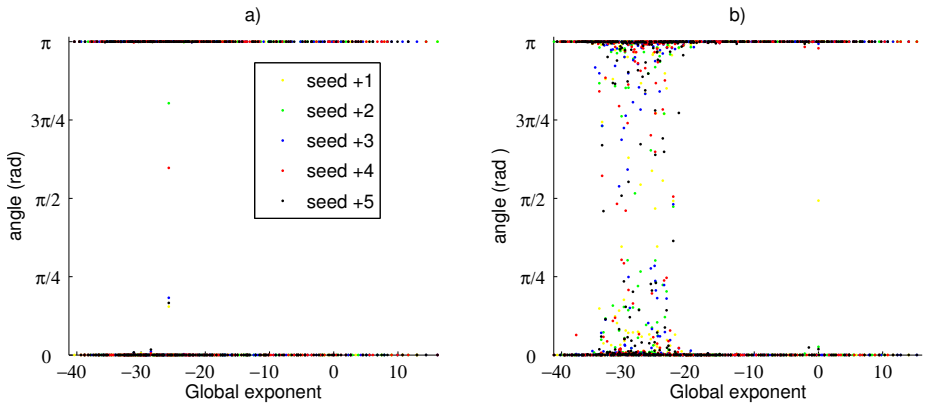

Figure 3.10: Time average of the angles between reference Lyapunov vectors, and vectors calculated starting with 5 different random initializations (color coded). (a) $N = 300$, $K = 50$; (b) $N = 500$, $K = 50$.

symmetry comes from the fact that Lyapunov vectors encode only *directions*, while their orientation depends on the random starting conditions. For a perfect convergence, we would see two straight lines in 0 and π; unfortunately for the network of bigger size, it seems that in a certain range, roughly in the second half of the spectrum, some vectors do not converge. They represent a small fraction: with a $\pm 5°$tolerance they are $\sim 9\%$ of the total.

Some examples of the time evolution of the $\alpha^{(j_{\mathrm{bad}})}(t_s)$ angles are shown in figure 3.11. Apparently, at least for some of them, there is convergence after some time. If we take into consideration only the first 10 seconds of our data-set, the "bad vectors" for $N = 500$ decrease to the $\sim 8\%$ of the total. For a S_{Al} long enough we would expect that all vectors eventually align, but the computation would not be feasible in terms of memory and time.

Our next step is checking the *time* convergence of the vectors. In a $N = 500$, $K = 50$ network we confronted the vector angles between a standard iteration $S_{\mathrm{All}} = 15000$ (corresponding to an evolution of ~ 90 seconds), and iterations where the last S_{Al} steps are cut of varying lengths, ranging from 100 to 14500. A scheme of the process is represented in figure 3.12.

In figure 3.13 (a) the angle averaged in time is represented. The colors code for different extension of the calculation. It is clear that when S_{Al} is negligible, there is no chance of proper alignment. Increasing its value has a quite positive effect, but, of course, we cannot expect any improvement from the "bad vectors" pinpointed in the previous test. Figure 3.13 (b) shows the angle evolution for the vector corresponding to the zero exponent. The fact that it loses alignment for longer times is indicative of its small instability.

Figure 3.14 (a) shows the average angles for all the time evolutions we sampled. It is clear that vectors nearer the first and the last exponents converge faster than the group in the middle. Figure 3.13 (b) shows some examples taken from (a), while in (c) we see the ratio of vectors with a misalignment bigger than 5°. The time length we chose is enough to limit them to $\sim 10\%$ of the total.

In conclusion, we have found that most vectors, except a sparse fraction increasingly small for larger S_{Al}, converge locally in time. This unstable vectors

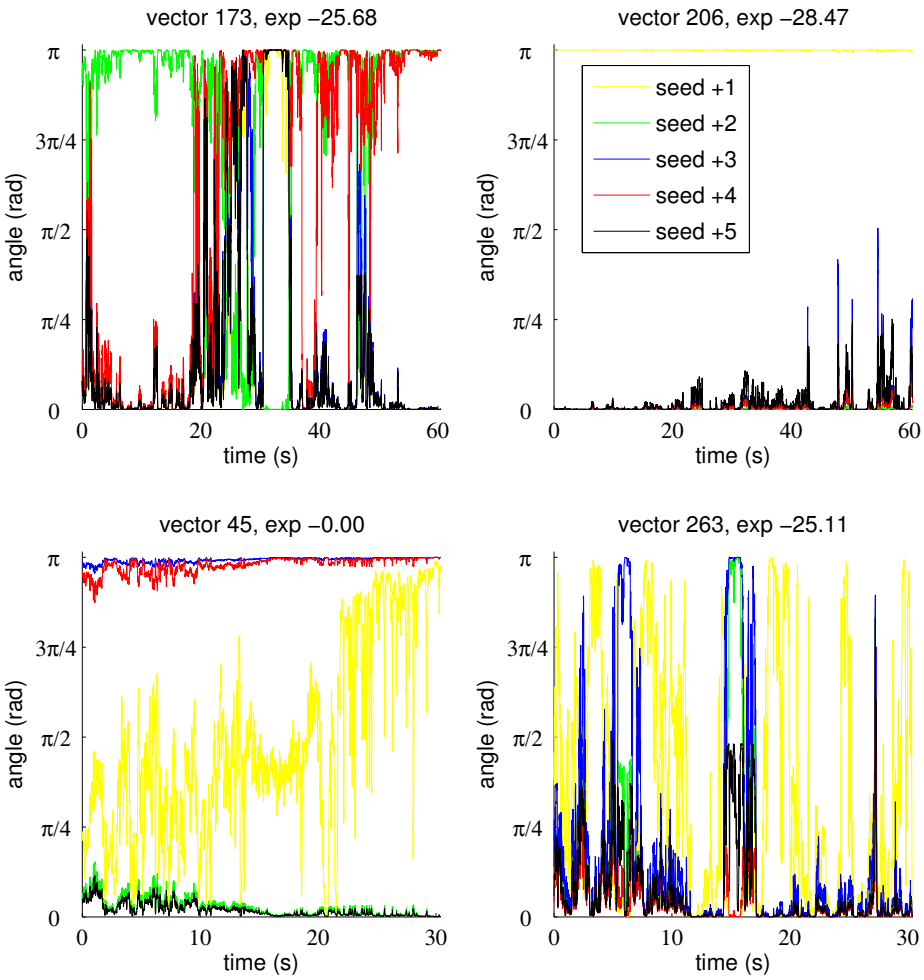

Figure 3.11: Angle evolution in time for some vectors not converging properly, selected as the outliers in figure 3.10. Upper part $N = 300$, $K = 50$, lower part $N = 500$, $K = 50$.

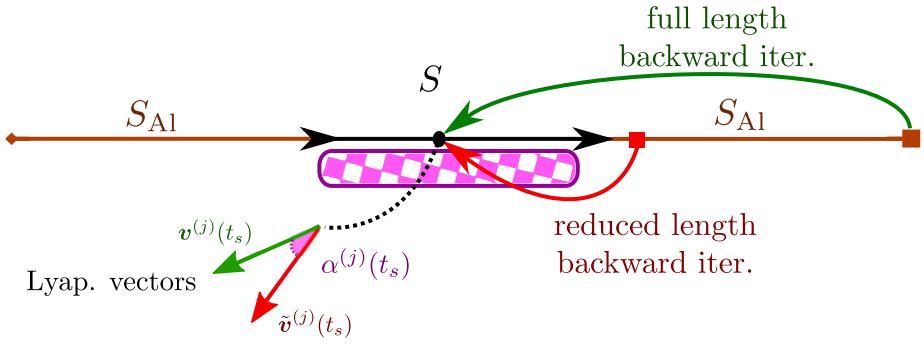

Figure 3.12: Convergence test performed with a reduction on the total computed time.

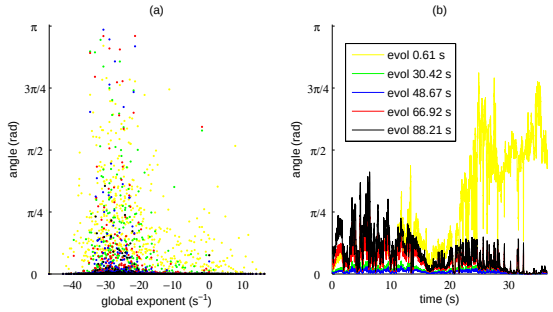

Figure 3.13: Convergence test performed cutting the total calculated time for a $N = 500$, $K = 50$ system. (a) shows the time average of angles between vectors for some of the durations considered (color coded). (b) the angle in time for vector 45, corresponding to a $\simeq 0$ global exponent: a certain instability is detected.

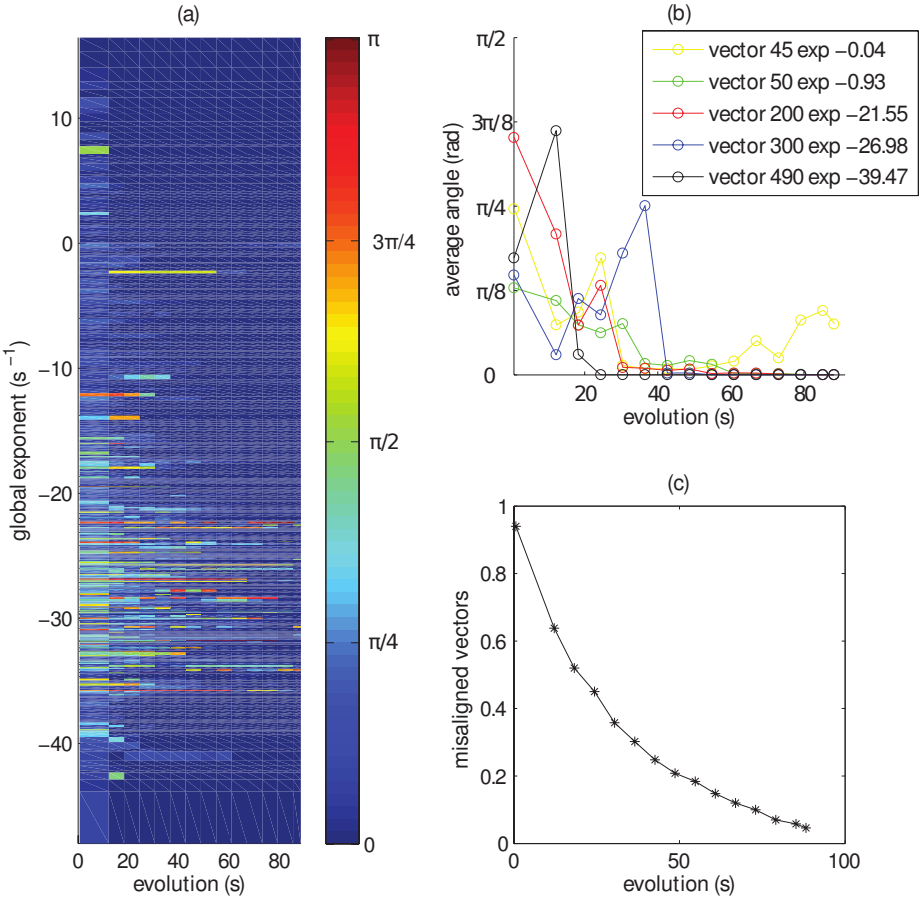

Figure 3.14: Convergence test performed cutting the total calculated time for a $N = 500$, $K = 50$ system.(a): average angles for all the considered time evolutions. (b): horizontal sections of (a) for some vectors. (c): the ratio of vectors with a misalignment larger than 5°.

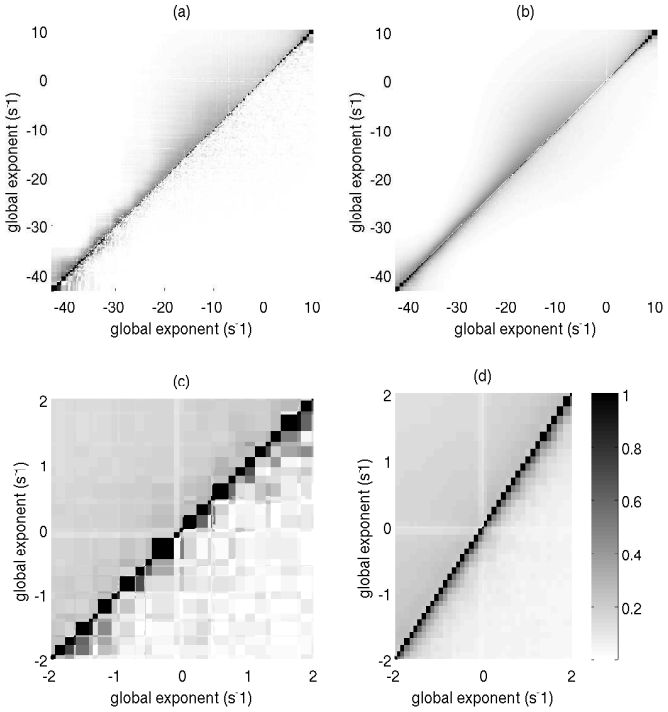

Figure 3.15: (a) - lower right: time averaged cosine of the angles between all vectors; upper left: circular variance (3.9) of the angles. (b) Average over $nI = 60$ iterations. (c) and (d) are magnifications of (a) and (b) around the 0 exponent.

seem to span a precise interval of global exponents. A possible explanation for the major stability of the first group is that the subspace considered has a smaller dimension, moreover no alignment is required for the first vector, since it is taken directly from the Gram-Schmidt basis. Instead exponents greater than $-35\ \mathrm{s}^{-1}$ appear a little more spaced, this, together with the strong backward expansion ratio, should account for their faster convergence. Checking how the time required for an optimal convergence varies for different network parameters would be an interesting direction for further analyses, but the scope of the present section is only to assess the invariance and the robustness of the Lyapunov vectors calculated with the backward iteration algorithm.

3.7 Angles and Hyperbolicity

We start the analysis of the vectors with an examination of the angles between them. For a $N = 500$, $K = 20$ system, figure 3.15 (a) shows, in the lower right part, the time average of the cosine of the angles between all vectors:

$$\langle \cos \alpha_{ij}(t) \rangle_t \coloneqq \left\langle \boldsymbol{v}^{(i)}(t) \cdot \boldsymbol{v}^{(j)}(t) \right\rangle_t \ . \tag{3.8}$$

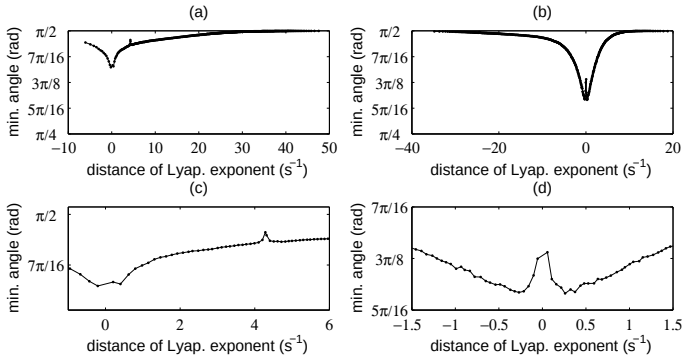

Figure 3.16: The abscissa represents the average angles between a single vector and all the others, the ordinate is the difference between Lyapunov exponents associated to the network. (a) vector 15, Lyap. exp 4.3 and (b) vector 300 exp -24.5 . Figures (c) and (d) are magnifications of, respectively (a) and (b). The network parameters are $N = 500$ and $K = 20$.

The upper left part is the *circular variance*: a measure on how angles deviate in time from their mean values.

$$\sigma^2(\alpha_{ij}) := 1 - \sqrt{\left(\langle \sin \alpha_{ij}(t) \rangle_t\right)^2 + \left(\langle \cos \alpha_{ij}(t) \rangle_t\right)^2} \,. \tag{3.9}$$

The vectors are referred to their corresponding global Lyapunov exponent, rather than to their index. Figure 3.15 (c) shows an enlargement of the same figure, limited to the vectors around the zero exponent. Figures 3.15 (b) and (d) represent averages over 60 repetitions of the same system.

Our results is that the angles of neighboring vectors have a higher variability in time and are, on average, more tangent to their close neighbours. For a more quantitative evaluation, figures 3.16 (a) and (b) depict two examples of the average angle between a single vector and all the others, versus their "distance", i.e. the difference in the Lyapunov exponents. The chosen vectors are the 15^{th} and the 300^{th}. Distant vectors are orthogonal, but the separation is good also for near ones, (the scale starts from 45°); moreover, the closest neighbours (i.e. the points around 0) have higher angles than the 2^{nd} order neighbours: it appears that vectors associated to similar exponents are nevertheless quite autonomous in direction. The effect is more marked for negative exponents, as shown in figure 3.16 (c), finally in figure 3.16 (d) the small peak on the right corresponds to vectors 46 and 47 : the vectors with nearly zero exponent tend to be more orthogonal to the rest, as also visible from the slightly lighter lines in figures 3.15.

The same graphs, plotted for networks of different size N and average connections K, look very similar, although the Lyapunov spectrum undergoes slight changes in shape and in density. The reciprocal angles between the vectors, at least when averaged on large times, appear an invariant property of the dynamical system.

As already stated at the end of chapter 1 (see page 28), the condition for a dynamical system to be hyperbolic is that the tangent space can be decomposed as the direct sum of expanding and contracting modes. The Lyapunov vectors,

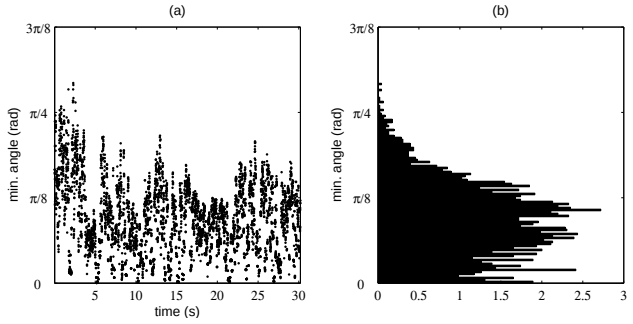

Figure 3.17: (a): minimum angle between contracting and expanding directions in time (3.10), for a $N = 500$ $K = 20$ network; (b): associated distribution

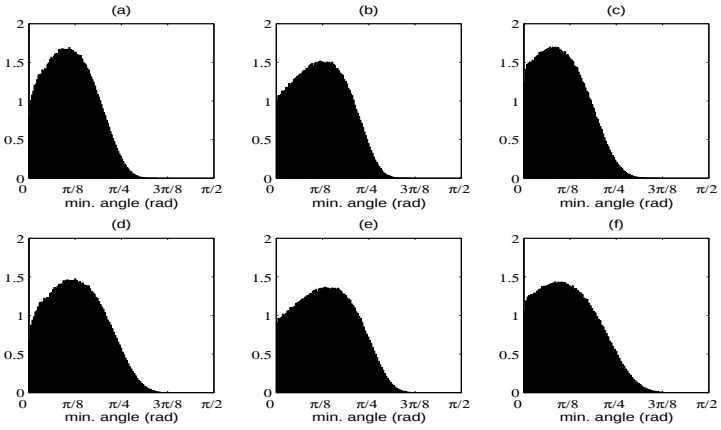

Figure 3.18: Minimum angle distributions averaged over several repetitions. Upper row: $N = 500$, $nI = 60$, $K = 20$, 50 and 100; lower row: $N = 200$, $nI = 200$, K as above.

coding the directions of expansion and contractions, are very good candidates to access the hyperbolic properties of the system. For example in [41] it is shown that, for generic nonlinear dissipative partial different equations, they can be used to discriminate between physical modes, important for the dynamical evolution, and nonphysical modes, rapidly decaying in time.

We consider all the vectors corresponding to positive global exponents as expanding modes, while vectors decoding negative exponents as contracting ones. A quantitative measure of the decoupling is then given by the least of the angles between contracting and expanding directions.

$$\alpha_{\min}(t) = \min_{ij}\{\alpha_{ij}(t) | \lambda^{(i)} > 0 \wedge \lambda^{(j)} < 0\} \; . \tag{3.10}$$

This quantity is measured for each timestep of the system evolution. Figure 3.17 (a) shows an example of $\alpha_{\min}(t)$ for a $N = 500$, $K = 20$ network; (b) represents its statistical distribution. Figure 3.18 represents the minimum angle distributions averaged over several iterations for different network parameters. In the upper part we have $N = 500$ and $K = 20$, 50, 100. In the lower part

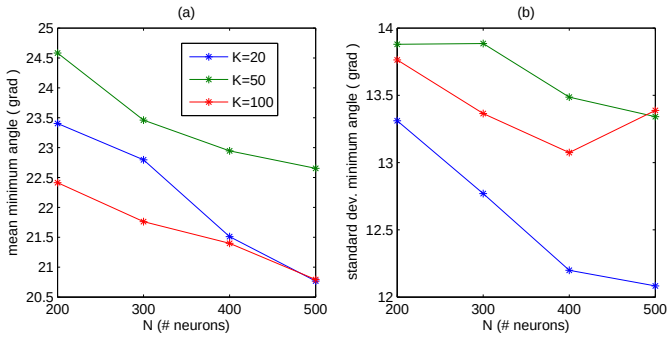

Figure 3.19: Average and standard deviation of minimum angles (3.10) distributions for all the computed network parameters.

$N = 200$ and K as before. We made 60 iterations on the $N = 500$ network, and 200 for $N = 200$. To perform the overall distribution, a correction is introduced: namely we exclude all angles involving the vector with the exponent closest to zero, assumed to (almost) correspond to a direction parallel to the motion, neither expanding not contracting and so not interesting for our esteem. The ratio of those angles increases with K and decreases with N. Without this correction, the distributions $K = 50$ and $K = 100$ would have a maximum at 0. The two rows are associated to networks of quite different size, but their shapes look surprisingly similar. However, with a closer look, we can see that the $N = 500$ distributions are a little more peaked with respect to the $N = 200$.

The time average and the standard deviation for systems of different size are plotted in figure 3.19. There is, apparently, a general trend, i.e. larger networks have slightly narrower distributions, with smaller averages; but the variations remain very small, limited to few degrees. Moreover there are anomalous points, and the role of K is not really clear.

To sum up, we can say that a certain separation between expanding and contracting direction is present, and it becomes sharper in larger networks. Nevertheless, to confirm this tendency, measures on much broader scales of networks are necessary. Another crucial improvement would be to calculate exactly the vector associated to the 0 exponent, the one parallel to the trajectory, and exclude it for the angle measurements.

3.8 Participation Ratio and Chaos Index

The participation ratio of a (normalized) vector $\boldsymbol{v}^{(j)}$ at time t_s is defined as:

$$\mathrm{PR}^{(j)}(t_s) = \left(\sqrt{\sum_{i=1}^{N} (\boldsymbol{v}_i^{(j)}(t_s))^4} \right)^{-1} . \tag{3.11}$$

It is a measure of the effective number of basis components that have a role in the vector evolution. As a matter of fact, if a normalized vector has only one component $(0\,0\ldots0\,1\,0\ldots0)$, its PR is 1; for a vector equally involving all dimensions $(1/\sqrt{N}\,1/\sqrt{N}\ldots1/\sqrt{N})$, instead, $\mathrm{PR} = N$. In our setting, the

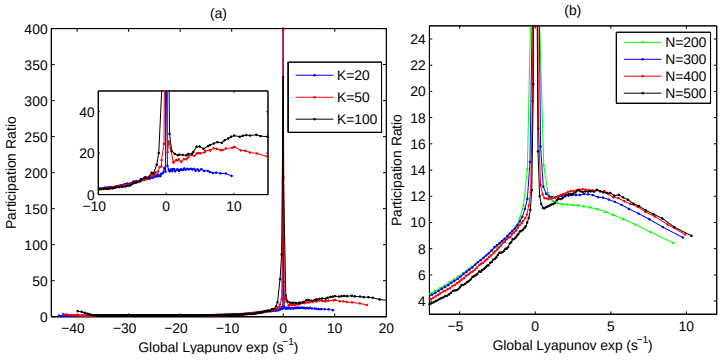

Figure 3.20: Participation ratio of each Lyapunov vector (a) for a $N = 400$ network with different average connections and (b) for $K = 20$ networks of different sizes.

base elements correspond to neurons, while vectors correspond to expanding and contracting directions. The participation ratio informs us of how many neurons are effectively taking part to an expanding or contracting mode, with the degree of expansion/contraction given by the Lyapunov exponent associated to the specific vector.

Figure 3.20 (a) shows the time-averaged participation ratio for networks with $N = 400$ and different K. The peak corresponds to the 0 exponent, parallel to the direction of motion: it nearly reaches 400, which means that the trajectory is tangent to all neurons. This is a clear outcome of the specific network dynamics: between two pulses all neuron phases evolve uniformly in time with the same velocity, so that the phase space trajectory is a line tangent to all directions. When the average connections between neurons are increased, more of them take part in the expanding directions and the systems is less stable. For contracting directions, instead, every network seems to reach the same minimum, with a SR $\simeq 1.6$.

In figure 3.20 (b) we see comparisons between different network sizes with K fixed on 20. The average is performed both on time and on several network iterations. When the size increases, the difference in the curves shrinks, as if they are converging to a limit value. Moreover larger networks seem more precise in the localization of the zero vector, as they are more peaked around the 0 exponent.

Overall, we see that the number of neurons involved in expanding directions has the order of $\sim K/3$, and is not greatly conditioned by the network size, the tangent direction involves *all* neurons, finally contracting modes involve less than 2 effective neurons under any condition.

The participation ratio expresses *how many* neurons participate in the dynamics of a given vector. To find *which* are the interested neurons we define the *chaos index*, in the form:

$$c_i^{(j)} := \frac{1}{S} \sum_{s=1}^{S} (\boldsymbol{v}_i^{(j)}(t_s))^2 \ . \tag{3.12}$$

For a given neuron i, $c_i^{(j)}$ represents its contribution to the time evolution of vector $\boldsymbol{v}^{(j)}$, or, equivalently, to the direction expanding with rate $\exp(\lambda^{(j)})$.

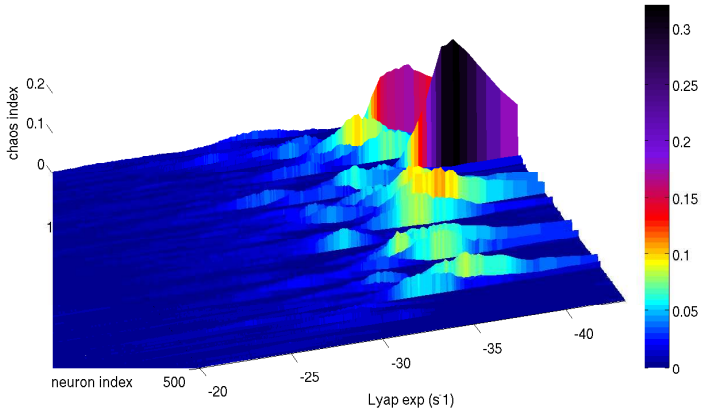

Figure 3.21: Chaos index as defined in (3.12) (z axis) for every neuron and every Lyapunov vector (on y and x axis). The first half of the vectors, cut from the graph, show a substantially flat $C_i^{(j)}$

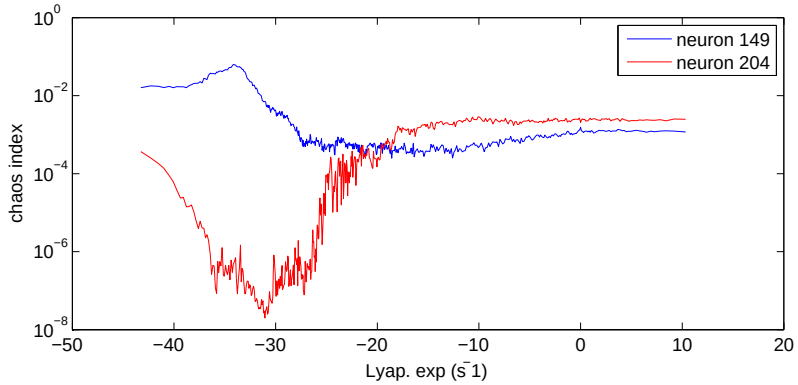

Figure 3.22: Detail of the same dataset of figure 3.21. The $c_i^{(j)}$ for neurons of index $i = 149$ and $i = 204$ is shown on logarithmic scale.

Figure 3.21 represent the chaos indexes in a $N = 500$ $K = 20$ network. The x axis reports the Lyapunov exponents $\lambda^{(j)}$, the y axis contains the network indexes i, with no privileged ordering, due to the randomness of the connections. The value of $c_i^{(j)}$ is substantially very small for all the positive exponents and for some of the negative. When we go to lower values, however, we start seeing peaks corresponding to neurons greatly contributing to a certain range of contracting directions.

Figure 3.22 represents two neurons chosen from the previous plot so that the first (neuron 149) has a peak in the contracting modes, the second (204) appears flat. With a logarithmic scale it is clear that they are covering different areas of the Lyapunov spectrum. The first half of the spectrum, from $\sim$10 to $\sim$ -20 (s^{-1}), does not show any peak, as most of the neurons are contributing uniformly to it, their contribution drops to very small levels after the -20 threshold. However a minority of neurons, such as the 149, contributes less to the expanding and

weakly-contracting directions, but shows high $c_i^{(j)}$ values in specific ranges or strong contracting directions.

Confronting those findings with the participation ratios of the exponents, and the information on the network structure, we can sketch a model of the network dynamics. All neurons evolve linearly in time, taking part in the tangent direction with 0 Lyapunov exponent. A smaller group of order $\simeq K$ are also receiving inhibitory signals, an average of $\sim 1/3$ of them results crucial in the punctual network evolution, as revealed in the participation ratio of positive vectors. The $\simeq K$ inhibited neurons change with time, covering the whole network, so that none of them is privileged in contributing to expanding directions. A few neurons are particularly uninfluential: they correspond to contracting directions, thus to negative Lyapunov exponents. This property comes from the interplay between the network structure and the global dynamical model, so it is localized on specific neurons, as revealed by the peaks in their chaos indexes.

To quantify the overall participation of a single neuron to expanding and contracting directions, we define two parameters in the form:

$$\mathrm{P}_i^{\lambda+} = \sqrt{\left[c_i^{(j)}\right]_{\lambda^{(j)}>0}} \qquad \mathrm{P}_i^{\lambda-} = \sqrt{\left[c_i^{(j)}\right]_{\lambda^{(j)}<0}} \tag{3.13}$$

we call them, respectively, *participation to expansion* and *participation to contraction* of neuron i. The value is squared because the chaos index is defined as a quadratic average.

Figure 3.23 (a) shows the distribution of $\mathrm{P}_i^{\lambda-}$, (b) is for $\mathrm{P}_i^{\lambda+}$. As we expect, the participation to expansion is much more peaked: most of the neurons contribute with an average value. For the contracting direction, we see a much broader distribution: the great contributors are associated to the peaks of figure 3.21. From the distribution of $\mathrm{P}_i^{\lambda+}$ we can draw an hypothesis on the shape of the participation ratio (figure 3.23). Most of the neurons do not participate to expansion with their maximum value, so

To assess the validity of the defined parameters, we can try to relate them with other quantities of the system. Figure 3.23 (c) shows, for each of the 500 neurons, the participation to contraction versus the average frequency $\bar{\nu}_i$. The red line is a fit in the form $C_1 + C_2 \exp(-\bar{\nu}_i)$, with $C_1 = 0.03 \pm 0.01$ and $C_2 = 0.85 \pm 0.02$. The neurons with low frequencies contribute to contracting directions much more than those with high frequencies, with a very simple exponential equation.

The *expanding* and *contracting* in phase space represent, dynamically, the propagation or decays of perturbations in the network. A neuron with a very high spiking frequency, when perturbed by some discretionally small noise, will rapidly communicate the variation to its $\simeq K$ postsynaptic neurons, consequently changing the evolution of the whole network, with an initial direction given by those $\simeq K$ neurons, weighted on their future influence, so that the actual participation ratio results smaller than K. A neuron with a very low frequency, on the other hand, is continuously inhibited by others, and sends very few signals: it would hardly lead a global change, or, equivalently, have a role in a vector associated to a positive exponent.Our result is that the $\mathrm{P}_i^{\lambda-}$ can give a very precise characterization of the frequencies, as is a good discriminant between the neurons.

In figure 3.23 (d) we try the same with the $P_i^{\lambda+}$, expecting a monotonically increasing function due to the reasons stated above. However, for frequencies higher than 1Hz, there is a drop: although some neurons have higher frequencies, they do not appear to stand over others in the characterization of the expanding directions. A possible explanation for this phenomenon lies in the inhibitory nature of the network: a frequently-pulsing neuron would frequently inhibit the neurons of its postsynaptic set, making them "dull" and less responsive to small variations of its own signal, thus its average contribution to positive exponents is decreased. Apparently the system self-adapts, so that the optimal frequency for transmissions is around the *average* frequency of the neurons, 1 Hz.

We may inquire if we could gain some information on the frequencies by studying the graph structure of the network. Neurons with low spiking frequencies receive a higher number of inhibitory signals. We expect that the quantity of received signals depend on the number of incoming connections. Figure 3.24 (a) shows, for every neuron, the number of presynaptic neurons versus its average frequency. An inverse proportionality is evident, however we see that, by using simply the static structure of the graph, a proper characterization of the neurons is not reachable.

Finally figure 3.24 (b) represents $P_i^{\lambda-}$ versus $P_i^{\lambda+}$. For great values they roughly show inverse proportionality, as we expect, but the initial points have a less trivial behaviour. As a direction for further studies, we could try to relate this figure with the level of hyperbolicity of the system. The concept of well separated directions for expanding and contracting modes corresponds to neurons on which dominates either $P_i^{\lambda+}$ or $P_i^{\lambda-}$; the unexpected rise at the beginning of figure 3.24 (b) could thus be related to the incomplete hyperbolicity showed by the network.

To sum up, in the present section the Lyapunov vectors, so far expressed as abstract entities of the phase space, have been reconnected to the effective dynamical behaviour of the neural network. The informations gained from parameters such as the participation ratio, the chaos index or the $P_i^{\lambda-}$ help us characterize both qualitatively and *quantitatively* the emergent behaviour of the network. Although the qualitative results are supported by our information on the network and our intuitive idea of its functioning, a quantitative explanation requires the creation of an approximated theoretical model.

3.9 Optimizations and Further Analyses

In this chapter many results on the behaviour of the network have been shown, however, especially for the Lyapunov vector analysis, the chosen network sizes lie in the relatively small range of $200 - 500$ neurons. To draw more general conclusions, find rules on how quantities scale with network parameters, and characterize the properties of the $N \gg K \gg 1$ regime, we should study systems in a broader range of N and with a higher resolution in the K.

An increase in the network size N would result in a slowing down of all computational processes involving $N \times N$ matrices, and in a bigger request of RAM. The computation speed can be "easily" boosted with a complete parallelization of all matrix operations. For the evolution and computation of Lyapunov vectors, the bottleneck remains in the memory usage, since both the Gram-Schmidt

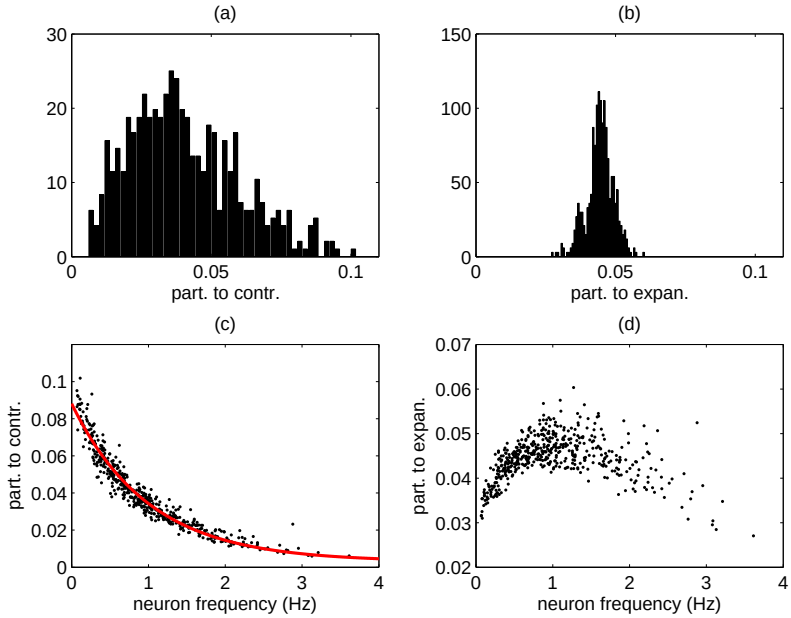

Figure 3.23: (a), (b): distribution of respectively $\mathrm{P}_i^{\lambda-}$ and $\mathrm{P}_i^{\lambda+}$, defined in (3.13), for all neurons of a $N = 500$, $K = 20$ network. (c), (d): $\mathrm{P}_i^{\lambda-}$ and $\mathrm{P}_i^{\lambda+}$ as a function of the neuron frequency. The red line corresponds to the curve $y = 0.03 + 0.85\exp(-x)$

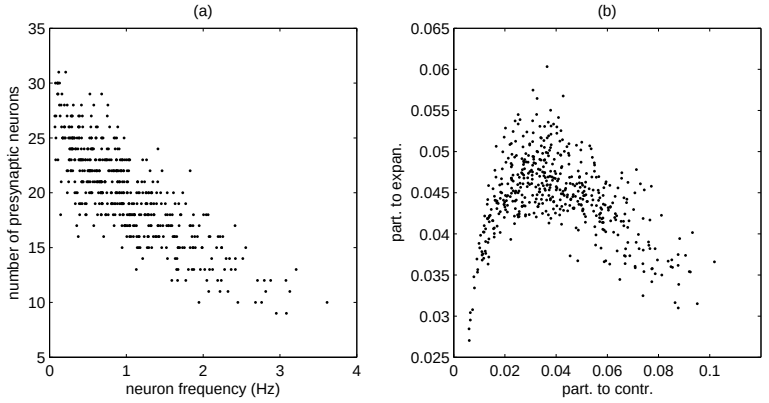

Figure 3.24: (a): number of presynaptic neurons related to neuron frequency for all neurons of a $N = 500$, $K = 20$ network. (b): plot of $\mathrm{P}_i^{\lambda+}$ versus $\mathrm{P}_i^{\lambda-}$

basis and the R matrices need to be saved locally in time. A solution of almost immediate implementation consists in storing the matrices on the local hard drive, and reload them when needed, with the downside of the time cost related to the use of physical memory. Alternatively, the simulation can be divided into smaller time intervals, saving GS basis and the state of the neurons only at the beginning of each of them; when needed by the backward vector iteration, the forward evolution is recomputed and saved on one interval at a time, and cleared afterwards. With the latter method, we can still rely on the much higher speed of virtual memory, but a parallelization of the processes would be strongly recommended.

Finally, as already mentioned, a more careful esteem of the minimum time needed for the Lyapunov vector convergence should be performed, so that the choice of the time length can be optimized on the network size.

With a broader data set, and the experience gained from the results already obtained, many other analyses become possible. A better sampling in the average connection parameter K, for example, could lead to precise scaling laws regarding the coefficient of variation, the network collective frequency, the entropy production rate, the maximum participation ratio, etc. , providing new insights on the functioning of the network. We could then investigate on relations between attractor dimension and participation ratio, or between entropy production and the $P^{\lambda+}$ parameter. Finally, to achieve a solid result on the presence of hyperbolicity, a systematical study on networks of much larger sizes should be performed.

Most of the numerical parameters shown here here have been qualitatively connected to our information on the network structure and dynamics. Many of the curves, however, are quite regular in their shapes and, in some cases, as in the $P_i^{\lambda+}$ versus $\bar{\nu}_i$ graph (figure 3.23 (c)), very simple fits can be found. Such findings surpass our qualitative idea of the network evolution, and express with precise numerical quantities its ergodic (and emergent) properties. For this reason, they could be taken as directions for the construction of a quantitative theoretical model of the network, which, in turn, would be used to verify our findings and give new ideas for other comparisons.

Chapter 4

Discussion

In the present work we extensively studied the dynamics of pulse-coupled inhibitory neural networks of QIF neurons, with the aim of creating a model qualitatively similar, in its behaviour, to networks of real pyramidal neural cells, and then fully characterize it.

Our findings are summarized in the following section.

4.1 Conclusions

The first result, well documented in scientific literature [32, 34, 8], is that a large number of simple oscillators with a phase linearly increasing, when sparsely connected with nonlinear inhibitory pulses, shows a disordered and chaotic behaviour similar to the so-called balanced state of real pyramidal neurons. Using the Kuramoto order parameter, the coefficient of variation and the measure of neuron coherence (3.5 - 3.7), we quantified how much the system as a whole is incoherent and near a Poisson point process. A closer look to single neurons, however, reveals an intrinsic oder: as a matter of fact the global behaviour is an example of emergent deterministic chaos, and is not due to any random variable.

In a reductionist point of view, our $N \gg 1$ - dimensional dynamical chaotic system results already fully characterized; our knowledge, however, is far from complete. A mean field approach, as shown in appendix A, can give *average* network properties with all the necessary approximations. To move furtherly in the characterization of the system, we rely on the ergotic theory.

The computation of the Lyapunov spectrum leads to an esteem of the attractor dimension and of entropy production, in substantial agreement to results already published [8, 9]. Then, using an algorithm proposed in a recent article [23], we moved to the caculation and the systematic study of the Lyapunov vectors.

Since no other examples of their use for similar systems have been found in the scientific literature, we performed a series of convergence checks, which confirmed both their invariance and the robustness of the algorithm.

Afterward, the vectors have been used as a quantitative esteem of the degree of hyperbolicity of the dynamical system. In a fully hyperbolical system, the measures of entropy production and attractor dimension would be more solid

and not approximate esteems. Our result is that such a property shows partially, but we *might* reach a full structural stability in networks of bigger size.

Finally we expressed other ergodic properties given by the systematic study of the Lyapunov vectors, and showed how they are connected with the effective dynamics of the neurons within the network. We have found that the system auto-organizes so that the majority of neurons equally contributes in the determination of the global dynamics, distributing their role in time, moreover the optimal frequency for the signal propagation in the network corresponds to the *global* average frequency: neurons pulsing with higher frequencies do not stand over others in determining the dynamics. On the other hand, a small group of selected neurons, stable in time, shows very little sensitivity to perturbations. They tend to have lower frequencies, and a very simple relation between frequency and contribution to dynamically decaying modes can be found.

Overall, the Lyapunov vector approach offered fruitful insights in the collective behaviour of the network, differentiating the role and contribution of neuron groups, always seen in the context of their global, dynamical structure. Approaches based on reduction to lesser dimensions, or to the study of the static graph of connections, would hardly provide as much information.

In the end, the results are encouraging but not completely satisfactory for two main reason: first of all, with our computational capabilities we have only approached the ideal condition of very large, and very sparsely connected networks (i.e. $N \gg K \gg 1$), further measures and optimizations are requested to express more solid results; secondly, there is no quantitative theoretical model which could be compared with the numerical findings and with the curves resulting from our measures.

4.2 Extensions

In section 3.9 we already mentioned possible improvements and optimizations for the *current* system. Here we describe a few of the many possible extensions which can be added.

First of all, we could use our *a priori* knowledge of the system to detect and isolate the tangent Lyapunov vector, i.e. the one corresponding to the 0 exponent. Since its direction is neither expanding nor contracting, no vectors would converge on it, either in forward or backward expansion. Our only hope is to catch it "by exclusion", relying on the randomness of the initializations. Inserting the tangent vector in the GS system would give us much more precision in the calculations of the nearly 0 Lyapunov exponents and in their corresponding directions: a more solid measure of hiperbolicity would then result.

A rather obvious direction of investigation would be checking the robustness of collective network dynamics for changes in the single neuron model; then we may inquire how the addition of more realistic traits, such as a delay in the signal transmission or the presence of excitatory pulses, modifies the results.

In all runs we used the fixed topology of a sparse random graph, characterized by relatively small variations in the number of incoming and outgoing connections. We may inquire whether a more diversified connectivity would give rise to a predominant role for some neurons, or if the system would somehow re-balance

those differences, as it already does when it limits the impact of high-frequency neurons.

Finally we could consider whether our Lyapunov-based approach answers to the general problem of determining a *centrality measure* in complex networks. Centrality measures are esteems of the "importance" of a given node in the network: they are crucial, for example, in models of power grids, spreading of diseases, etc. Traditionally, centrality measures rely on the underlying structure of the connection graph, not taking the network dynamics into account. A recent attempt to define a centrality measure based on dynamics can be found in [42]. Our contribution to expansion and contraction parameters, defined in (3.13), could possibly fall in this category. The only requirement for our computation is the (numerical) knowledge of the Jacobian matrix in every point of the system evolution. As long as a dynamical system, regardless of its structure, dynamics or dimension, satisfies this requisite, we can, in principle, perform on it the complete analysis of Lyapunov exponents, vectors and, along with them, of all the parameters defined in this work.

Appendix A

Temporal Fluctuations in Balanced State

Recalling the formula (2.11), we can distinguish an external component, which is assumed to be constant in time and equal for all neurons, and an internal current, depending on the network dynamics, which is therefore the only source of fluctuations. For simplicity we restrict ourselves to a population of inhibitory neurons. The current from the network is then:

$$I_{\mathrm{netw}}(t) = -\frac{J_0}{\sqrt{K}} \sum_{\hat{t}^{(p)} \in \mathrm{CTS}} \zeta(t + \hat{t}^{(p)}) \tag{A.1}$$

CTS stands for *compound spike train*, and represents the ordered uninion of the spiking times sets of each neuron. If our system is weakly correlated and very large, it is reasonable to assume that spikes near in time are uncorrelated with very few exceptions. Thus the spike-time distribution can be approximated with a Poisson point process (see section 1.4 of the book [27]).

We define the *event rate* as:

$$\Omega(t) \coloneqq \lim_{\Delta t \to 0} \frac{\text{mean number of events in } \Delta t \text{ bins}}{\Delta t} \,. \tag{A.2}$$

For a given $\Omega(t)$ function, the conditional probability of having N_{spi} total events at times $\left\{\hat{t}^{(1)}, \ldots, \hat{t}^{(N_{\mathrm{spi}})}\right\}$ is given, in Poisson statistics, by the formula:

$$P(N_{\mathrm{spi}}, \{\hat{t}^{(1)}, \ldots, \hat{t}^{(N_{\mathrm{spi}})}\} | \Omega(t)) = \frac{1}{N_{\mathrm{spi}}!}\, e^{-\int_0^T ds\, \Omega(s)} \prod_{p=1}^{N_{\mathrm{spi}}} \Omega(\hat{t}^{(p)}) \tag{A.3}$$

The current averaged over this distribution is then:

$$[\langle I_i(t) \rangle_t]_i = -\sum_{N_{\mathrm{spi}}=1}^{\infty} \int_0^T \cdots \int_0^T \prod_{p=1}^{N_{\mathrm{spi}}} d\hat{t}^p\, P\left(N_{\mathrm{spi}}, \{\hat{t}^{(1)}, \ldots, \hat{t}^{(N_{\mathrm{spi}})}\} | \Omega(t)\right) \cdot \\ \cdot \frac{J_0}{\sqrt{K}} \sum_{p'=1}^{N_{\mathrm{spi}}} \zeta(t - \hat{t}^{(p')}) \,; \tag{A.4}$$

explicitly:

$$-\frac{J_0}{\sqrt{K}}\, e^{-\int_0^T ds\,\Omega(s)} \sum_{N_{\mathrm{spi}}=1}^{\infty} \int_0^T \cdots \int_0^T \prod_{p=1}^{N_{\mathrm{spi}}} d\hat{t}^{(p)} \frac{\Omega(\hat{t}^{(p)})}{N_{\mathrm{spi}}!} \sum_{p'=1}^{N_{\mathrm{spi}}} \zeta(t-\hat{t}^{(p')}) \,. \tag{A.5}$$

Since the shape of $\zeta(t-\hat{t}^{(p')})$ is invariant of the considered spike, the sum over p' corresponds to a single sample times the total number of spikes:

$$-\frac{J_0}{\sqrt{K}}\, e^{-\int_0^T ds\,\Omega(s)} \sum_{N_{\mathrm{spi}}=1}^{\infty} \int_0^T d\hat{t}^{(1)} N_{\mathrm{spi}} \zeta(t-\hat{t}^{(1)}) \Omega(\hat{t}^{(1)}) \int_0^T \cdots \int_0^T \prod_{p=2}^{N_{\mathrm{spi}}} d\hat{t}^{(p)} \frac{\Omega(\hat{t}^{(p)})}{N_{\mathrm{spi}}!} \,. \tag{A.6}$$

The $\hat{t}^{(p)}$ are just dummy variables, so that every term of the product over p is equal. This leads to:

$$-\frac{J_0}{\sqrt{K}}\, e^{-\int_0^T ds\,\Omega(s)} \sum_{N_{\mathrm{spi}}=1}^{\infty} \frac{1}{(N_{\mathrm{spi}}-1)!} \left(\int_0^T ds\,\Omega(s) \right)^{N_{\mathrm{spi}}-1} \left(\int_0^T ds\,\zeta(t-s)\,\Omega(s) \right) \,. \tag{A.7}$$

Finally the sum over N_{spi} can be seen as the expansion series of an exponential, and consequently simplified with the exponential term. The result is:

$$\left[\langle I_i(t)\rangle_t\right]_i = -\frac{J_0}{\sqrt{K}} \int_0^T ds\; \zeta(t-s)\; \Omega(s) \,. \tag{A.8}$$

With the further assumption that the event rate is stationary in time, and is a $\mathcal{O}(K)$, we can write it as:

$$\Omega(t) \equiv K\,\bar{\nu} \tag{A.9}$$

which, considering the properties (2.12), $\zeta(t)$ will integrate to one. This leads to the result given in equation (2.18).

Appendix B

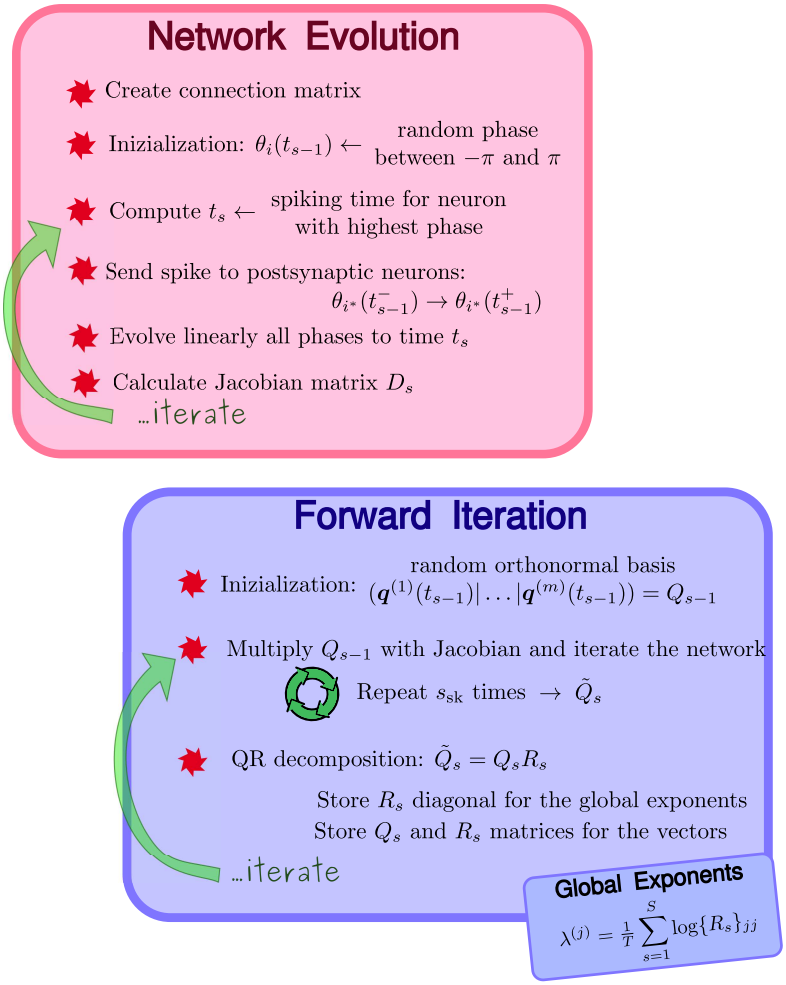

Figure B.1: Schematic representation of the algorithms used to iterate the network and calculate the Lyapunov exponents. In the first box t_s is computed with (2.32), postsynaptic neurons are update with (2.33), linear evolution is given by (2.31), finally D_s comes from (2.36 - 2.39).

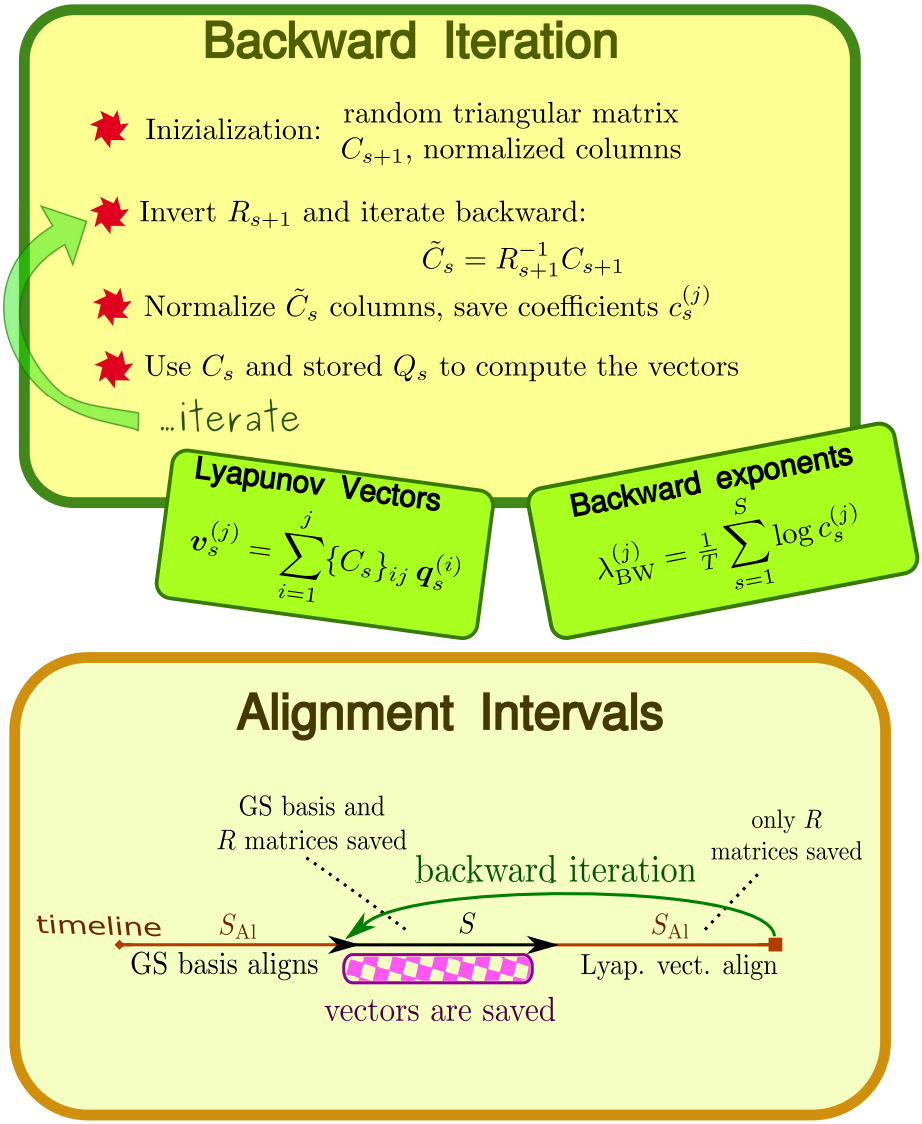

Figure B.2: Upper part: schematic representation of the algorithm used to calculate the time evolution of Lyapunov vectors, as reported in [23]. Below: how the simulation times are structured, so that the interval S_{Al} is devoted to convergence, for both GS basis and vectors.

Bibliography

[1] M. E. J. Newman. The structure and function of complex networks. *SIAM Review*, 45(2):pp. 167–256, 2003.

[2] Steven H. Strogatz. Exploring complex networks. *Nature*, 410(6825):268–276, March 2001.

[3] Albert-László Barabási. *Linked: How Everything Is Connected to Everything Else and What It Means*. Plume, reissue edition, April 2003.

[4] Simon Haykin. *Neural Networks: a Comprehensive Foundation*. Macmillan College Publishing Company, New York, 1994.

[5] Charles S Peskin. *Mathematical aspects of heart physiology*. Courant Institute of Mathematical Sciences, New York University, 1975.

[6] Sven Jahnke, Raoul-Martin Memmesheimer, and Marc Timme. Stable irregular dynamics in complex neural networks. *Phys. Rev. Lett.*, 100(4):048102, Jan 2008.

[7] A. Politi, R. Livi, G.-L. Oppo, and R. Kapral. Unpredictable behaviour in stable systems. *EPL (Europhysics Letters)*, 22(8):571, 1993.

[8] Michael Monteforte and Fred Wolf. Dynamical entropy production in spiking neuron networks in the balanced state. *Phys. Rev. Lett.*, 105(26):268104, Dec 2010.

[9] Michael Monteforte. *Chaotic Dynamics in Networks of Spiking Neurons in the Balanced State*. PhD thesis, Georg-August University, Göttingen, Germany, 2011.

[10] J. P. Eckmann and D. Ruelle. Ergodic theory of chaos and strange attractors. *Rev. Mod. Phys.*, 57(3):617–656, Jul 1985.

[11] David Ruelle. *Chaotic Evolution and Strange Attractors*. Cambridge University Press, 1989.

[12] Steven H. Strogatz. *Nonlinear Dynamics and Chaos*. Westview Press, 1994.

[13] Edward Ott. *Chaos in Dynamical Systems*. Cambridge University Press, 2002.

[14] Massimo Cencini, Fabio Cecconi, and Angelo Vulpiani. *Chaos: From Simple Models to Complex Systems*. World Scientific Publishing, 2010.

[15] George D. Birkhoff. Proof of the ergodic theorem. *Proc. Nat. Acad. Sci.*, 17:656–660, 1931.

[16] V.I. Oseledec. A multiplicative ergodic theorem. Lyapunov characteristic numbers for dynamical systems. *Trans. Moscow Math. Soc.*, 19:197–231, 1968.

[17] Jim Kelliher. Lyapunov exponents and Oseledec's multiplicative ergodic theorem.
Url: `http://math.ucr.edu/~kelliher/Geometry/ErgodicLecture.pdf`, 2003.

[18] Giancarlo Benettin, Luigi Galgani, Antonio Giorgilli, and Jean-Marie Strelcyn. Lyapunov characteristic exponents for smooth dynamical systems and for hamiltonian systems; a method for computing all of them. part 1: Theory. *Meccanica*, 15:9–20, 1980. 10.1007/BF02128236.

[19] Jim Kelliher. Oseledec's multiplicative ergodic theorem.
Url: `http://math.ucr.edu/~kelliher/Geometry/LectureNotes.pdf`, 2002.

[20] Giancarlo Benettin, Luigi Galgani, Antonio Giorgilli, and Jean-Marie Strelcyn. Lyapunov characteristic exponents for smooth dynamical systems and for hamiltonian systems; a method for computing all of them. part 2: Numerical application. *Meccanica*, 15:21–30, 1980. 10.1007/BF02128237.

[21] Alan Wolf, Jack B. Swift, Harry L. Swinney, and John A. Vastano. Determining lyapunov exponents from a time series. *Physica D: Nonlinear Phenomena*, 16(3):285 – 317, 1985.

[22] J. P. Eckmann, S. Oliffson Kamphorst, D. Ruelle, and S. Ciliberto. Liapunov exponents from time series. *Phys. Rev. A*, 34(6):4971–4979, Dec 1986.

[23] F. Ginelli, P. Poggi, A. Turchi, H. Chaté, R. Livi, and A. Politi. Characterizing dynamics with covariant Lyapunov vectors. *Phys. Rev. Lett.*, 99(13):130601, Sep 2007.

[24] A.L. Hodgkin and A.F. Huxley. A quantitative description of membrane current and its application to conduction and excitation in nerve. *The Journal of Physiology*, 117:500–544, 1952.

[25] Eugene M. Izhikevich. *Dynamical Systems in Neuroscience.* MIT Press, Cambridge, Massachusetts, 2007.

[26] Erik De Schutter. *Computational Modeling Methods for Neuroscientists.* MIT Press, Cambridge, Massachusetts, 2010.

[27] Peter Dayan and L.F. Abbott. *Theoretical Neuroscience.* MIT Press, Cambridge, Massachusetts, 2001.

[28] C. Morris and H. Lecar. Voltage oscillations in the barnacle giant muscle fiber. *Biophysical Journal*, 35(1):193 – 213, 1981.

[29] Xiao-Jing Wang. Ionic basis for intrinsic 40 hz neuronal oscillations. *NeuroReport*, 5(20):6402–6413, Dec 1993.

[30] Eugene M. Izhikevich. Which model to use for cortical spiking neurons? *IEEE Transactions on Neural Networks*, 15(5):1063–1070, Sept 2004.

[31] Massimo Cencini, Fabio Cecconi, and Angelo Vulpiani. *Chaos: an Introduction to Dynamical Systems*. Springer, 1997.

[32] Boris S. Gutkin and G. Bard Ermentrout. Dynamics of membrane excitability determine interspike interval variability: A link between spike generation mechanisms and cortical spike train statistics. *Neural Computation*, 10(5):1047–1065, 1998.

[33] GP Moore, DH Perkel, and JP Segundo. Statistical analysis and functional interpretation of neuronal spike data. *Annual Review of Physiology*, 28:493–522, 1966.

[34] C. van Vreeswijk and H. Sompolinsky. Chaotic balanced state in a model of cortical circuits. *Neural Comput.*, 10:1321–1371, Aug 1998.

[35] Bilal Haider, Alvaro Duque, Andrea R. Hasenstaub, and David A. McCormick. Neocortical network activity in vivo is generated through a dynamic balance of excitation and inhibition. *J. Neurosci.*, 26(17):4535–4545, 2006.

[36] Michael J. Higley and Diego Contreras. Balanced excitation and inhibition determine spike timing during frequency adaptation. *The Journal of Neuroscience*, 26(2):448–457, 2006.

[37] Rune W. Berg, Aidas Alaburda, and Jørn Hounsgaard. Balanced inhibition and excitation drive spike activity in spinal half-centers. *Science*, 315(5810):390–393, 2007.

[38] S. Olmi, A. Politi, and A. Torcini. Collective chaos in pulse-coupled neural networks. *EPL (Europhysics Letters)*, 92(6):60007, 2010.

[39] Juan A. Acebrón, L. L. Bonilla, Conrad J. Pérez Vicente, Félix Ritort, and Renato Spigler. The kuramoto model: A simple paradigm for synchronization phenomena. *Rev. Mod. Phys.*, 77(1):137–185, Apr 2005.

[40] David Golomb and John Rinzel. Clustering in globally coupled inhibitory neurons. *Physica D: Nonlinear Phenomena*, 72(3):259 – 282, 1994.

[41] Hong-liu Yang, Kazumasa A. Takeuchi, Francesco Ginelli, Hugues Chaté, and Günter Radons. Hyperbolicity and the effective dimension of spatially extended dissipative systems. *Phys. Rev. Lett.*, 102(7):074102, Feb 2009.

[42] Konstantin Klemm, M. Angeles Serrano, Victor M. Eguiluz, and Maxi San Miguel. A measure of individual role in collective dynamics: spreading at criticality.
Url: `http://arxiv.org/abs/1002.4042v2`,
2010.

Aknowledgment

I would like to express my gratitude to Prof. Fred Wolf for introducing me to the world of neuroscience and neural networks, adding nicely expanding directions in the phase-space of my dynamical evolution (a.k.a. *personal growth*). A big thank to Prof. Leone Fronzoni for his complete support and guidance in the writing of the thesis, and to Doctor Antonio Politi for his useful suggestions and vital corrections to the first, rough results I got.

The firm, and already quite high foundations of this thesis are in the preceding works by Michael Monteforte, and his marvelous network simulation program: his great patience, as well as the free use of his code, made this research possible. Thank you!

Thanks to Denny Fliegner for efficiently providing me the necessary computational resources, to Yorck-Fabian Beensen for keeping my desktop PC alive, connected and fully functional. Thanks to Katharina Jeremias, Regina Wunderlich, Ayse Bolik and Victoryia Novak, the administrative staff, for helping me whenever I needed signatures, refunding modules, faxes, photocopies or general information about what was happening around. Overall, I genuinely appreciated the lively, informal and stimulating atmosphere of the MPI for Dynamics and Self Organization, and my gratitude and admiration goes to all those who keep sustaining, renovating and enriching it every single day.

Besides the academic sphere, I wish to thank all those who eagerly and friendly supported me during my first days (and months) in Göttigen. For their punctual help, precious suggestions, and human warmth I've never truly felt alone in a foreign country. Thanks Mirko and Elena, Tatjana T, Theresa and Alana, David H, Markus H and Gabriella.

A special thank to my friends and colleagues in Pisa, starting from those who kindly and nobly accepted to host me during my "short", thesis-related staying: Anna S, Daniela C, Marco L, Luna, Gianluca C. A big thank also to Luigi C, Lapo F, Sabrina S, Mamta A, Giulia P ,Antonella S , Sarah D, since they all positively influenced me over our long, common, university years. I owe them some part of my personal growth and I shared with them many of the happiest moments of my student life (apparently also a few of the saddest and shabbiest :-P). Thanks!

Many others should be mentioned, such as Blanca Lidia E, for her positive persistence and her fortune-telling attempts, Debora L, for a friendship clear and simple, as much as spontaneous and perfect; Angelica Z, for her being strong and different, no matter what... then I'm grateful to people like Jacopo P, Pina & Irene, Emanuela, Else P, Angelo R, Barbara C, Silvia B, Alina & Michaela, Giovanni C, Dora S, Chiara Giovanna B, Nishathri D, Nancy M, AnnaChiara M, for apparently no other reasons that the fact I feel happy at the idea we are wandering around on the same planet, and, hopefully, we shall keep doing that for very long.

My biggest "thank you", however, goes to who has read the current page this far, maybe out of simple curiosity, maybe looking for his/her name, maybe for no reason whatsoever. Thanks to be here, right now, and to take a look at my work. Take care.